UNIVERSITY OF CALIFORNIA SAN DIEGO

Excursions in light-dressed matter systems: From Floquet engineering to molecular polaritonics

A dissertation submitted in partial satisfaction of the
requirements for the degree Doctor of Philosophy

in

Chemistry

by

Kai Schwennicke

Committee in charge:

Professor Joel Yuen-Zhou, Chair
Professor Daniel Arovas
Professor Clifford Kubiak
Professor Francesco Paesani
Professor Michael Tauber

2024

The Dissertation of Kai Schwennicke is approved, and it is acceptable in quality and form for publication on microfilm and electronically.

University of California San Diego

2024

DEDICATION

To my loving family for their unwavering support throughout this lengthy journey and for reminding me of the importance of balance — that stepping away from work for a quick surf can be just as crucial as the work itself.

EPIGRAPH

Science is magic that works.

Kurt Vonnegut, Cat's Cradle

TABLE OF CONTENTS

LIST OF FIGURES

LIST OF TABLES

ACKNOWLEDGEMENTS

First and foremost, I would like to extend my deepest gratitude to my Ph.D. advisor, Professor Joel Yuen-Zhou. Thank you for taking a chance on a naive experimentalist who had a knack for algebra and calculus but lacked physical intuition. You taught me that the simplest intuitive explanation is often more elegant than the most complex mathematical expression. Without your guidance, support, and patience, I would not be half the theorist I am today.

Next I would like to thank the members of the Yuen-Zhou research group. I will forever cherish my time spent with Juan B. Pérez-Sánchez and Sindhana S. Pannir-Sivajothi, with whom I began this Ph.D. journey. From stimulating scientific discussions to spirited and lighthearted conversations outside the lab, our friendship pushed me to become the best scientist I could be. They also reminded me that research requires one to take a break here and there. To previous members, Dr. Matthew Du, Dr. Luis Martínez-Martínez, Dr. Jorge Campos-Gonzalez-Angulo, Dr. Raphael Ribeiro, and Dr. Stephan van den Wildenberg, thank you for always having time for my incessant questions. I have continued this tradition, albeit in a reversed role, with the newer members of our group, Arghadip Koner, Yong Rui Poh, and Sricharan Raghavan Chitra. I thank them for injecting new excitement into our research and reminding me that I never know as much as I think I do.

I would also like to express my gratitude to my friends from UCSD, especially those from the Biochemistry track. Thank you for welcoming a lowly theorist into your ranks. I will always be grateful for your friendship, which made my time at UCSD thoroughly enjoyably.

I am indebted to Stephen Randall, Jason Banister, and Grace Anne Carrick for putting up with living with me in San Francisco amidst a pandemic. Words cannot express how fondly I cherish those memories during such a scary time when the world stood still.

To my lifelong friends Rory McClish and Timothy Denham: thank you for being my steadfast support, lifting me from my lows and grounding me at my highs. Thank you both for providing me a space to get away from research and recalibrate to my truest self.

Last, but not least, I need to thank my incredible family. To my amazing sister Shea

Schwennicke, thank you for always taking my unscheduled calls, providing a place for me to stay in Costa Rica, and the fun times when I crashed on your couch in Santa Barbara. I am consistently blown away by your life achievements, adventures, and the quality of your character; I am always honored to be your brother. To my loving parents, Robert and Lisa Schwennicke, thank you for cultivating my curiosity in mathematics and science from a young age and instilling a deep love and appreciation for the ocean and travel. Your "Carpe diem" outlook on life provided invaluable support during the inevitability rough patches of this wild journey and consistently reminded me to take time for myself away from work.

Chapter 2, in full, is adapted from the material as it appears in "Optical activity from the exciton Aharonov–Bohm effect: A Floquet engineering approach," by K. Schwennicke and J. Yuen-Zhou, *J. Phys. Chem. C.* **124.7**, 42026-4214 (2020). The adaptations made here were informed by and aligned with corrections provided in "Corrections to 'Optical activity from the exciton Aharonov–Bohm effect: A Floquet engineering approach,"' by K. Schwennicke and J. Yuen-Zhou, *J. Phys. Chem. C.* **126.36**, 15547-15548 (2022), which was published subsequently. These adaptations were introduced because we realized that although the qualitative basis of our model is correct, its application to anthracene is erroneous. Specifically, in our model, we want to drive a Fanck–Condon (FC) active mode, which is a totally symmetric mode, with an infrared (IR) laser. This is not possible for anthracene, which belongs to the D_{2h} point group, because the totally symmetric mode, a_g, is IR inactive (it does not transform as x, y, or z). For the totally symmetric mode to be IR active, the molecule must lack an inversion center. An example of such a molecule is carbazole (see Figure 2.1). The dissertation author was the primary investigator and author of these papers.

Chapter 3, in full, is adapted from the material as it appears in "Enantioselective Topological Frequency Conversion," by K. Schwennicke and J. Yuen-Zhou, *J. Phys. Chem. Lett.* **13.10**, 2434-2441 (2022). The dissertation author was the primary investigator and author of this paper.

Chapter 4, in full, is adapted from the material as it appears in "Extracting accurate light-matter coupling from disordered polaritons," by K. Schwennicke, N. C. Giebink, and J.

Yuen-Zhou, *Nanophotonics* (2024). The dissertation author was the primary investigator and author of this paper.

Chapter 5, in full, is adapted from the materials as it appears in "Classical linear optics effects in molecular polaritonics" by K. Schwennicke, A. Koner, J. B. Pérez-Sánchez, and J. Yuen-Zhou, in preparation (2024). The dissertation author was the primary investigator and author of this paper.

VITA

2018	Bachelor of Science in Chemistry, University of California Santa Barbara
2018–2019	Teaching Assistant, University of California San Diego
2020	Master of Science in Chemistry, University of California San Diego
2024	Doctor of Philosophy in Chemistry, University of California San Diego

PUBLICATIONS

K. Schwennicke, N. C. Giebink, and J. Yuen-Zhou, "Extracting accurate light-matter couplings from disordered polaritons" *Nanophotonics* (2024)

K. Schwennicke and J. Yuen-Zhou, "Enantioselective Topological Frequency Conversion," *J. Phys. Chem. Lett.* **13.10**, 2434-2441 (2022)

K. Schwennicke and J. Yuen-Zhou, "Optical activity from the exciton Aharonov–Bohm effect: A Floquet engineering approach," *J. Phys. Chem. C.* **124.7**, 42026-4214 (2020)

ABSTRACT OF THE DISSERTATION

Excursions in light-dressed matter systems: From Floquet engineering to molecular polaritonics

by

Kai Schwennicke

Doctor of Philosophy in Chemistry

University of California San Diego, 2024

Professor Joel Yuen-Zhou, Chair

The detection and manipulation of matter with light is a ubiquitous goal of chemists and physicists. However, this endeavor faces inherent challenges due to the typically "weak" light-matter interaction and discrepancy in scale between molecules and the spatial variation of the electromagnetic field. Such limitations hinder the ability to differentiate between similar molecules and effectively modify their characteristics.

In this dissertation, we seek to transcend the limitations of typical light-matter interactions by introducing innovative laser protocols and venturing into the realm of strong coupling. We aim to overcome the challenges attributed to natural and magnetically-induced optically activity and demystify phenomena intriguing to molecular polaritonic phenomena.

We begin by proposing a laser setup to generate synthetic gauge fields within molecular aggregates to induce a molecular excitonic version of the Aharovon-Bohm effect. Even though the undriven system is achiral, this laser-induced effect generates a non-zero circular dichroism signal. Notably, an unfeasibly strong static magnetic field is needed to generate a similar effect in electronic systems.

Next, we introduce a modified microwave three-wave mixing setup to achieve enantioselective topological frequency conversion. This approach, representing the first instance of a chiroptical spectroscopic signal directly linked to a topological invariant, underscores the potential of using topological principles to enhance the sensitivity and robustness of spectroscopic techniques for distinguishing between enantiomers.

Transitioning into the realm of strong coupling, we explore the effects of molecular disorder on the linear response of molecular polaritons. We provide analytical expressions for the vacuum Rabi splitting observed in the absorption, transmission, and reflection spectra under conditions of weak disorder, addressing multiple disorder distributions. Additionally, we introduce a novel sum rule offering a universal methodology for extracting accurate collective light-matter coupling values from experimental data.

Finally, we address the perplexing fact that classical linear optics can regularly describe polaritonic effects. We demonstrate that, in the thermodynamic limit, polaritonic transmission windows function as "optical filters", and many phenomena attributed to polaritons can be replicated in bare molecular systems using appropriately configured linear optical sources. This insight urges a reevaluation of certain "polaritonic" phenomena and identifies promising directions for future research to uncover genuinely novel polaritonic effects.

Chapter 1

Introduction

The interplay between light and matter drives numerous chemical, physical, and biological processes. Traditionally, this interaction operates within the "weak" coupling regime, where light perturbatively influences matter. Moreover, molecules are typically much smaller than the wavelength of light, preventing them from fully interacting with the three-dimensional spatial structure of the electromagnetic field. Such conditions often limit the effectiveness of light-based techniques in distinguishing between similar molecules or modifying their characteristics. This dissertation explores novel laser protocols and the realm of "strong" coupling, aiming to transcend these inherent limitations.

The first part of this dissertation addresses optical activity, which manifests as a different response to right- and left-handed circularly polarized light (RCP, LCP). Chiral molecules are prototypical examples of optically active materials. Importantly, chiral molecules that are non-superimposable images of each other, or enantiomers, show opposite optical activity [1]. Taking advantage of this phenomenon, the traditional chiroptical techniques of circular dichroism (CD) (difference in the absorption rate of RCP and LCP fields) and optical rotation (OR) (rotation of the plane of linearly polarized light) are used to measure enantiomeric excess in an ensemble of molecules. While in Nature optical activity is restricted to chiral media, one can induce the effect in any material by placing it in a static magnetic field that is perpendicular to the propagation direction of the probe light field. The magneto-optical (MO) effects that arise are magnetic CD

(MCD) and magnetic OR (MOR), which are analogous to the naturally occurring effects for chiral molecules [1]. While MCD is a useful spectroscopic technique for resolving electronic transitions in congested absorption bands [2, 3], MOR is a phenomenon that is routinely exploited in the development of optical devices, such as isolators and circulators [4]. While natural and magnetically-induced optical activity are extremely useful, they both have their shortcomings. CD and OR suffer from the weak interaction between molecules and the magnetic component of the optical field, which has led to the recent advocation for techniques that rely solely on electric dipole interactions; for example, creating synthetic chiral fields [5, 6] and employing enantiosensitive microwave three-wave mixing [7, 8]. Meanwhile, few materials possess strong MO effects that fall within the optical frequency regime [9, 10], creating a bottleneck for the downsizing of MO devices for optical communication and computation.

The latter half shifts focus to molecular systems under strong coupling. In the weak regime light and matter are considered distinct entities where the former perturbatively influences the latter, limited by the slow rate of excitation exchange between light and matter compared to their natural dissipation rates. By confining the radiation field within a small volume, the light and matter can exchange energy multiple times before the excitation escapes, intensifying the light-matter interaction such that it enters the strong coupling regime. In this regime, light and matter coalesce into hybrid states known as polaritons.

The hybridization of light and matter excitations in crystalline solids outside of cavities has been long known since the seminal works of Tolpygo [11] and Huang [12] on phonon-polaritons and Agranovich [13] and Hopfield [14] on exciton-polaritons in the 1950s. It was, however, until 1992 that Weisbuch [15] demonstrated that these strong coupling phenomena in inorganic semiconductors could be enhanced with optical microcavities (this statement is not always true, as recent work has shown that dielectric contrast between a bulk semiconductor and its surroundings can give rise to effective polariton formation too [16]). A few years later, Lidzey [17] reported the same feat with excitons in disordered organic films. The study of strong coupling for ensembles of molecular vibrations is much more recent [18, 19], yet serves as a

testament to the ubiquity of polaritonic phenomena across the electromagnetic spectrum.

Today, the burgeoning field of polaritonics shows promise in diverse applications ranging from manipulating chemical reactivity in both ground [20, 21, 22, 23, 24] and excited states [25, 26, 27, 28, 29, 30, 31, 32] to enhancing exciton transport [33, 34, 35, 36, 37, 38], facilitating long-range energy transfer [39, 40, 41, 42, 43, 44], enabling room temperature polariton condensation [45, 46, 47, 48, 49], altering organic photophysical dynamics [50, 51, 52, 53, 54], and modifying phase transitions [55]. Despite these advancements, the field is still marked by contradictory findings, with some studies reporting no polaritonic modification to chemical reactivity [56, 57, 58, 59] and no modification to reverse inter-system crossing from triplets to singlets [60]. Furthermore, with respect to modification of phase transitions, recent reports find that the re-scaling of the local temperature inside the cavity with respect to the temperature measured outside the cavity is the dominant mechanism over the proposed mechanism of renormalization of the material's free energy [61, 62]. This mix of positive and negative results underscores the nascent nature of the field and the need for further experimental and theoretical understanding, as highlighted by recent perspectives [63, 64, 65].

This dissertation seeks to navigate the challenges surrounding natural and magnetically-induced optical activity through innovative laser setups, including the realization of a molecular exciton Aharonov-Bohm effect via Floquet engineered synthetic gauge fields [66] and an enantioselective topological frequency conversion construction for the measurement of enantiomeric excess [67]. Additionally, this dissertation delves into molecular polaritonic phenomenon under strong coupling by studying molecular disorder effects on the linear response of molecular polaritons [68] and exploring the convergence of specific molecular polaritonic phenomena with linear optics [69]. In the latter it observed that for certain phenomena the polaritonic states act as simple optical filters, implying that identical phenomena can be achieved outside of cavity by pumping the bare molecular system with a filtered (reshaped) laser pulse whose intensity profile matches the polariton transmission spectrum. This revelation cautions making claims of "polaritonic" effects before optical filtering has been judiciously ruled out and underscores the

necessity for further exploration of systems that go past this linear regime to uncover truly novel polaritonic phenomena.

1.1 Summary of Contents

In Chapter 2, adapted from [66], we introduce a novel laser setup to generate synthetic gauge ("pseudomagnetic") fields, enabling the observation of a molecular exciton version of the Aharonov-Bohm effect. Using Floquet theory, we analyze the optical activity in an isotropic ensemble of achiral molecular aggregates driven by an elliptically polarized laser. We demonstrate that optical activity is absent under linear polarization but maximized with circular polarization. This distinction correlates with the existence of non-trivial and trivial exciton Aharonov-Bohm phases. Furthermore, we highlight that achieving a similar non-trivial phase in electronic with static magnetic fields would require impractically high strengths, far beyond those attainable in typical nano-ring systems that enclose equivalent areas to our molecular aggregates.

In Chapter 3, adapted from [67], we explore the adaptation of a microwave three-wave mixing setup, featuring slowly modulated microwave field amplitudes with incommensurate frequencies, to facilitate topological frequency conversion for enantiomeric mixtures. We derive an enantioselective topological invariant, proposing its application for precise enantiomeric excess measurement. This approach represents a significant advancement in chiral analysis, leveraging topological concepts to enhance selectivity and sensitivity.

In Chapter 4, adapted from [68], we investigate the impact of molecular disorder on the linear response of molecular polaritons across various disorder distributions and strengths. We present analytical expressions for the vacuum Rabi splitting in absorption, transmission, and reflection spectra under conditions of weak disorder, addressing Lorentzian, Gaussian, and rectangular distributions. Notably, even under strong disorder, rectangular distribution exhibits the emergence of two distinct side bands. Additionally, we introduce a novel sum rule applicable to all forms and strengths of disorder, offering a universal methodology for extracting accurate

collective light-matter coupling values from experimental data.

In Chapter 5, in part adapted from the materials as it appears in [69], we investigate the convergence of molecular polaritonics with classical linear optics. In the limit that the number of molecules coupled to a single cavity mode goes to infinity, we provide the analytical exact result that the polariton absorption is just the product of the bare molecular absorption and the linear polaritonic transmission spectra. In other words, the polaritonic transmission windows act as "optical filters" that determine what radiation can enter the cavity, after which the absorption of these frequencies by the molecules is solely determined by their bare absorption spectra. We then use this classical linear optics lens to demystify several "polaritonic" phenomena and show that for each instance the same result can be achieved outside of the cavity if an optical source with an intensity profile that mimics the linear polaritonic transmission spectrum. Finally, we discuss what polaritonic phenomenon cannot be explained using this classical optics perspective.

In Chapter 6, we summarize the research findings and provide an outlook on future research directions to advance the understanding and application of light-matter interactions.

Chapter 2

Optical activity from the exciton Aharonov-Bohm effect: A Floquet engineering approach

2.1 Introduction

Molecular enantiomers exhibit slightly different interactions with right and left-handed circular polarized (RCP, LCP) light fields. There are two important consequences of this effect: non-racemic samples exhibit finite circular dichroism (CD) (difference in absorption rate of RCP and LCP fields) and finite optical rotation (OR) (rotation of the plane of linearly polarized light). The phenomena of CD and OR are intimately related by Kramers-Kronig relations and are collectively known as "optical activity" [1, 70]. CD and OR are well-established spectroscopic techniques to probe enantiomeric excess in chemical samples. Interestingly, optical activity is not restricted to samples involving chiral molecules, but can also arise in a material that interacts with a static magnetic field parallel to the propagation direction of light. To distinguish the optical activity due to a magnetic field from that due to the breakdown of molecular inversion symmetry, the former so-called magneto-optical (MO) effects are known as magnetic CD (MCD) and magnetic OR (MOR) or the Faraday effect, respectively. MCD is an important spectroscopic technique that allows one to resolve electronic transitions in congested absorption bands [2, 3], while MOR is a phenomenon that is routinely exploited in the fabrication of optical devices such

as isolators and circulators [2, 71, 9].

The fundamental origin of MO effects is the breakdown of time-reversal symmetry (TRS). It is therefore reasonable that phenomena analogous to MO effects could arise from replacing a static magnetic field with time-varying electric fields; we shall hereafter term them pseudo-MO effects. In molecular spectroscopy, these phenomena have been long recognized since the pioneering work of Atkins and Miller [72]. More recently, within the context of topological photonics and nonreciprocal media, much attention has been directed towards exploiting time-varying modulation of material permittivities as a way to generate synthetic gauge ("pseudo-magnetic") fields, thereby circumventing magnetic field strengths that could be prohibitive in general experimental setups or difficult to integrate in optoelectronic devices. In fact, photonic versions of the Aharonov-Bohm (AB) effect [73] and quantum Hall systems [74, 75, 76] have been experimentally demonstrated. The AB effect was observed for photons using a Ramsey-type interferometer [77], while topologically protected photonic edge states were observed in arrays constructed from optical ring resonators [78]. A hallmark of TRS breaking is the realization of AB phases that differ from 0 or $\pi \bmod 2\pi$. This version of AB phase is astutely realized in Reference [79] by driving resonators in adjacent unit cells so that there is a large phase lag between them, a feature that is facilitated by the relatively big mesoscopic length scales of the experimental system of interest. Thus, it is not obvious *a priori* whether such a strategy would be feasible in the recreation of pseudo-magnetic fields in molecular aggregates or in general nanoscale scenarios, especially considering the lengthscale mismatch between the typical interatomic or intermolecular distances and the optical wavelength of the driving field. However, as we shall show in the present article, such a mismatch can be compensated by invoking rings of coherently coupled anisotropic nanoscale molecular dipoles which simultaneously interact with an elliptically polarized laser field, such that different molecules interact with distinct linear polarizations of the laser and consequently pick up distinct phases from the light to break TRS. Our work follows a similar spirit to other theoretical proposals where an optically induced AB effect can be achieved in both electronic [80] and excitonic [81, 82] nanoscopic ring structures

by exploiting circularly polarized electric fields to break TRS. However, in these cases, the AB phase varies with field strength, while in our case the AB phase solely depends on the phase imprinted by the ellipticity of the field.

We present a theoretical proof-of-principle of the possibility of inducing synthetic gauge fields in the excitonic degrees of freedom of small cyclic molecular aggregates. In particular, we design a setup consisting of an isotropic ensemble of molecular homotetramers, where each of the sites has an internal vibronic structure with low-frequency (e.g., vibrational) transitions that are driven by a near-resonant electric field. Owing to the periodicity of the laser-driving, we employ Floquet theory [83, 84, 85] to calculate the spectral properties of the driven system according to a recently developed methodology [86]. These Floquet engineering concepts are complementary to efforts using strong magnetic fields to dramatically alter the vibronic structure and consequently the optical properties of molecular aggregates [87], as well as to the design of topologically nontrivial phases in organic excitonic systems [88]. Although by no means a new technique, Floquet engineering is regaining interest in the development of materials with novel properties [89], and in the proposal of using Floquet engineering to influence both energy [90] and electron transfer [91] in molecular systems. In particular, our study highlights the simplicity with which large values of AB phases can be Floquet engineered with time-varying electric fields in nanoscale systems (as shown below, with weak laser intensities), in contrast with the difficulties of deploying giant magnetic fields to generate similarly large values of AB phases. Hence, our results suggest much flexibility in the use of elliptically polarized light in the realization of excitonic AB phases in molecular systems, which could control a variety of charge and energy transfer processes in molecular aggregates or manipulate the spectroscopic properties of the latter. While excitonic AB phases that depend on the separation between electrons and holes have been studied in inorganic Wannier exciton systems [92, 93, 94, 95, 96], similar phases in Frenkel organic exciton systems are far less explored (see Reference [88] for an example) and constitute an interesting frontier in physical chemistry.

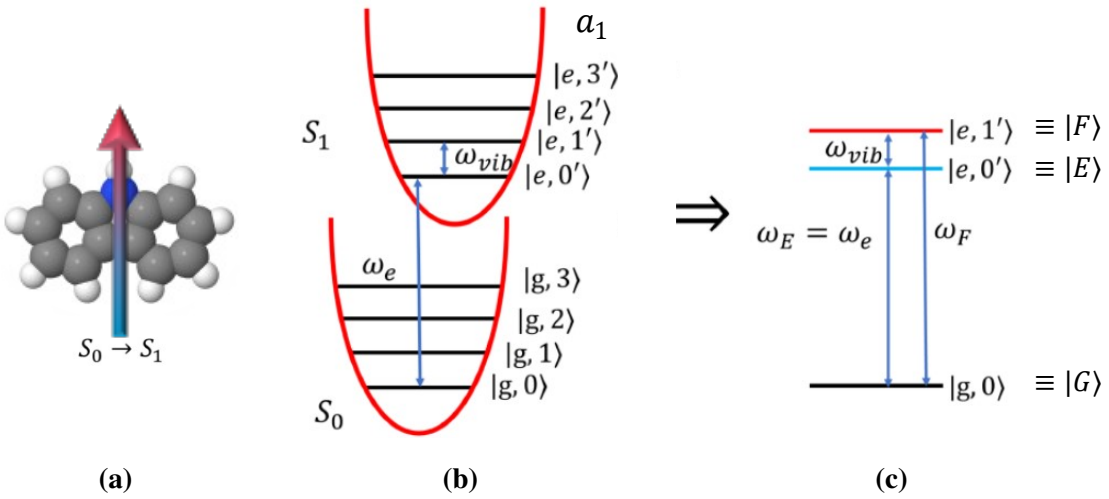

Figure 2.1. *Carbazole monomer*: (a) Molecular structure and dipole moment vector corresponding to the $S_0 \rightarrow S_1$ transition. (b) Simplified displaced harmonic oscillator spectrum of carbazole along the low-frequency vibrational mode ($\omega_{vib} = 211$ cm^{-1}). Here, $\omega_e = 30,300$ cm^{-1} is the $0-0$' electronic transition frequency, and D $= 0.348$ is the Huang$-$Rhys parameter for vibronic coupling. (c) In this work, we simplify the spectrum in part (b) with a three$-$level model.

2.2 Theoretical formalism

2.2.1 Definition of excitonic model

The building block of our molecular aggregates is a carbazole molecule, depicted in Figure 2.1. We shall only be concerned with its $S_0 \rightarrow S_1$ electronic transition (with 0-0' frequency $\omega_e = 30,300\,\text{cm}^{-1}$ and oscillator strength $f = 0.042$ [97]) which is coupled to a low-frequency a_1 mode ($\omega_{vib} = 211\,\text{cm}^{-1}$ [98]); the Huang-Rhys factor that characterizes the displacement of the S_1 potential energy surface with respect to the S_0 surface is $D = 0.348$ [99]. The weak vibronic coupling featured by this transition allows us to simplify the carbazole spectrum as an effective three-level system featuring ground $|g,0\rangle$ and excited $|e,0'\rangle$ electronic states with no phonons, and an excited $|e,1'\rangle$ electronic state with one phonon, where $|g\rangle$ and $|e\rangle$ denote S_0 and S_1 electronic states, and $|v\rangle$ and $|v'\rangle$ label vibrational eigenstates of the harmonic potentials corresponding to S_0 and S_1, respectively (see Figure 2.1).

For simplicity, let us consider a homotetramer where the chromophores are located at

the vertices of a square of side length $a = 3.5\,\text{Å}$ (see Figure 2.2), mimicking the value reported from an ultrafast spectroscopy study of anthracene dimers involving vibrational coherences [100] (previous theoretical studies addressing how to control excitation-energy transfer by manipulation ultrafast vibrational dynamics [101, 102] where fitted to the aforementioned experimental data). To unclutter notation, we introduce the following single-excitation basis:

$$|G\rangle = \prod_{i=1}^{4} |g_i, 0_i\rangle, \tag{2.1a}$$

$$|E_j\rangle = |e_j, 0'_j\rangle \prod_{i\neq j}^{4} |g_i, 0_i\rangle, \tag{2.1b}$$

$$|F_j\rangle = |e_j, 1'_j\rangle \prod_{i\neq j}^{4} |g_i, 0_i\rangle. \tag{2.1c}$$

The excitonic Hamiltonian of the homotetramer reads ($\hbar = 1$)

$$\begin{aligned} H_T = &\sum_{i=1}^{4} \Big(\omega_E |E_i\rangle\langle E_i| + \omega_F |F_i\rangle\langle F_i| \Big) \\ &+ \sum_{\langle ij \rangle} \Big[(J_{E_i,E_j} |E_i\rangle\langle E_j| + J_{E_i,F_j} |E_i\rangle\langle F_j| + J_{F_i,F_j} |F_i\rangle\langle F_j|) + \text{h.c.} \Big], \end{aligned} \tag{2.2}$$

where the sum over $\langle ij \rangle$ assumes only nearest-neighbor couplings. Here $\omega_E = \omega_e$ and $\omega_F = \omega_e + \omega_{vib}$, and $J_{\alpha\beta} = J_{\beta\alpha}$ are the electrostatic couplings between excitonic states $|\alpha\rangle$ and $|\beta\rangle$, which are calculated assuming the Condon approximation [103, 104], *e.g.*,

$$J_{E_i,F_j} = \langle e_i g_j | H_T | g_i e_j \rangle \langle 0'_i | 0_i \rangle \langle 0_j | 1'_j \rangle, \tag{2.3}$$

where

$$\langle e_i g_j | H_T | g_i e_j \rangle = \eta \frac{(\hat{\mu}_i \cdot \hat{\mu}_j) - 3(\hat{\mu}_i \cdot \hat{r}_{ij})(\hat{\mu}_j \cdot \hat{r}_{ij})]}{a^3} \tag{2.4}$$

is approximated as the classical dipole-dipole interaction, with $\hat{\mu}_i$ being the unit vector of the

electronic transition dipole moment for the $S_0 \rightarrow S_1$ transition for the i-th chromophore and $\hat{r}_{ij}$ being the unit vector that connects chromophores i and j. The value $\eta = 982\,\mathrm{cm}^{-1}\,\mathrm{\AA}^3$ has been invoked to account for the effects of transition dipole magnitudes as well as the index of refraction of the surrounding medium, so that the dipolar coupling between parallel carbazole molecules $\langle e_i g_j | H_T | g_i e_j \rangle = \frac{\eta}{a^3} = 22.9\,\mathrm{cm}^{-1}$ is similar to the value used in theoretical studies of anthracene dimers [101, 102] that is consistent with quantum beat data in ultrafast spectroscopy experiments [100]. The scalar $|\langle n_i' | 0_i \rangle|^2 = \exp[-D]\frac{D^n}{n!}$ is the relevant Franck-Condon factor [103]. In this work, we fix the orientations of μ_2 and μ_4 to be along the $\hat{x}$ and $\hat{y}$ axes, respectively, in the molecular aggregate frame, while we vary the orientations of μ_1 and μ_3 at angles θ_1 and θ_3 (Figure 2.2a shows $\theta_1 = 45^0$ and $\theta_3 = 315^0$). For simplicity, we ignore out-of-plane dipole orientations; this is not a necessary condition and could be easily lifted if chemical synthesis favors other geometries. The excitonic transition dipole moments from the ground state, $|G\rangle$, are $\mu_{E_i G} = \langle E_i | \mu | G \rangle = \langle e_i, 0_i' | \mu | g_i, 0_i \rangle$ and $\mu_{F_i G} = \langle F_i | \mu | G \rangle = \langle e_i, 1_i' | \mu | g_i, 0_i \rangle$. In our calculations we take $\langle e_i, 0_i' | \mu | g_i, 0_i \rangle = 1.7\,\mathrm{D}$ and $\langle e_i, 1_i' | \mu | g_i, 0_i \rangle = 0.85\,\mathrm{D}$, values which are consistent with experiments [97].

Given that $J_{\alpha\beta} \ll \omega_{vib}$, the exciton eigenstates of H_T consist of two bands centered at ω_E and ω_F, respectively, with bandwidths $\sim 2\max|J_{E_i E_j}|$, $\sim 2\max|J_{F_i F_j}|$. Figure 2.3 shows the absorption spectrum of an isotropically averaged collection of homotetramers. Notice that due to different Franck-Condon overlaps, the splitting of the band at ω_F is narrower than that at ω_E. Note, that there are multiple vibronic eigenstates whose symmetries result in net zero transition dipole moments; that is, they are dark with respect to UV-visible light in the absence of laser driving. Accordingly, these states cannot be observed using absorption spectroscopy, which is why there are fewer peaks in the spectrum than the number of possible eigenstates of H_T.

2.2.2 Floquet theory for laser-driving

The aforementioned two bands can be mixed upon the introduction of a driving laser; the new Hamiltonian is time-dependent and reads

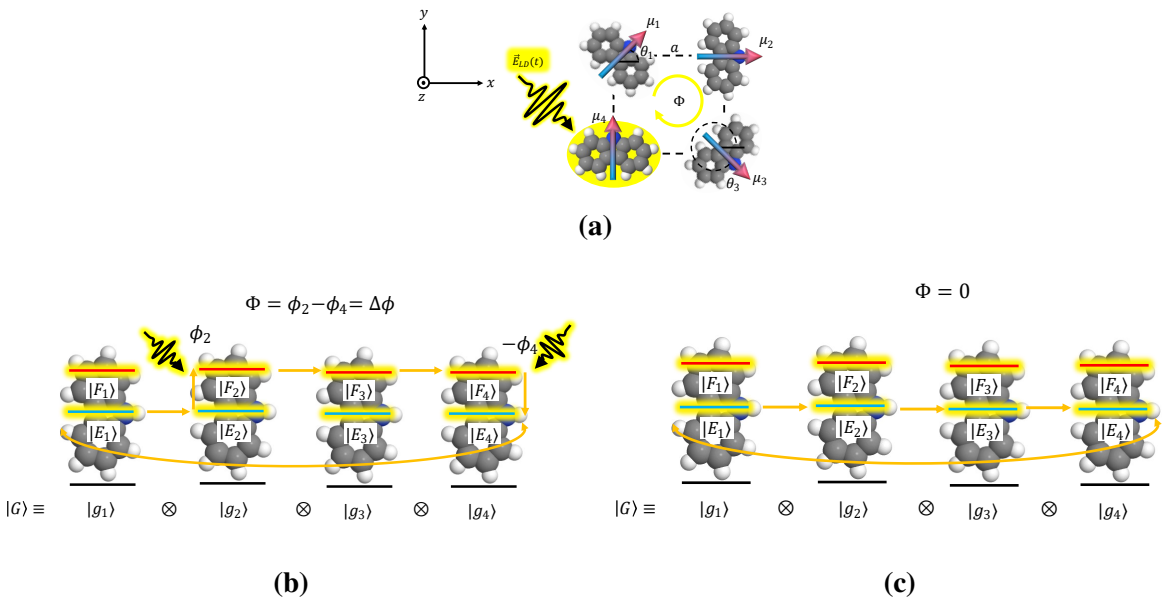

Figure 2.2. *Realization of excitonic Aharonov-Bohm (AB) effect in cyclic molecular aggregates via Floquet engineering with elliptically polarized light*: (a) Example geometry of a carbazole homotetramer where relative orientations (θ_1, θ_3) of transition dipoles together with laser-driving induces an excitonic AB phase Φ. The carbazole monomers are equidistantly placed at a distance a from their neighbors forming a square. (b,c) Schematic illustrations of the mechanism whereby Floquet engineering induces excitonic AB phases. The elliptically polarized field $E_{LD}(t)$ drives the $|E_i\rangle \rightarrow |F_i\rangle$ low-frequency vibrational transition (vertical yellow arrows). Horizontal yellow arrows denote excitonic couplings mediated by electrostatic interactions. In (b1), excitation of the first chromophore at $|E_1\rangle$ is resonantly transferred to the second chromophore $|E_2\rangle$ via a dipolar coupling. Next, the laser promotes the $|E_2\rangle \rightarrow |F_2\rangle$ vibrational excitation, "dialing" phase ϕ_2 onto that transition. Subsequent excitation transfer $|F_2\rangle \rightarrow |F_3\rangle \rightarrow |F_4\rangle$ occurs via resonant dipolar couplings, after which the laser promotes the $|F_4\rangle \rightarrow |E_4\rangle$ vibrational emission, dialing phase $-\phi_4$ onto that transition. Finally another step of resonant dipole-mediated excitation transfer $|E_4\rangle \rightarrow |E_1\rangle$ closes the loop, yielding an AB phase $\Phi = \phi_2 - \phi_4$. $\Phi \neq n\pi$ for integer n signals time-reversal symmetry breaking. Meanwhile (b2) illustrates a pathway mediated by electrostatic interactions (and no influence from laser-driving) that does not result in a nontrivial AB phase.

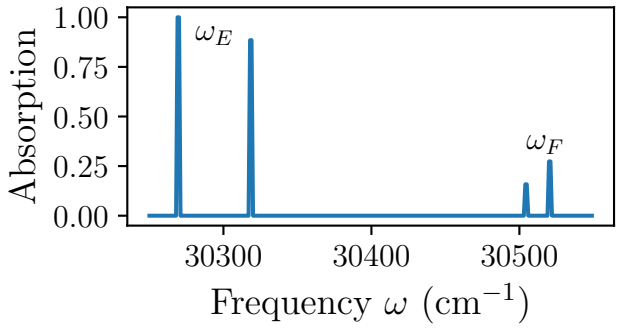

Figure 2.3. *Absorption spectrum of an isotropic solution of excitonic homotetramers*: It can be approximately understood as consisting of two bands of transitions corresponding to coherent combinations of 0-0' transitions (centered at ω_E) and 0-1' transitions (centered at ω_F) respectively. The splitting of each of these bands is due to resonant exciton hopping between molecules, and correspond to $\sim 2\max|J_{E_iE_j}|$ and $\sim 2\max|J_{F_iF_j}|$, respectively.

$$H_{LD}(t) = H_T - \sum_{i=1}^{4}(\mu_{E_iF_i} \cdot \overrightarrow{E}_{LD}(t)|E_i\rangle\langle F_i| + \text{h.c.}), \tag{2.5}$$

where we have introduced an infrared (IR) field at a frequency $\Omega = \omega_{vib} + \delta$ that is slightly detuned from the $E_i \to F_i$ vibrational transitions by δ:

$$\overrightarrow{E}_{LD}(t) = \frac{E^0_{LD}}{\sqrt{2}}[\hat{x}\cos(\Omega t + \phi_x) + \hat{y}\cos(\Omega t + \phi_y)]. \tag{2.6}$$

The detuning δ allows us to ignore resonant pumping of vibrational transitions in the ground state (Figure 2.1b) so that the three-level approximation per molecule (Figure 2.1c) is justified. The phases ϕ_x and ϕ_y will play an important role below. The relevant transition dipole moments to the laser-driving are $\mu_{F_iE_i} = \langle F_i|\mu|E_i\rangle = \langle e_i, 1'_i|\mu|e_i, 0'_i\rangle$ and we take $|\mu_{F_iE_i}| = 0.15\,\text{Debye}$, which is a reasonable value for IR molecular vibrational excitations [105].

For completeness, we shall now lay out the Floquet theory [83, 84, 85] utilized to address the problem in question. The Hamiltonian $H_{LD}(t)$ is periodic in time with period $T = 2\pi/\Omega$ such

that $H_{LD}(t+T) = H_{LD}(t)$. The solutions to the time-dependent Schrödinger equation (TDSE)

$$i\frac{d}{dt}|\Psi(t)\rangle = H_{LD}(t)|\Psi(t)\rangle \tag{2.7}$$

can be written in the Floquet state basis $|\Psi(t)\rangle = \sum_\lambda C_\lambda |\psi_\lambda(t)\rangle$ where

$$|\psi_\lambda(t)\rangle = e^{-i\varepsilon_\lambda t}|\phi_\lambda(t)\rangle. \tag{2.8}$$

The Floquet modes can be spectrally decomposed in the single (molecular) excitation basis, $\alpha \in \{G, E_i, F_i\}$ where $i \in \{1,2,3,4\}$, introduced in Eq. (2.1),

$$|\phi_\lambda(t)\rangle = \sum_\alpha |\alpha\rangle\langle\alpha|\phi_\lambda(t)\rangle, \tag{2.9}$$

and are periodic in time with period T. Furthermore, they are eigenfunctions of the Floquet Hamiltonian

$$H_F|\phi_\lambda(t)\rangle = \left[H_{LD}(t) - i\frac{d}{dt}\right]|\phi_\lambda(t)\rangle = \varepsilon_\lambda|\phi_\lambda(t)\rangle, \tag{2.10}$$

where the eigenvalues $\{\varepsilon_\lambda\}$ are known as quasi-energies. Since $|\phi_\lambda(t)\rangle$ and $H_{LD}(t)$ are time-periodic, we can write Eqs. (2.5) and (2.9) in terms of their Fourier components:

$$|\phi_\lambda(t)\rangle = \sum_\alpha \sum_{n=-\infty}^{\infty} |\alpha\rangle\langle\alpha|\phi_\lambda^{(n)}\rangle e^{in\Omega t}, \tag{2.11a}$$

$$\langle\alpha|H_{LD}(t)|\beta\rangle = \sum_{n=-\infty}^{\infty} H_{LD,\alpha\beta}^{(n)} e^{in\Omega t}, \tag{2.11b}$$

where $H_{LD,\alpha\beta}^{(n)} = \frac{1}{T}\int_0^T dt\langle\alpha|H_{LD}(t)|\beta\rangle e^{-in\Omega t}$. By substituting Eqs. (2.11a) and (2.11b) into Eq. (2.10), multiplying both sides of the resulting equation by $\exp(-ik\Omega t)$, and taking a time-integral over one period T, we obtain

$$\sum_{\beta n} H_{F\alpha\beta}^{(k-n)} \langle \beta | \phi_\lambda^{(n)} \rangle = \varepsilon_\lambda \langle \alpha | \phi_\lambda^{(k)} \rangle, \tag{2.12a}$$

$$H_{F\alpha\beta}^{(k-n)} = H_{LD,\alpha\beta}^{(k-n)} + n\Omega \delta_{\alpha\beta} \delta_{kn}. \tag{2.12b}$$

At this point, we augment the Hilbert space from $|\alpha\rangle$ to $|\alpha\rangle \otimes |t\rangle$, where $\langle t|\phi_\lambda\rangle = |\phi_\lambda(t)\rangle$, and introduce the Fourier basis $\{|n\rangle\}$ where $\langle n|\phi_\lambda\rangle \equiv |\phi_\lambda^{(n)}\rangle$, $\langle t|n\rangle = e^{in\Omega t}$, $|\alpha, n\rangle \equiv |\alpha\rangle|n\rangle$, and $\langle \alpha, k|H_F|\beta, n\rangle \equiv H_{F\alpha\beta}^{(k-n)}$, rendering the eigenvalue problem into the following form:

$$H_F|\phi_\lambda\rangle = \left[H_F^{(0)} + H_F^{(1)}\right]|\phi_\lambda\rangle = \varepsilon_\lambda|\phi_\lambda\rangle, \tag{2.13a}$$

$$\begin{aligned} H_F^{(0)} = \sum_{n=-\infty}^{\infty} \Big\{ \sum_{i=1}^{4} \Big[(\omega_E + n\Omega)|E_i, n\rangle\langle E_i, n| + (\omega_F + n\Omega)|F_i, n\rangle\langle F_i, n| \Big] + n\Omega|G, n\rangle\langle G, n| \\ + \sum_{\langle ij \rangle} \Big[(J_{E_i,E_j}|E_i, n\rangle\langle E_j, n| + J_{E_i,F_j}|E_i, n\rangle\langle F_j, n| + J_{F_i,F_j}|F_i, n\rangle\langle F_j, n|) + \text{h.c.} \Big] \Big\}, \end{aligned} \tag{2.13b}$$

$$H_F^{(1)} = -\frac{E_{LD}^0}{\sqrt{2}} \sum_{n=-\infty}^{\infty} \Big\{ \sum_{i=1}^{4} \sum_{q=\hat{x},\hat{y}} \Big[\mu_{E_iF_i}^q \big(e^{i\phi_q}|E_i, n\rangle\langle F_i, n+1| + e^{-i\phi_q}|E_i, n+1\rangle\langle F_i, n| \big) + \text{h.c} \Big] \Big\}. \tag{2.13c}$$

An intuitive interpretation of this basis, which was originally presented by Shirley [83], comes from associating n to the number of quanta present in the laser-driving mode; e.g., $|E_1, 3\rangle$ would refer to the state were the exciton corresponds to the 0-0' transition in the first chromophore while the field contains three photons. Following this interpretation, Eq. (2.13b) denotes that intermolecular interactions between excitonic states preserve photon number, while Eq. (2.13c) shows that the driving field couples states $|E_i\rangle, |F_i\rangle$ by either absorbing or emitting a photon. To

gain further insight, we consider the limit where

$$|J_{E_iF_j}|, |\mu_{LD} \cdot E_{LD}(t)| \ll \Omega, \tag{2.14}$$

so that we can apply the rotating-wave approximation (RWA) to drop highly off-resonant terms; Eqs. (2.13b) and (2.13c) can then be reduced to

$$\begin{aligned} H_F^{(0)} \approx \sum_{n=-\infty}^{\infty} \Big\{ \sum_{i=1}^{4} \Big[(\omega_E + n\Omega)|E_i,n\rangle\langle E_i,n| + (\omega_F + n\Omega)|F_i,n\rangle\langle F_i,n| \Big] + n\Omega|G,n\rangle\langle G,n| \\ + \sum_{\langle ij \rangle} \Big[(J_{E_i,E_j}|E_i,n\rangle\langle E_j,n| + J_{F_i,F_j}|F_i,n\rangle\langle F_j,n|) + \text{h.c.} \Big] \Big\} \end{aligned} \tag{2.15a}$$

$$H_F^{(1)} \approx -\frac{E_{LD}^0}{\sqrt{2}} \sum_{n=-\infty}^{\infty} \Big\{ \sum_{i=1,q}^{4} \Big[\mu_{E_iF_i}^q e^{-i\phi_q} |E_i,n+1\rangle\langle F_i,n| + \text{h.c.} \Big] \Big\}. \tag{2.15b}$$

The RWA invokes a physically intuitive constraint: the laser-driving intensity is weak enough that it can only induce the $|E_i\rangle \to |F_i\rangle$ transition if the exciton absorbs a photon from the field. Furthermore, the RWA block-diagonalizes Eq. (2.13a) so that $H_F \approx \sum_n (h_{F,n} + h_{G,n})$ where the n-th blocks $h_{G,n}$ and $h_{F,n}$ are defined as:

$$h_{G,n} = n\Omega|G,n\rangle\langle G,n|, \tag{2.16a}$$

$$\begin{aligned} h_{F,n} = \sum_{i=1}^{4} \Big[(\omega_E + (n+1)\Omega)|E_i,n+1\rangle\langle E_i,n+1| + (\omega_F + n\Omega)|F_i,n\rangle\langle F_i,n| \Big] \\ + \sum_{\langle ij \rangle} \Big[(J_{E_i,E_j}|E_i,n+1\rangle\langle E_j,n+1| + J_{F_i,F_j}|F_i,n\rangle\langle F_j,n|) + \text{h.c.} \Big] \\ - \frac{E_{LD}^0}{\sqrt{2}} \sum_{i=1,q}^{4} \Big[\mu_{E_iF_i}^q e^{-i\phi_q} |E_i,n+1\rangle\langle F_i,n| + \text{h.c} \Big]. \end{aligned} \tag{2.16b}$$

Note that the Floquet states $\{|\psi_\lambda(t)\rangle\}$ are uniquely characterized by the quasi-energies ε_λ mod Ω [85, 83]; therefore, within the RWA, we only need to diagonalize one $h_{F,n}$ block and

one $h_{G,n}$ block to find a finite set of Floquet modes $\{|\phi_\lambda\rangle\}$ to construct the Floquet state basis $\{|\psi_\lambda(t)\rangle\}$. We should note that Eq. (2.16b) resembles a lattice Hamiltonian where the quantum degrees of freedom are influenced by a gauge field $\vec{A}(r)$ [106], where $\phi_q = \int \vec{A}(r)\cdot dr$. Typically, the latter arises from a magnetic field coupling to movable charges, resulting in AB phases; in our case, we shall see that the gauge field is a result of the elliptically polarized laser, which can be thought of as a pseudo-magnetic field.

2.2.3 Calculation of circular dichroism spectrum

To calculate the CD signal of the laser-driven system, we invoke the formalism developed in Reference [86]. We compute the rates of absorption $W_\pm(\omega)$ due to weak-intensity continuous-wave circularly polarized probe laser fields at UV-visible frequency ω,

$$E_{P\pm}(\omega,t) = \frac{E_P^0}{\sqrt{2}}(\hat{x}\cos\omega t \pm \hat{y}\sin\omega t).$$

The CD response at each frequency ω is defined as $S(\omega) = \frac{\delta W(\omega)}{W_+(\omega)+W_-(\omega)}$, where $\delta W(\omega)$ is the difference in the rates due to RCP and LCP light:

$$\delta W(\omega) = -|E_p^0|^2\pi \mathrm{Im}\left[\sum_{\lambda,\alpha,\beta}\sum_{n=-\infty}^{\infty}\mu^y_{\alpha G}\langle\phi_\lambda|\alpha n\rangle\mu^x_{G\beta}\langle\beta n|\phi_\lambda\rangle\delta(\varepsilon_\lambda - n\Omega - \omega)\right]. \tag{2.17}$$

Here $\varepsilon_\lambda - n\Omega$ denotes the $|Gn\rangle \to |\phi_\lambda\rangle$ transition energy, where $|\phi_\lambda\rangle$ is an eigenstate of $h_{F,1}$ or $h_{G,1}$ (see Eqs. (2.16a), (2.16b)) with eigenvalue ε_λ, and ω is the energy absorbed from the probe. Note that $\mu_{GG} = 0$ and, due to the RWA, $h_{F,1}$ only couples the states $|E_i,2\rangle$ and $|F_i,1\rangle$. Therefore, $\langle\alpha,n|\phi_\lambda\rangle \neq 0$ only for $n = 1,2$, which results in Eq. (2.17) being simplified to

$$\begin{aligned}\delta W(\omega) = -|E_p^0|^2\pi \mathrm{Im}\Bigg[\sum_\lambda\sum_{ij}\Big\{&\mu^y_{E_iG}\langle\phi_\lambda|E_i2\rangle\mu^x_{GE_j}\langle E_j2|\phi_\lambda\rangle\delta(\varepsilon_\lambda - 2\Omega - \omega)\\ &+\mu^y_{F_iG}\langle\phi_\lambda|F_i1\rangle\mu^x_{GF_j}\langle F_j1|\phi_\lambda\rangle\delta(\varepsilon_\lambda - \Omega - \omega)\Big\}\Bigg].\end{aligned} \tag{2.18}$$

Eq. (2.18) corresponds to a single homotetramer of fixed orientation. Since we are interested

in an isotropic film or solution of such aggregates, we must take an average of $\delta W(\omega)$ and $W(\omega)_+ + W_-(\omega)$ over different orientations of the tetramer with respect to the incident light k vector. The average CD response is then

$$\langle S(\omega)\rangle = \frac{\int_0^{2\pi}\int_0^{2\pi}\int_0^{\pi} d\chi d\psi d\theta \delta W(\omega;\chi,\psi,\theta)\sin\theta}{\int_0^{2\pi}\int_0^{2\pi}\int_0^{\pi} d\chi d\psi d\theta [W_+(\omega;\chi,\psi,\theta)+W_-+(\omega;\chi,\psi,\theta)]\sin\theta}, \tag{2.19}$$

where we have explicitly written $\delta W(\omega) = \delta W(\omega;\chi,\psi,\theta)$ and $W_\pm(\omega) = W_\pm(\omega;\chi,\psi,\theta)$ to express the fact that the CD for each aggregate is a function of its orientation, defined by Tait-Bryan angles χ, ψ, θ [107] (see Figure 2.4). Notice that unlike with perturbative spectroscopy [108], we cannot analytically carry out this average given that $h_{F,1}$ is a function itself of χ, ψ, θ, as each orientation experiences a different driving due to its different dipole projections with the IR laser. Hence, we compute the isotropically averaged CD spectrum in Eq. (2.19) via Monte Carlo integration (see A.1).

2.3 Results

2.3.1 Excitonic AB phases

To illustrate the nontrivial effects produced by Floquet engineering, we now consider coherent pathways due to the various terms in Eq. (2.16). In particular, we are interested in cyclic ones, namely, those which begin and end in the same state. For concreteness, let us focus on the pathway depicted in Figure 2.2b1. Excitation of the first chromophore at $|E_1\rangle$ is resonantly transferred to the second chromophore $|E_2\rangle$ via dipolar coupling. Next, the elliptically polarized driving laser promotes the $|E_2\rangle \to |F_2\rangle$ vibrational excitation, imprinting a nontrivial phase ϕ_2 onto that transition. Subsequent excitation transfer via dipolar coupling $|F_2\rangle \to |F_3\rangle \to |F_4\rangle$ is followed by a laser-induced vibrational de-excitation $|F_4\rangle \to |E_4\rangle$, which imprints yet another nontrivial phase ϕ_4; the pathway is closed by another dipolar coupling $|E_4\rangle \to |E_1\rangle$. To make these statements more precise, let us define the Wilson loop [109] corresponding to this pathway:

$$
\begin{aligned}
\mathscr{W} &= \langle E_1 n|h_{F,n}|E_4 n+1\rangle\langle E_4 n+1|h_{F,n}|F_4 n\rangle\langle F_4 n|h_{F,n}|F_3 n\rangle \\
&\times \langle F_3 n|h_{F,n}|F_2 n\rangle\langle F_2 n|h_{F,n}|E_2 n+1\rangle\langle E_2 n+1|h_{F,n}|E_1 n+1\rangle \\
&= J_{E_1E_2}\left(\sum_{q=\hat{x},\hat{y}}\frac{E^0_{LD}\mu^q_{E_2F_2}}{\sqrt{2}}e^{i\phi_q}\right)J_{F_2F_3} \\
&\times J_{F_3F_4}\left(\sum_{q=\hat{x},\hat{y}}\frac{E^0_{LD}\mu^q_{E_2F_2}}{\sqrt{2}}e^{-i\phi_q}\right)J_{E_4E_1}. \qquad (2.20)
\end{aligned}
$$

If we define

$$
\phi_2 = \arg\left[J_{E_1E_2}\left(\sum_{q=\hat{x},\hat{y}}\frac{E^0_{LD}\mu^q_{E_2F_2}}{\sqrt{2}}e^{i\phi_q}\right)J_{F_2F_3}\right], \qquad (2.21)
$$

$$
\phi_4 = -\arg\left[J_{F_3F_4}\left(\sum_{q=\hat{x},\hat{y}}\frac{E^0_{LD}\mu^q_{E_2F_2}}{\sqrt{2}}e^{-i\phi_q}\right)J_{E_4E_1}\right], \qquad (2.22)
$$

the excitonic AB phase corresponding to this pathway is equal to $\Phi = \arg(W) = \phi_2 - \phi_4$. To gain further intuition on the types of transition dipole arrangements that lead to substantial values of Φ, let us consider the configuration in Figure 2.2a, where the dipoles in chromophores 2 and 4 are aligned along $\hat{x}$ and $\hat{y}$ respectively, and the only positive dipolar couplings within our gauge convention is $J_{F_2F_3}$; then, $\phi_2 = \phi_x + \pi$ and $\phi_4 = -\phi_y - 2\pi = -\phi_y$, so that the phases of the elliptically polarized field are explicitly imprinted in the resulting excitonic AB phase

$$
\Phi = \arg(\mathscr{W}) = \phi_x - \phi_y + \pi = \Delta\phi + \pi. \qquad (2.23)
$$

A few comments are pertinent at this point. When $\Delta\phi = 0 \bmod \pi$, the driving laser corresponds to linearly polarized light and the AB phase $\Phi = 0, \pi$ is trivial; this is expected as TRS is preserved. However, when $\Delta\phi \neq 0 \bmod \pi$, the driving laser corresponds to elliptically polarized light, leading to a nontrivial AB phase $\Phi \neq 0, \pi$ ($\Delta\phi = \frac{\pi}{2} \bmod \pi$ corresponds to the special case

of circular polarization) that signals TRS breaking. Hence, our design crucially depends on chromophores 2 and 4 obtaining different phases ϕ_x and ϕ_y from the laser-driving; to maximize this difference, they are placed perpendicular to one another. However, the production of a nontrivial AB phase relies also on having coherent dipolar couplings throughout the aggregate that yield a nonzero Wilson loop. To ensure that chromophores 2 and 4 are coupled, chromophores 1 and 3 are positioned along optimal orientations $\frac{\hat{x}\pm\hat{y}}{\sqrt{2}}$ so that the exciton hoppings are enough to ensure large coherent couplings throughout the cycle. It follows that to realize an exciton AB phase $\Phi = \frac{\pi}{2}$, one simply needs to set $\Delta\phi = -\frac{\pi}{2}$, corresponding to right circularly polarized light. At this point, it is worth highlighting that this excitonic AB phase is independent of laser intensity so long as the RWA is a good approximation. This should be contrasted with the magnitudes of the magnetic fields used to generate an AB phase $\Phi = \frac{\pi}{2}$ in a nanoscale ring supporting electronic currents. In fact, considering a putative loop of the same area a^2 as our molecular aggregate, $\Phi = \frac{eBa^2}{\hbar}$ [73] would require $B = 8400\,\text{Tesla}$ (an intensity that is only feasible at present in restricted places such as white dwarfs! [110]). This remark implies that it should be substantially easier to realize AB phases in nanoscale systems by employing Floquet engineering via time-varying laser electric fields over giant static magnetic fields. Thus, these versatile Floquet engineered AB phases could open doors to new ways of coherently controlling excitonic processes in molecules and nanomaterials.

Our proposal to induce AB phases via Floquet engineering is heavily influenced by Reference [79], where the authors suggest the periodic modulation of permittivities in arrays of coherently coupled resonators to generate pseudo-magnetic fields. Crucial to their setup is a well-crafted spatial distribution of modulation phases which is locally controlled with electrical circuit elements. This local control of phases is possible in mesoscopic systems but much harder to realize in the nanoscale. In fact, one could be tempted to think that light-matter interaction is ineffective in doing so, given the mismatch between the lengthscale of light and molecules. However, as we show in our example above, we achieve the distribution of modulation phases by exploiting (a) the phase lag between the $\hat{x}$ and $\hat{y}$ components of the electric field of elliptically

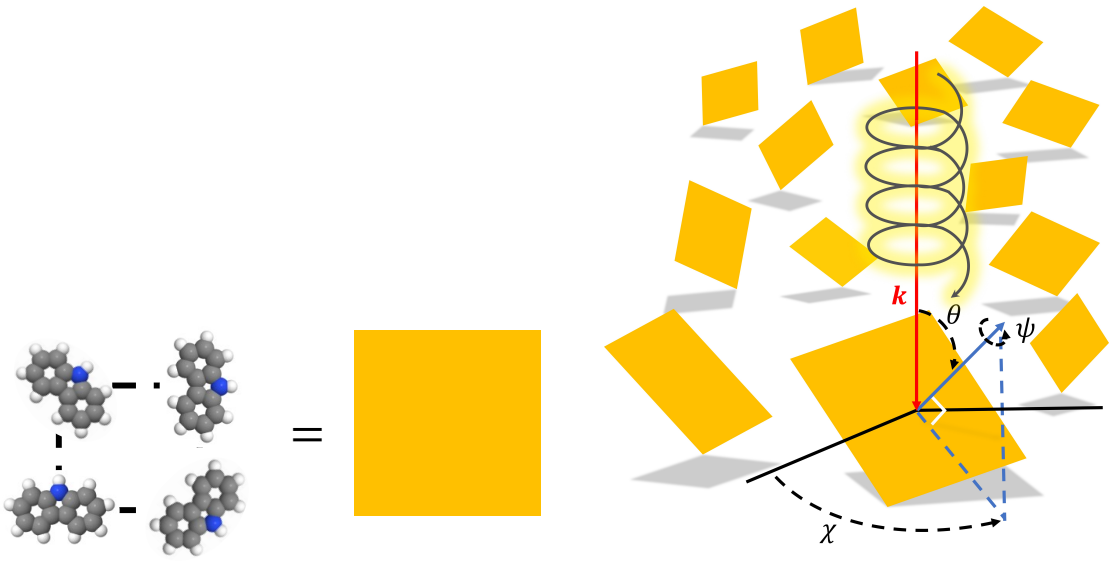

(a) (b)

Figure 2.4. *Orientational averaging of excitonic homotetramers*: (a) Excitonic homotetramer unit. (b) Depiction of an isotropic ensemble of homotetramers; calculation of circular dichroism (CD) involves averaging over orientations χ, θ, ψ with respect to the k vector of the incident beam. Here, the normal vector to the molecular aggregate plane (blue arrow) is uniquely defined by the polar coordinates θ and χ, while ψ is the angle of rotation of the aggregate about the aforementioned vector. Note that the ellipticity of the incident beam is not represented to scale with respect to the molecular aggregates.

polarized laser light and (b) by designing rings of coherently coupled molecular dipoles where different sites feature orientations that interact with different polarizations of the laser light.

2.3.2 Features of the CD spectrum

To test the effects of TRS breaking due to nontrivial excitonic AB phases, Figure 2.5 shows the isotropic averaged CD spectrum. For our simulations, we use $E^0_{LD} = 2.7 \times 10^8 \frac{V}{m}$, which is a standard value utilized in Floquet engineering experiments with inorganic semiconductors[111], and take $\delta = -0.1\omega_{vib}$. With these parameters we obtain $\frac{|\mu_{LD} \cdot E_{LD}(t)|}{\Omega} = 0.02$, which satisfies the requirement of Eq. (2.14) above. As expected, when $\Delta\phi = 0, \pi$, $\langle S(\omega) \rangle$ vanishes for all ω: TRS is preserved under linearly polarized light driving. However, arbitrary elliptically polarized fields ($\Delta\phi \neq 0, \pi$) give rise to nonzero CD, where a clear pattern of sign switches occurs at the TRS

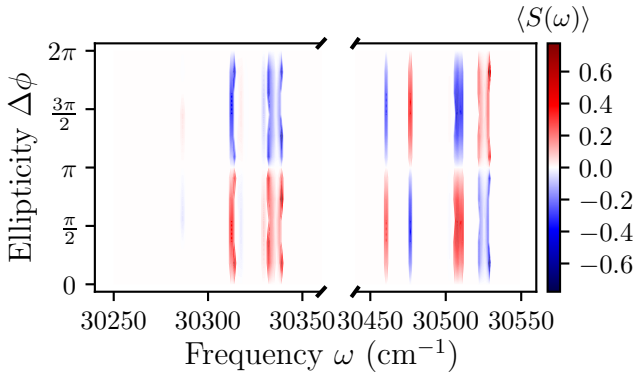

Figure 2.5. *Computed circular dichroism (CD) spectrum for isotropic ensemble of carbazole-homotetramers under the influence of elliptically-polarized driving*: Clear progressions of the CD as a function of ellipticity $\Delta\phi$ can be observed, with sign switches at the time-reversal-symmetry (TRS) points $\Delta\phi = 0, \pi$. Note we have inserted a break in the frequency axes in order to highlight the CD signal about ω_E and ω_F.

points. Notice that despite the laser-driving being weak in comparison to its carrier frequency, $|\mu_{LD} \cdot E_{LD}(t)| \ll \Omega$ (see Eq. (2.14)), the small shifts in peak frequencies in Figure 2.3 give rise to substantial CD signals, just as in MCD, where moderate values of magnetic fields can easily dissect congested spectra [2, 3]. Also note that the maximum absolute value of $\langle S(\omega)\rangle$ occurs at $\Delta\phi = \frac{\pi}{2}, \frac{3\pi}{2}$, which corresponds to circularly polarized light. Based on the mechanism outlined in the previous subsection (see also Figures 2.2a, b), we attribute this symmetry to the fact that in our homotetramer, the dipoles are all of the same magnitude.

2.4 Conclusion

In this article, we have demonstrated that Floquet engineering with elliptically polarized laser fields can serve as an alternative to magnetic fields to induce pseudo-MO effects in molecular systems and nanomaterials. These phenomena should be regarded as complementary to MCD and MOR effects in molecular systems. Small cyclic molecular aggregates with an anisotropic arrangement of transition dipoles can support a wide range of excitonic AB phases upon elliptically polarized laser driving despite the small areas they enclose. A rich ellipticity-dependent modulation of energy level splittings ensues, which concomitantly manifests in widely

tunable CD spectra. Within the program of harnessing coherence in light-harvesting systems [112, 113, 114, 115] and AB effects in quantum tunneling [116], our study emphasizes the potential that AB phases have in the coherent control of energy and charge transport in molecular aggregates, as well as in the decongestion of spectra of the latter. While we have previously proposed the realization of excitonic AB phases in topologically protected porphyrin arrays [88], such effects have been barely explored in a broader range of systems and they could be appealing as a way to switch exciton couplings and propagation direction on demand with lasers rather than by synthetic modification. Moreover, we have recognized that in the nanoscale, Floquet engineering is a dramatically less challenging tool than using magnetic fields to realize AB effects. In fact, the nanoscale excitonic AB phases that arise in our designed system depend on the pump laser ellipticity $\Delta\phi$ and not on its field strength; thus a large phase of $\Phi = \frac{\pi}{2}$ can in principle be readily realized in our protocol. This ease must be contrasted with the prohibitive magnetic fields that must be used in nanorings to induce an electronic AB phase of the same magnitude (we must mention, however, ingenious molecular electronics proposals to harness small AB phases arising from weak magnetic fields to induce substantial control on electronic currents [117]). Furthermore, it is important to emphasize that while general features of pseudo-MO and MO effects are similar (they both arise from breaking of TRS), they cannot be easily compared [72]: the former depends on the coupling of time-varying electric fields with electric transition dipole moments, while the latter arises from the interaction of static magnetic fields with the spin and orbital angular momentum of molecular eigenstates. Yet, we suspect that pseudo-MO effects could provide a convenient alternative in situations where magnetic fields are experimentally unfeasible.

This work has laid the foundations for the generation of exciton AB phases in molecular aggregates. However, a detailed exploration of the dissipative effects of a condensed phase environment must be addressed to ensure the experimental feasibility of our predictions in a wide range of experimental scenarios. Broadly speaking, we expect exciton AB phases to be resilient to decoherence as long as the light-matter coupling $|\mu_{LD} \cdot E_{LD}(t)|$ and the excitonic couplings

$|J_{\alpha\beta}|$ are stronger than the spectral linewidths caused by the environment. These issues, together with the additional effects of intramolecular vibrations, will be addressed in future work.

Note.– After the initial submission of the manuscript, we were made aware of an important reference by Phuc and Ishizaki [91], which proposes Floquet engineering to control the chirality of electron transfer in molecular trimers. While the conclusions in that work are similar to the present, the AB phase in their work is due to linearly polarized light with two driving frequencies and amplitudes, rather than due to elliptically polarized light. While no isotropic averaging effects were discussed in that work, the authors carried out a thorough exploration of the effects of decoherence and concluded that chiral currents survive in the condensed phase. Further comparison of both strategies to induce AB phases will be the subject of future studies.

Chapter 2, in full, is adapted from the material as it appears in "Optical activity from the exciton Aharonov–Bohm effect: A Floquet engineering approach," by K. Schwennicke and J. Yuen-Zhou, *J. Phys. Chem. C.* **124.7**, 42026-4214 (2020) [66]. The adaptations made here were informed by and aligned with corrections provided in "Corrections to 'Optical activity from the exciton Aharonov–Bohm effect: A Floquet engineering approach,"' by K. Schwennicke and J. Yuen-Zhou, *J. Phys. Chem. C.* **126.36**, 15547-15548 (2022) [118], which was published subsequently. These adaptations were introduced because we realized that although the qualitative basis of our model is correct, its application to anthracene is erroneous. Specifically, in our model, we want to drive a Fanck–Condon (FC) active mode, which is a totally symmetric mode, with an infrared (IR) laser. This is not possible for anthracene, which belongs to the D_{2h} point group, because the totally symmetric mode, a_g, is IR inactive (it does not transform as x, y, or z). For the totally symmetric mode to be IR active, the molecule must lack an inversion center. An example of such a molecule is carbazole (see Figure 2.1). The dissertation author was the primary investigator and author of these papers.

Chapter 3

Enantioselective topological frequency conversion

3.1 Introduction

In the mid-nineteenth century, Louis Pasteur discovered that molecules can possess handedness, or chirality, an attribute that influences how they interact with their surroundings [119]. More generally, the two species of a chiral molecule, referred to as enantiomers, are non-superimposable mirror images of each other and, while they feature many identical physicochemical properties (up to very small parity violation corrections [120]), they can also exhibit drastically different behavior when exposed to chiral environments or stimuli. Thus, enantioselectivity plays a crucial role in biological activity as well as in the synthesis, purification, and characterization of pharmaceuticals [121, 122, 123]. Traditionally, optical rotation and circular dichroism have served as optical tools to obtain enantioselective information; however, these techniques rely on the weak interaction between molecules and the magnetic component of the optical field. A very active effort in chirality research consists of spatially shaping electromagnetic fields [124, 125, 126] to enhance these weak interactions. Other techniques that rely solely on electric dipole interactions [127] have been recently advocated. For instance, many efforts are currently invested in photoelectron circular dichroism (PECD) [128, 129, 130, 131]. Yet, others focus on nonlinear optical signals that depend on the sign of the electric fields with which the molecules interact [132, 133], including photoexcitation circular dichroism

[134], the use of synthetic chiral fields [5, 6, 135, 136], and microwave three-wave mixing [7, 8, 137, 138, 139]. More precisely, the latter technique can be understood through cyclic three-level models [140, 141, 142, 143, 144, 145, 146] where the product of three light-matter couplings [hereafter referred to as the Král-Shapiro (KS) product] differs by a phase of π between the two enantiomers. This remarkable symmetry has been exploited to propose cyclic population transfer schemes [140, 146] or the use of cross-polarized terahertz pulses [147] to prepare the enantiomers in different energy configurations or orientations for separation. This symmetry has also been utilized to suggest an enantioselective generalization of the Stern-Gerlach [148] or spin Hall [149] experiments, where spatial separation of enantiomers, rather than spins, is achieved using artificial gauge fields [150, 151, 152]. The analogy between enantiomer and spin labels is intriguing and surprisingly underexplored, and serves as the motivation for our present work. More specifically, we wish to demonstrate an enantioselective analogue to the Quantum Spin Hall Effect (QSHE) [153].

On the other hand, since the pioneering work of Thouless, Kohmoto, Nightingale, and den Nijs in relation to the Quantum Hall Effect (QHE) [154], notions of symmetry-protected topological phases (SPTPs) have been at the heart of condensed matter research, and have only been exacerbated in the past fifteen years with the discovery of topological insulators [155]. These notions guarantee that certain response properties of so-called topologically nontrivial systems are largely independent of material specification, instead depending only on products of universal constants and integer quantities known as topological invariants. The discrete nature of these properties implies that they are robust against material imperfections, thus making them attractive for metrology, among other applications. While topological protection was originally identified in translationally invariant 2D systems, its scope has been enlarged through the use of Floquet engineering in systems of different dimensionality [156, 157, 158, 89] and the consideration of the 2D phase space of 1D systems [159, 160]. Of particular interest is an elegant construction due to Martin, Refael, and Halperin [161] called topological frequency conversion (TFC), where quantized "current" is observed. In this Letter, we design a novel spectroscopic

scheme that generalizes TFC to the microwave spectroscopy of an ensemble of chiral molecules. The very first link between chiroptical spectroscopy and topology was suggested recently in work by Ordóñez and Smirnova [162] within the context of PECD. These authors showed that the propensity field (a pseudoscalar) as a function of ejected photoelectron direction (Berry curvature) can be integrated over all solid angles to yield a quantized enantiosensitive flux which is proportional to a Chern number. Similarly, the authors showed that microwave three-wave mixing signals can be interpreted in terms of an analogous quantity to the propensity field [127]. However, it is not clear from that work if there exists a parameter space upon which integration of the signals leads to topological invariants, so geometric and topological consequences of these nonlinear spectroscopies were not explored. In this Letter, we use TFC to identify time as the missing parameter space and for simplicity, restrict our attention to frequency conversion rather than three-wave mixing. The result is a signal that is proportional to enantiomeric excess (EE), with a simple prefactor containing the sign of the KS product. Owing to the topological nature of the signal, it should also serve as a very sensitive detection of EE. As far as we are aware, our work provides the first connection between topological physics, chiroptical spectroscopy, and nonlinear spectroscopy, and anticipates a fertile ground for further exploration.

3.2 Theory

3.2.1 Model

Following the principles of enantioselective microwave three-wave mixing [163, 164], we treat the enantiomers as asymmetric tops whose Hamiltonian is

$$H_0 = AJ_a^2 + BJ_b^2 + CJ_c^2, \tag{3.1}$$

where J_a, J_b, J_c are the angular momentum operators with respect to the principal axes $\hat{a}$, $\hat{b}$, $\hat{c}$, and $A > B > C$ are the corresponding rotational constants. The eigenstates are labeled as $|J,\tau,M\rangle$, where $J = 0,1,2...$ is the rotational quantum number, $M = -J, -J+1, -J+2, ..., J$ is

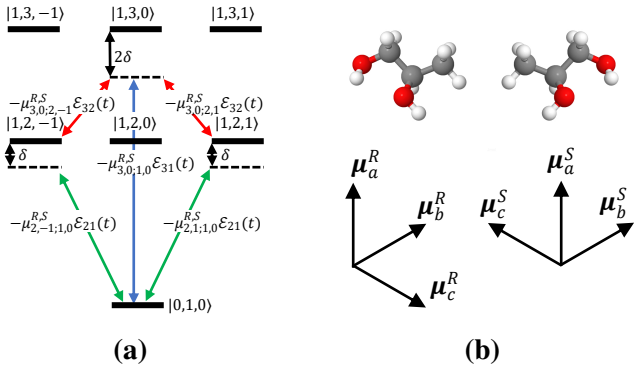

Figure 3.1. *Asymmetric top model*: (a) Cyclic three-level transitions for an asymmetric top, such as enantiomers. Three near-resonant, linear polarized lasers with modulated field amplitudes $\mathscr{E}_{ij}(t)$ interact with these transitions. (b) The principal axes components of the dipole moments for the $R-$ and $S-$1,2-propanediol enantiomers. Note that $(\mu^R_a\cdot\hat{a})(\mu^R_b\cdot\hat{b})(\mu^R_c\cdot\hat{c}) = -(\mu^S_a\cdot\hat{a})(\mu^S_b\cdot\hat{b})(\mu^S_c\cdot\hat{c})$

the quantum number that characterizes the projection of the total angular momentum along the z-laboratory-fixed axis, and τ serves as the quantum number to differentiate between states with the same J and M. We consider the following low angular momentum eigenstates of Eq. 3.1 with a rotational quantum number of $J = 0$ or $J = 1$

$$\begin{aligned} &|0,\tau = 1,0\rangle,\\ &|1,\tau = 2,M\rangle,\\ &|1,\tau = 3,M\rangle, \end{aligned} \tag{3.2}$$

where $M = -1,0,1$ [165] (see B.1). The ground state $|0,\tau = 1,0\rangle$, with energy $\hbar\varepsilon_1$, and the excited states $|1,\tau = 2,M\rangle$ and $|1,\tau = 3,M\rangle$, with energies $\hbar\varepsilon_2$, $\hbar\varepsilon_3$, respectively, are coupled to each other using a set of three orthogonally-polarized time-dependent electric fields

$$\begin{aligned} \mathbb{E}_{21}(t) &= \mathscr{E}_{21}(t)\sin(\Omega_{21}t)\hat{y},\\ \mathbb{E}_{32}(t) &= \mathscr{E}_{32}(t)\cos(\Omega_{32}t)\hat{x},\\ \mathbb{E}_{31}(t) &= \mathscr{E}_{31}(t)\cos(\Omega_{31}t)\hat{z}, \end{aligned} \tag{3.3}$$

where $\hat{x}$, $\hat{y}$, $\hat{z}$ denote the three laboratory-fixed axes, the frequencies $\Omega_{21} = \varepsilon_2 - \varepsilon_1 - \delta$, $\Omega_{32} = \varepsilon_3 - \varepsilon_2 - \delta$, $\Omega_{31} = \varepsilon_3 - \varepsilon_1 - 2\delta$, are slightly detuned from the system's natural frequencies, and the field amplitudes $\mathscr{E}_{21}(t)$, $\mathscr{E}_{32}(t)$, $\mathscr{E}_{31}(t)$ are slowly modulated. Note from the selection rules for electric dipole interactions [164], that $\Delta M = 0$ for the z polarized field and $\Delta M = \pm 1$ for the x and y polarized field (see Fig. 3.1). Ignoring all states that are not coupled through the driving electric fields, and assuming that $|\mu^{R,S}_{i,M';j,M}\mathscr{E}_{ij}(t)|/2 \ll \hbar\Omega_{ij}$, the Hamiltonian for the laser dressed $R-$ and $S-$enantiomer, after making the rotating wave approximation, is

$$\begin{aligned} H^{R,S}(t) = &\sum_{i=1,3} \hbar\varepsilon_i |i,0\rangle\langle i,0| + \hbar\varepsilon_2 \sum_{M=\pm1} |2,M\rangle\langle 2,M| \\ &- \mathscr{E}_{21}(t) \sum_{M=\pm1} \Big(\frac{i\mu^{R,S}_{2,M;1,0} e^{-i\Omega_{21}t}}{2} |2,M\rangle\langle 1,0| + \text{h.c.} \Big) \\ &- \mathscr{E}_{32}(t) \sum_{M=\pm1} \Big(\frac{\mu^{R,S}_{3,0;2,M} e^{-i\Omega_{32}t}}{2} |3,0\rangle\langle 2,M| + \text{h.c.} \Big) \\ &- \mathscr{E}_{31}(t) \Big(\frac{\mu^{R,S}_{3,0;1,0} e^{-i\Omega_{31}t}}{2} |3,0\rangle\langle 1,0| + \text{h.c.} \Big), \end{aligned} \tag{3.4}$$

where for simplicity we have introduced the notation $|1,0\rangle \equiv |0,\tau = 1,0\rangle$, $|2,M\rangle \equiv |1,\tau = 2,M\rangle$, $|3,0\rangle \equiv |1,\tau = 3,0\rangle$. In Eq. 3.4 $\mu^{R,S}_{i,M';j,M}$ is the component of the transition-dipole moment for the $|j,M\rangle \rightarrow |i,M'\rangle$ transition that is projected along the polarization axis of $\mathbb{E}_{ij}(t)$. Following the procedure of Refs. [163, 164], the values of $\mu^{R,S}_{i,M';j,M}$ are

$$\begin{aligned} \mu^{R,S}_{2,\pm1;1,0} &= -\frac{i\mu^{R,S}_b}{\sqrt{6}}, \\ \mu^{R,S}_{3,0;2,\pm1} &= \frac{\mu^{R,S}_a}{2\sqrt{2}}, \\ \mu^{R,S}_{3,0;1,0} &= -\frac{i\mu^{R,S}_c}{\sqrt{3}}, \end{aligned} \tag{3.5}$$

where $\mu^{R,S}_a$, $\mu^{R,S}_b$, $\mu^{R,S}_c$ are the components of the dipole moment along the principal molecular axes. These components are real valued and $|\mu^R_{a,b,c}| = |\mu^S_{a,b,c}|$. Note that for the chosen polar-

izations for the three electric fields (see Eq. 3.3) and studied energy levels, $\mu^{R,S}_{i,M';j,M}$ does not depend on the quantum number M. The associated time-dependent wavefunction for the $R-$ and $S-$ enantiomer the system is $|\psi^{R,S}(t)\rangle$.

Next, we consider the rotating frame

$$U(t) = e^{-i(\varepsilon_2-\Omega_{21})t}|1,0\rangle\langle 1,0| + \sum_{M=\pm 1} e^{-i\varepsilon_2 t}|2,M\rangle\langle 2,M| + e^{-i(\varepsilon_2+\Omega_{32})t}|3,0\rangle\langle 3,0|, \tag{3.6}$$

such that $|\psi^{R,S}(t)\rangle = U(t)|\tilde{\psi}^{R,S}(t)\rangle$, in order to remove the central frequencies Ω_{ij}. In this frame, $i\hbar\partial_t|\tilde{\psi}^{R,S}(t)\rangle = \mathscr{H}^{R,S}(t)|\tilde{\psi}^{R,S}(t)\rangle$, with the effective Hamiltonian:

$$\mathscr{H}^{R,S}(t) = \frac{1}{2}\begin{pmatrix} -2\hbar\delta & -\frac{\mu_b^{R,S}}{\sqrt{6}}\mathscr{E}_{21}(t) & -\frac{\mu_b^{R,S}}{\sqrt{6}}\mathscr{E}_{21}(t) & -\frac{i\mu_c^{R,S}}{\sqrt{3}}\mathscr{E}_{31}(t) \\ -\frac{\mu_b^{R,S}}{\sqrt{6}}\mathscr{E}_{21}(t) & 0 & 0 & -\frac{\mu_a^{R,S}}{2\sqrt{2}}\mathscr{E}_{32}(t) \\ -\frac{\mu_b^{R,S}}{\sqrt{6}}\mathscr{E}_{21}(t) & 0 & 0 & -\frac{\mu_a^{R,S}}{2\sqrt{2}}\mathscr{E}_{32}(t) \\ \frac{i\mu_c^{R,S}}{\sqrt{3}}\mathscr{E}_{31}(t) & -\frac{\mu_a^{R,S}}{2\sqrt{2}}\mathscr{E}_{32}(t) & -\frac{\mu_a^{R,S}}{2\sqrt{2}}\mathscr{E}_{32}(t) & 2\hbar\delta \end{pmatrix}. \tag{3.7}$$

After a change of basis (see B.2), we arrive at the following effective Hamiltonian

$$\begin{aligned}\mathscr{H}^{R,S}(t) = &-\frac{\mu_b^{R,S}\mathscr{E}_{21}(t)}{2\sqrt{3}\hbar}L_x - \frac{\mu_a^{R,S}\mathscr{E}_{32}(t)}{4\hbar}L_y \\ &+ \frac{\mu_c^{R,S}\mathscr{E}_{31}(t)}{2\sqrt{3}\hbar}L_z - \frac{\delta}{2\hbar}(L_+^2 + L_-^2)\end{aligned} \tag{3.8}$$

where $L_x = \frac{\hbar}{\sqrt{2}}\begin{pmatrix} 0 & 1 & 0 \\ 1 & 0 & 1 \\ 0 & 1 & 0 \end{pmatrix}$, $L_y = \frac{\hbar}{\sqrt{2}}\begin{pmatrix} 0 & -i & 0 \\ i & 0 & -i \\ 0 & i & 0 \end{pmatrix}$, $L_z = \hbar\begin{pmatrix} 1 & 0 & 0 \\ 0 & 0 & 0 \\ 0 & 0 & -1 \end{pmatrix}$ are the angular momentum operators for a spin-1 particle and $L_+ = \sqrt{2}\hbar\begin{pmatrix} 0 & 1 & 0 \\ 0 & 0 & 1 \\ 0 & 0 & 0 \end{pmatrix}$, $L_- = \sqrt{2}\hbar\begin{pmatrix} 0 & 0 & 0 \\ 1 & 0 & 0 \\ 0 & 1 & 0 \end{pmatrix}$ are the corresponding ladder operators. We use the form of the effective Hamiltonian in Eq. 3.8 to calculate the topology of the system. Hereafter, we will assume that the slowly-modulated

electric field amplitudes are

$$\begin{aligned}
\mathscr{E}_{21}(t) &= E_{21}\sin(\omega_1 t),\\
\mathscr{E}_{32}(t) &= E_{32}\sin(\omega_2 t),\\
\mathscr{E}_{31}(t) &= E_{31}[m-\cos(\omega_1 t)-\cos(\omega_2 t)],
\end{aligned} \tag{3.9}$$

where ω_1 and ω_2 are two modulation frequencies, and m is a scalar that characterizes a non-modulated component of the electric field. These functional forms are inspired by the TFC scheme reported in Ref. [166].

3.3 Results

3.3.1 Enantioselective TFC

For completeness, we briefly rederive the TFC formalism using adiabatic perturbation theory (the original paper does so within Floquet theory [161]). In the rotating frame, the rate of the system's energy absorption for the enantiomers is given by

$$\partial_t E^{R,S}(t) = \langle\tilde{\psi}^{R,S}(t)|\partial_t \mathscr{H}^{R,S}(t)|\tilde{\psi}^{R,S}(t)\rangle. \tag{3.10}$$

In the long time limit, $t\to\infty$, the time-averaged energy-absorption rate, or average power, is

$$\mathscr{P}_{av}^{R,S} = \lim_{t\to\infty}\frac{1}{t}\int_0^t dt'\partial_{t'}E^{R,S}(t') = \sum_{\omega_i}\mathscr{P}_{av}^{R,S}(\omega_i), \tag{3.11a}$$

$$\mathscr{P}_{av}^{R,S}(\omega_i) = \lim_{t\to\infty}\frac{1}{t}\int_0^t dt'\omega_i\langle\partial_{\omega_i t'}\mathscr{H}^{R,S}(t')\rangle, \tag{3.11b}$$

where $\mathscr{P}_{av}^{R,S}(\omega_i)$ is the average power at the modulation frequency ω_i.

Let $|\varepsilon_l^{R,S}(t)\rangle$ denote the $l-$th adiabatic state of $\mathscr{H}^{R,S}(t)$, where $\mathscr{H}^{R,S}(t)|\varepsilon_l^{R,S}(t)\rangle = \varepsilon_l^{R,S}(t)|\varepsilon_l^{R,S}(t)\rangle$ (Fig. 3.2). If ω_1,ω_2 are incommensurate, *i.e.*, ω_1/ω_2 is irrational, $\mathscr{H}^{R,S}(t)$ is not periodic. However, if we write $\mathscr{H}^{R,S}(t) = \mathscr{H}^{R,S}(\theta) = \mathscr{H}^{R,S}(\theta_1,\theta_2)$ with $\theta_i = \omega_i t\,(\mathrm{mod}\,2\pi)$, we

notice that $\mathscr{H}^{R,S}(\theta)$ is quasiperiodic, $\mathscr{H}^{R,S}(\theta_1+2\pi,\theta_2)=\mathscr{H}^{R,S}(\theta_1,\theta_2+2\pi)=\mathscr{H}^{R,S}(\theta_1,\theta_2)$, and the domain of $\mathscr{H}^{R,S}(\theta_1,\theta_2)$ is a two-dimensional torus $\mathbb{T}=[0,2\pi)\otimes[0,2\pi)$. Near the adiabatic limit where ω_1, ω_2 are much smaller than the instantaneous energy gap of $\mathscr{H}^{R,S}(t)$, and if the system is initiated in the $l-$th adiabatic state, *i.e.,* $|\tilde{\psi}^{R,S}(0)\rangle=|\varepsilon_l^{R,S}(0)\rangle$, the expected quantities $\langle\partial_{\omega_1 t}\mathscr{H}^{R,S}(t)\rangle$ and $\langle\partial_{\omega_2 t}\mathscr{H}^{R,S}(t)\rangle$ for $|\tilde{\psi}^{R,S}(t)\rangle$, to first order in ω_1 and ω_2 are

$$\langle\partial_{\omega_1 t}\mathscr{H}^{R,S}(t)\rangle=\langle\partial_{\theta_1}\mathscr{H}^{R,S}(\theta)\rangle=\partial_{\theta_1}\varepsilon_l^{R,S}(\theta)-\hbar\omega_2 F_l^{R,S}(\theta) \tag{3.12a}$$

$$\langle\partial_{\omega_2 t}\mathscr{H}^{R,S}(t)\rangle=\langle\partial_{\theta_2}\mathscr{H}^{R,S}(\theta)\rangle=\partial_{\theta_2}\varepsilon_l^{R,S}(\theta)+\hbar\omega_1 F_l^{R,S}(\theta) \tag{3.12b}$$

where $F_l^{R,S}(\theta)=i\langle\partial_{\theta_1}\varepsilon_l^{R,S}(\theta)|\partial_{\theta_2}\varepsilon_l^{R,S}(\theta)\rangle+\text{h.c.}$ is the Berry curvature of the $l-$th adiabatic state (see B.4).

According to the mean-value theorem for incommensurate ω_1 and ω_2 [167], the linear flow of θ covers the torus densely for long enough times. Thus, the time average of $F_l^{R,S}(t)$ is the same as the average of $F_l^{R,S}(\theta)$ over the entire torus $\mathbb{T}$:

$$\lim_{t\to\infty}\frac{1}{t}\int_0^t dt' F_l^{R,S}(t')=\frac{1}{4\pi^2}\int_{\mathbb{T}}d\theta F_l^{R,S}(\theta). \tag{3.13}$$

From a practical standpoint, $t\to\infty$ means $t>p\frac{2\pi}{\omega_1}=q\frac{2\pi}{\omega_2}$, where $\frac{\omega_1}{\omega_2}\approx\frac{p}{q}$ for $p,q\in\mathbb{Z}^+$. Substituting Eqs. 3.12a and 3.12b into Eq. 3.11b gives rise to the average power lost by the fields at ω_1 and ω_2 when the system is initiated in the $l-$th adiabatic state, $\mathscr{P}_{av}^{R,S}(\omega_1)=-\mathscr{P}_{av}^{R,S}(\omega_2)=-\frac{\hbar\omega_1\omega_2 C_l^{R,S}}{2\pi}$. Here the average of $\partial_{\theta_i}\varepsilon_l^{R,S}(\theta)$ is zero since $\varepsilon_l^{R,S}(\theta)$ is quasiperiodic in θ, and $C_l^{R,S}=\frac{1}{2\pi}\int_{\mathbb{T}}d\theta F_l^{R,S}(\theta)$ is the Chern number of the $l-$th adiabatic state for the corresponding enantiomer. Thus, the enantiomer dependent average energy-pumping rate between the two modulation fields $\mathscr{P}_{2\to1}^{R,S}=[\mathscr{P}_{av}^{R,S}(\omega_2)-\mathscr{P}_{av}^{R,S}(\omega_1)]/2$ is quantized,

$$\mathscr{P}_{2\to1}^{R,S}=\frac{\hbar\omega_1\omega_2 C_l^{R,S}}{2\pi}, \tag{3.14}$$

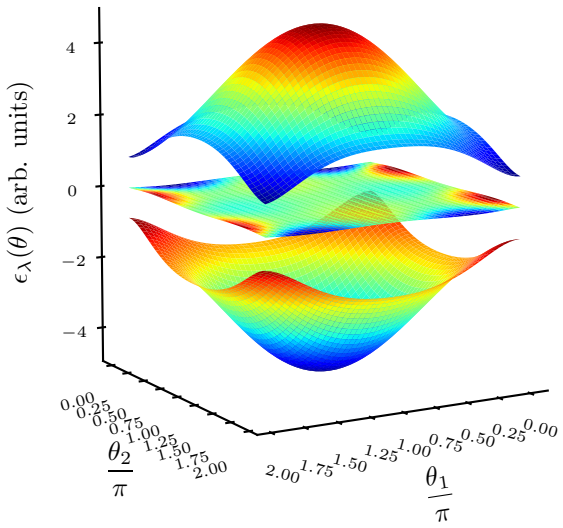

Figure 3.2. *Example adiabatic states giving rise to enantioselective TFC*: The color gradient is a visual aid for the band dispersion.

or in other words, after one period of the ω_2 modulation, $C_l^{R,S}$ photons with frequency ω_1 are produced. The photons produced are in the same spatial modes as the incoming electric fields. The very off-resonant nature of this process guarantees that the molecule does not retain energy and the energy transfer process occurs only between the fields.

For $\delta = 0$, $\mathscr{H}^{R,S}(\theta)$ (see Eq. 3.8), resembles half of the Bernevig-Hughes-Zhang Hamiltonian [168], except that the Pauli matrices are replaced with the spin-1 angular momentum operators. As expected, $\mathscr{H}^{R,S}(\theta)$ is topologically non-trivial for $|m| < 2$, where the Chern numbers for the upper (U) and lower (L) adiabatic states remarkably acquire the value

$$C_U^{R,S} = 2\mathrm{sgn}(m)\mathrm{sgn}(\mathscr{O}^{R,S}) = -C_L^{R,S}, \tag{3.15}$$

and that for the middle (M) band $C_M = 0$ (for an analytical proof, see B.5). Here $\mathscr{O}^{R,S} = (\mu_b^{R,S}E_{12})(\mu_a^{R,S}E_{23})(\mu_c^{R,S}E_{31})$ is the KS product which obeys the enantioselective symmetry relation $\mathscr{O}^R = -\mathscr{O}^S$, since $\mu_a^R\mu_b^R\mu_c^R = -\mu_a^S\mu_b^S\mu_c^S$, and we have assumed that $E_{ij} = E_{ji}$. Therefore

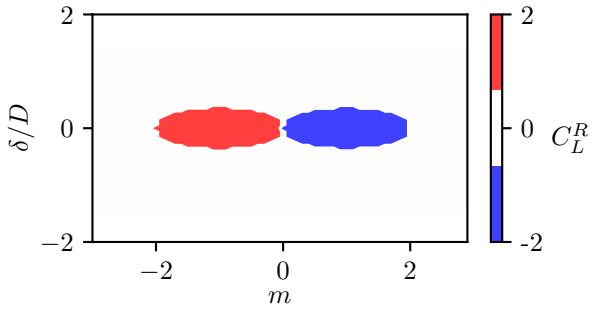

Figure 3.3. *Topological phase diagram*: The value of C_L^R is calculated by taking the magnitudes of the light-matter couplings to be equal, *i.e.*, $|\mu^R_{2,M';1M}E_{21}| = |\mu^R_{3,M';2,M}E_{32}| = |\mu^R_{3,M';1,M}E_{31}| = \hbar D$, while the laser-driving parameters m and δ are varied. We obtain $C_L^R = -2\mathrm{sgn}(m)\mathrm{sgn}(\mathscr{O}^R)$ at the vicinity of $\delta = 0$, where $\mathscr{O}^R = -\mathscr{O}^S$ is the Král-Shapiro product, which is enantioselective.

$C_L^R = -C_L^S$, and the TFC for the two enantiomers initiated in the lower (upper) adiabatic band at $t = 0$ is expected to have the same magnitude but opposite sign, *i.e.*, $\mathscr{P}^R_{2\to1} = -\mathscr{P}^S_{2\to1}$. This result begs us to consider the fruitful analogy between enantiomer label and spin degrees of freedom. Just like in the QSHE, where the transverse conductivity for opposite spins bears opposite signs, so does the TFC for opposite enantiomers. Eq. 3.15 is the central result of this work and relates a fundamental topological invariant from chiroptical spectroscopy ($\mathrm{sgn}\mathscr{O} = \pm1$) with the notions of SPTPs. Fig. 3.3 shows the computed value of C_L^R for different values of m when $\delta \neq 0$.

By analogy with Eq. 3.11, we can compute the enantiomer dependent average power absorbed in the original frame as $P^{R,S}_{av}(\Omega) = \lim_{t\to\infty}\frac{1}{t}\int_0^t dt'\Omega\langle\partial_{\Omega t'}H^{R,S}(t')\rangle$, obtaining:

$$\frac{\mathscr{P}^{R,S}_{av}(\omega_1)}{\hbar\omega_1} = \frac{P^{R,S}_{av}(\Omega_{21+1})}{\hbar\Omega_{21+1}} - \frac{P^{R,S}_{av}(\Omega_{21-1})}{\hbar\Omega_{21-1}} + \frac{P^{R,S}_{av}(\Omega_{31+1})}{\hbar\Omega_{31+1}} - \frac{P^{R,S}_{av}(\Omega_{31-1})}{\hbar\Omega_{31-1}}, \tag{3.16a}$$

$$\frac{\mathscr{P}^{R,S}_{av}(\omega_2)}{\hbar\omega_1} = \frac{P^{R,S}_{av}(\Omega_{32+2})}{\hbar\Omega_{32+2}} - \frac{P^{R,S}_{av}(\Omega_{32-2})}{\hbar\Omega_{32-2}} + \frac{P^{R,S}_{av}(\Omega_{31+2})}{\hbar\Omega_{31+2}} - \frac{P^{R,S}_{av}(\Omega_{31-2})}{\hbar\Omega_{31-2}}, \tag{3.16b}$$

where $\Omega_{ij\pm1,2} = \Omega_{ij} \pm \omega_{1,2}$. Thus, the quantization due to the enantioselective TFC can be

extracted from an experimentally detected difference power spectrum of the fields interacting with the molecule. Notice that the topology is preserved for $\delta \neq 0$ as long as $\hbar|\delta| < |\mu^{R,S}_{i,M';j,M}E_{ij}|/2$. In general, we expect our scheme to maintain the nontrivial topology with respect to changes in experimental conditions (such as laser spot size or collection efficiency) so long as adiabaticity still holds and the necessary peaks in the power spectrum can be resolved.

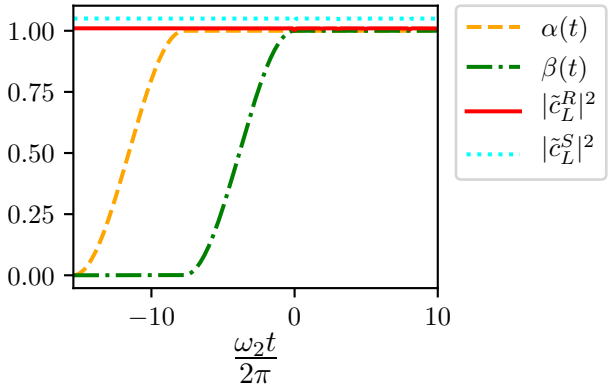

Figure 3.4. *Adiabatic state preparation*: Presented are the plots for the functions $\alpha(t)$ and $\beta(t)$. We also feature the populations $|\tilde{c}^R_L|^2$, $|\tilde{c}^S_L|^2$ (shifted vertically slightly to be visible) of the lower adiabatic state for each enantiomer. As shown, the system is effectively prepared in the lower adiabatic bands for both enantiomers.

3.3.2 Numerical results

The dynamics of the system are calculated by numerically integrating the Schrödinger equation in the rotating frame (Eq. 3.7), and the power spectrum is obtained by returning to the original frame. In atomic units ($\hbar = 1$), the electric field amplitudes are taken to be $E_{21} = 5\sqrt{3}E_0$, $E_{32} = 6E_0$, $E_{31} = \sqrt{3}E_0$, where $E_0 = 4.0 \times 10^{-9}$ a.u., the dipole moment principal axes components are $\mu^R_a = \mu^S_a = 0.47$ a.u., $\mu^R_b = \mu^S_b = 0.75$ a.u., $\mu^R_c = -\mu^S_c = 0.14$ a.u., and the molecular transition energies are $\varepsilon_2 - \varepsilon_1 = 4.4 \times 10^{-8}$ a.u. and $\varepsilon_3 - \varepsilon_1 = 4.7 \times 10^{-8}$ a.u. The dipole moment components and molecular energies are extracted from a microwave three-wave-mixing model for $R-$ and $S-$1,2-propanediol [7]. Using these parameters, it is true that $|\mu^{R,S}_{i,M';j,M}E_{ij}|/2 \ll \hbar\Omega_{ij}$, so the rotating wave approximation holds. The slow incommensurate

modulation frequencies and laser detuning are taken to be $\omega_1 = \omega_2/\phi = \delta = 1 \times 10^{-11}$ a.u., where we take $\phi = \frac{\sqrt{5}-1}{2}$ as in Ref. [161], satisfying the perturbative condition $\hbar|\delta|$, $\hbar\omega_1$, $\hbar\omega_2 \ll |\mu^{R,S}_{i,M;j,M'} \cdot E_{ij}|/2$. Setting $m = 1.4$, the system is in the topologically nontrivial regime.

To obtain the desired enantioselective TFC, both enantiomers need to be prepared in the lowest adiabatic states in the rotating frame at $t = 0$. Suppose that before fields are turned on ($\mu^{R,S}_{i,M';j,M}\mathscr{E}_{ij}(t) \to 0$ as $t \to -\infty$), the molecules start in the ground state $|1,0\rangle$. Under those circumstances, the eigenstates of Eq. 3.7 are the states $|1,0\rangle, |2,M\rangle, |3,0\rangle$ with eigenenergies $\varepsilon^{R,S}_{L,M,U}(-\infty) = -\delta, 0, \delta$, and the state of each molecule is $|\varepsilon^{R,S}_L(-\infty)\rangle$. If the electric fields are slowly turned on at a rate ω_r that is much smaller than the instantaneous band gaps $|\varepsilon^{R,S}_l(t) - \varepsilon^{R,S}_{l'}(t)|$, both enantiomers are prepared in the lower band, *i.e.* $|\varepsilon^{R,S}_L(0)\rangle$. Note that the modulating frequencies ω_1 and ω_2 must also be much smaller than $|\varepsilon^{R,S}_l(t) - \varepsilon^{R,S}_{l'}(t)|$ at all times. Chirped microwave fields for $t < 0$ satisfy this constraint. The adiabatic protocol we choose is $E_{ij} \to E_{ij}\alpha(t)$ and $\omega_{1,2} \to \omega_{1,2}\beta(t)$, where the ramp-up functions slowly vary at the rate $\omega_r = 2 \times 10^{-13}$ a.u. (see Fig. 3.4),

$$\alpha(t) = \begin{cases} 0 & t < -\frac{2\pi}{\omega_r}, \\ \frac{1-\cos\omega_r t}{2} & -\frac{2\pi}{\omega_r} < t < -\frac{\pi}{\omega_r}, \\ 1 & -\frac{\pi}{\omega_r} < t, \end{cases} \tag{3.17a}$$

$$\beta(t) = \begin{cases} 0 & t < -\frac{\pi}{\omega_r}, \\ \frac{1+\cos\omega_r t}{2} & -\frac{\pi}{\omega_r} < t < 0, \\ 1 & 0 < t. \end{cases} \tag{3.17b}$$

After a sufficiently long time (we choose $t^* = 2000 \times 2\pi/\omega_2$), the frequency-resolved time-averaged power spectrum $P_{av}(\Omega)$ lost by the fields is numerically calculated considering only $t \geq 0$. This quantity is indeed enantioselective, and using Eqs. 3.16a and 3.16b, each enantiomer Chern number for the lower adiabatic state $C^R_L = -2 = -C^S_L$ is extracted, revealing

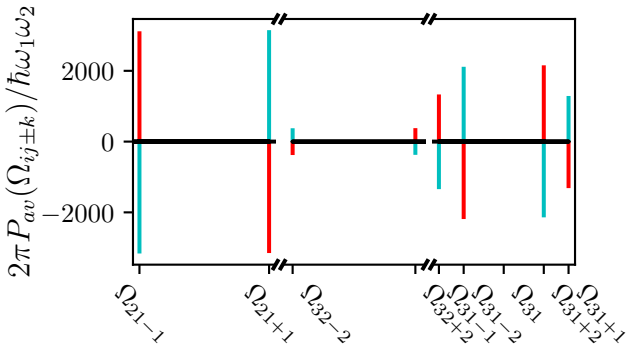

Figure 3.5. *Enantioselective TFC*: Plotted is the difference power spectrum for the driving electric field when coupled to a single $R-$ (red) and $S-$ (cyan) 1,2-propanediol enantiomers. In terms of intensity, assuming the laser beam waist area is ~ 1 cm^2, the change observed is $\sim 10^{-15}\,\mathrm{W\cdot m^{-2}}$ per molecule. This spectrum is enantioselective, and using Eqs. 3.16a and 3.16b, we can see that the frequency conversion in the rotating frame is topological, $\frac{2\pi}{\hbar\omega_1\omega_2}\mathscr{P}^R_{2\to1} = -\frac{2\pi}{\hbar\omega_1\omega_2}\mathscr{P}^S_{1\to2} = -2$.

the topological nature of this nonlinear optical phenomenon (Fig. 3.5).

3.3.3 Detecting enantiomeric excess

For an ensemble containing N_R $R-$molecules and N_S $S-$molecules, which are all prepared in the ground state $|1,0\rangle$, the expected pumping rate is

$$\mathscr{P}_{2\to1} = \frac{\hbar\omega_1\omega_2 C_L^R}{2\pi}(N_R - N_S). \tag{3.18}$$

which is zero for a racemic mixture, but otherwise, reveals the EE $|N_R - N_S|$ and chirality $\mathrm{sgn}(N_R - N_S)$. Notice that in line with other nonlinear chiroptical signals that depend on electric but not magnetic dipole contributions [127], Eq. 3.18 contains no background achiral signal, unlike traditional circular dichroism, where both enantiomers have the same electric dipole and magnetic dipole absorption strengths for circularly polarized light [169].

Let us briefly discuss the limits of enantioselective TFC. First, the linewidths of microwave transitions are on the order of 10-100 kHz [170], which are smaller than the adiabatic state preparation gap $\delta \approx 1\,\mathrm{MHz}$, as well as the light-matter interactions $|\mu_{ij}E_{ij}|/\hbar \approx 10\,\mathrm{MHz}$

inducing the topological gap, or even the smallest difference in energies in the power spectrum (see, Fig. 3.5, $\Omega_{31\pm1} - \Omega_{31\pm2} \approx 1\,\mathrm{MHz}$). Thus, the described protocol should be resilient to the finite linewidths of these transitions. Second, another source of imperfections stems from laser shot noise. Assuming that the laser beam waist area is $\sim 1\,\mathrm{cm}^2$ and considering the field strength above, the shot noise for a time interval t^* is $\sqrt{N} \sim 10^9$ (where N is the expected number of photons produced by the field, see B.6). From the power spectrum (Fig. 3.5), we find that for the same time interval, that the minimal magnitude of the change in the photon number due to the TFC is $\min\left(\left|\frac{P_{av}(\Omega_{ij\pm1,2})t^*}{\hbar\Omega_{ij\pm1,2}}\right|\right) \approx 100 \times |N_R - N_S|$. Therefore, as long as the magnitude of the enantiomer excess $|N_R - N_S|$ is much larger than $\sim 10^7$ molecules, the signal should be detectable above the shot noise. In terms of percentage of the total molecule count $N_R + N_S$, the lower end of the EE detection limit for 1 mL of a 1 μM solution is $10^{-6}\%$. We conclude with a few comments on the observability of our predictions. First, this study has assumed the ideal limit that the molecules are at 0 K. Under typical experimental conditions for microwave-three wave mixing at 7 K [7] all three rotational energy levels used in our model are substantially thermally occupied. In this scenario, enantioselective frequency conversion still survives; however, the integer Chern number will be replaced by a thermal average of the Chern numbers C_L^R, C_M^R, C_U^R. Second, the excited-state thermal populations can be bypassed by working in a different energy range, such as the UV-visible one involving electronic transitions and the infrared one involving vibrations [171, 172]; the price to pay in the first case is the complication introduced by electron-vibration coupling. These complications will be addressed in future works.

3.4 Conclusion

In summary, we have presented an enantioselective TFC setup for an ensemble of chiral molecules. Owing to the dependence of the topological invariant on the sign of the KS product (Eq. 3.15), which differs by a phase of π for the two enantiomers, the quantized time-averaged energy-pumping rate is of opposite sign for the $R-$ and $S-$ molecules, just like

how the transverse conductivity is of opposite sign for up and down spins in the QSHE. We show that the computed signal is non-zero for any sample with EE and vanishes for a racemic mixture. An intriguing consequence of Eq. 3.14 is that as long as the timescale separations required by the model are fulfilled, the chemical identity of the probed molecules (*e.g.*, through the strengths of the transition dipole moments) in the rotating frame is erased by the signal, leading to a universal nonlinear optical response which acknowledges the enantiomeric excess only. This characteristic is reminiscent of the very accurate determination of the quantum of conductance with a wide range of QHE systems. Thus, from a metrological standpoint, the generality of the enantioselective TFC can be exploited to accurately measure EE by running a linear fit of the pumping rate $\mathscr{P}_{2\to1}$ for a series of experiments where ω_1 (or ω_2) is varied. Furthermore, if one is only concerned with |EE|, a practical asset of the presented methodology is that there is no need to calibrate the signal with an enantiopure sample beforehand. We believe that the removal of calibration counterbalances the complexity of the experimental setup proposed in this Letter.

While concepts of topology have been very productive in the exploration of new condensed matter physics phenomena, most of them are restricted to periodic solids (see Ref. [173, 66] for a few molecular exceptions). TFC [161, 158] is a powerful tool that opens doors to the application of those concepts to 0D systems such as finite molecular and non-periodic nanoscale systems. In particular, this work reveals that laser-dressed chiral molecules support SPTPs that are not adiabatically connected to their non-laser-dressed counterparts. It also provides a fruitful playground to explore further conceptual connections between topological physics and molecular chirality [162, 174]

Chapter 3, in full, is adapted from the material as it appears in "Enantioselective Topological Frequency Conversion," by K. Schwennicke and J. Yuen-Zhou, *J. Phys. Chem. Lett.* **13.10**, 2434-2441 (2022) [67]. The dissertation author was the primary investigator and author of this paper.

Chapter 4

Extracting accurate light-matter coupling from disordered polaritons

4.1 Introduction

In the realm of molecular polaritons, the phenomenon of vacuum Rabi splitting (VRS) stands as an established metric for gauging the strength of collective light-matter coupling. Traditionally, this interaction is classified into several regimes: weak, strong, ultrastrong, and deep-strong [175]. In particular, molecular polaritons are often observed in the realm of strong coupling, with a wide range of potential applications such as catalysis [25, 20, 21, 24], exciton transport [33, 34, 35, 36, 37, 176], and Bose-Einstein condensation [45, 47, 48]. While reaching the ultrastrong coupling regime remains experimentally challenging, there are a number of experiments that have pushed the limits of molecular systems into this intriguing regime [177, 178, 179, 180].

In the idealized scenario of N identical molecules strongly coupled to a single photonic mode, the magnitude of VRS scales linearly with $\sqrt{N}$ [181, 182]. However, the inherent complexity of molecular ensembles introduces a compelling challenge, as molecular disorder becomes an inescapable feature. Molecular disorder exerts a profound influence on various aspects of polariton physics, including transport [183, 184, 185, 186, 34, 37, 35, 187], photoconductivity [188], photoreactivity [189], and vibropolaritonic chemistry [23]. In the solid-state physics community, using polaritons to reduce the linewidth of quantum emitters has potential

applications in the storage of quantum information [190, 191]. Surprisingly, even though the effects of disorder were theoretically studied early on [192, 193, 194, 195], the effects of disorder on VRS splitting are still a debate within the community. Early explorations by Houdré et al. [194] suggested that disorder (or inhomogeneous broadening) should have no impact on the size of the splitting. However, these conclusions have been contested in recent investigations [196, 35, 197, 198, 199, 200, 201] which note that disorder can both enhance and suppress the VRS.

In this article, we revisit the problem of VRS and disorder, embarking on a comprehensive study of linear absorption A, transmission T, and reflection R properties of molecular polaritons, considering various distributions and magnitudes of disorder. Our aim is not only to elucidate the intricate interplay between molecular disorder and VRS, but also to provide a robust method for accurately extracting light-matter coupling parameters. Our findings align with recent reports, demonstrating that VRS tends to increase with disorder, reaches a saturation point, and eventually decreases to zero for a wide range of disorder distributions. Note that A, T, R do not in general give the same value of VRS [193]. Hence, while some of the results are already known in the literature, we deem it valuable to collect all the results in a single study. Significantly for experiments, we unveil what seems to be a ubiquitous scenario: the presence of substantial disorder can dramatically enhance the VRS leading to an *apparent* onset of the ultrastrong coupling regime, despite the underlying collective light-matter coupling firmly residing within the strong coupling regime. Moreover, we introduce a novel sum rule that proves instrumental in extracting precise values of collective light-matter coupling, particularly when both absorption and transmission can be measured in the experimental setup. Crucially, this sum rule demonstrates generality across all types of disorder. In the case of a rectangular distribution (which was briefly discussed in Ref. [197]), we observe the emergence of two narrow polariton peaks in the spectra, reminiscent of the pronounced spectral narrowing witnessed in the context of surface lattice resonances [202] and other phenomena associated with Wood anomalies [203, 204, 205, 206, 207].

4.2 Theory

4.2.1 Model

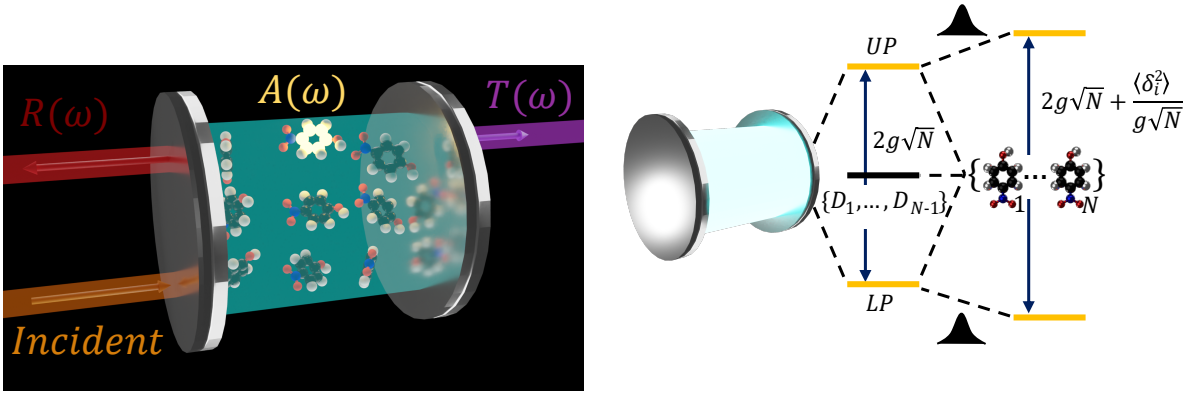

(a) **(b)**

Figure 4.1. *Disorder effects on linear polariton spectra*: (a) Linear spectroscopy of molecular polaritons as absorption $A(\omega)$, transmission $T(\omega)$, and reflection $R(\omega)$ (b) For weak disorder, a perturbative approach to understand the role of disorder is useful. The zeroth-order Hamiltonian can be taken to be the disorderless system, comprising of the photon mode interacting with the N degenerate molecules to form the upper (UP) and lower (LP) polaritons, alongside $N-1$ dark states ($\{D_1,...,D_{N-1}\}$). The VRS at resonance in this case happens to be $2g\sqrt{N}$, where g is the single molecule light-matter coupling. The molecular disorder then perturbatively couples the polaritons to the manifold of dark states, inducing level repulsion between the polaritons, as discussed in Refs. [196, 199], and [200], thus increasing the VRS. This repulsion depends on the variance of the disorder distribution ($\langle\delta_i^2\rangle$, where $\delta_i = \omega_i - \omega_0$ and ω_0 represents the center of the distribution). Given the perturbative character of this analysis, it does not apply to strong disorder.

For concreteness, we consider N two-level systems coupled to a single photon mode [in the rotating wave approximation (RWA), Tavis–Cummings model [181]]:

$$H = \hbar\omega_{ph}a^\dagger a + \sum_{i=1}^{N}\hbar\omega_{ex,i}\sigma_i^\dagger\sigma_i - \hbar\lambda\left(\sum_{i=1}^{N}\mu_i a\sigma_i^\dagger + \text{h.c.}\right), \tag{4.1}$$

where ω_{ph} and a are the photon frequency and annihilation operator, $\omega_{ex,i}$ and $\sigma_i = |g_i\rangle\langle e_i|$ are the frequency and annihilation operator for the $i-$th two-level system, μ_i is the amplitude of the $i-$th transition dipole, and $\hbar\lambda = \sqrt{\frac{\hbar\omega_{ph}}{2\varepsilon_0\mathcal{V}_{ph}}}$ is the vacuum field amplitude where ε_0 is the

Table 4.1. Real and imaginary parts of the molecular susceptibility

	Susceptibility		
Real or Imaginary	Gaussian[a]	Lorentzian	Rectangle
$\frac{\omega_{ph}}{2}\chi'(\omega)$	$-\frac{g^2N\sqrt{2}}{\sigma}F(\frac{\omega-\omega_0}{\sqrt{2}\sigma})$	$-g^2N\frac{(\omega-\omega_0)}{(\omega-\omega_0)^2+(\sigma/2)^2}$	$-\frac{g^2N}{\sigma}\ln\lvert\frac{\omega-\omega_0+\sigma/2}{\omega-\omega_0-\sigma/2}\rvert$
$\frac{\omega_{ph}}{2}\chi''(\omega)$	$\frac{g^2N}{\sigma}\sqrt{\frac{\pi}{2}}\exp[-\frac{1}{2}(\frac{\omega-\omega_0}{\sigma})^2]$	$g^2N\frac{\sigma/2}{(\omega-\omega_0)^2+(\sigma/2)^2}$	$\frac{g^2N\pi}{\sigma}\mathrm{rec}[2(\omega-\omega_0)/\sigma]$

[a]Here $F(y)=\exp[-y^2]\int_0^y dte^{t^2}$ is the Dawson function.

vacuum permittivity and $\mathscr{V}_{ph}$ is the mode volume. In the thermodynamic limit ($N\to\infty$), the linear absorption, transmission, and reflection spectra are given by (see Refs. [208] and [209])

$$A(\omega)=\frac{\kappa_L\omega_{ph}\chi''(\omega)}{|\omega-\omega_{ph}+i\frac{\kappa}{2}+\frac{\omega_{ph}}{2}\Big[\chi'(\omega)+i\chi''(\omega)\Big]|^2}, \tag{4.2}$$

$$T(\omega)=\frac{\kappa_L\kappa_R}{|\omega-\omega_{ph}+i\frac{\kappa}{2}+\frac{\omega_{ph}}{2}\Big[\chi'(\omega)+i\chi''(\omega)\Big]|^2}, \tag{4.3}$$

$$R(\omega)=1-A(\omega)-T(\omega). \tag{4.4}$$

Note, for simplicity we are considering the case where the volume of the molecular sample is equal to the cavity mode volume (*i.e.* $\mathscr{V}_{mol}=\mathscr{V}_{ph}$). Here $\kappa=\kappa_L+\kappa_R$ is the total cavity decay rate, and the respective decay rates into the left and right photon continua are denoted by κ_L and κ_R. The linear molecular susceptibility $\chi(\omega)$ is given by

$$\chi(\omega)=-\lim_{\gamma\to0^+}\frac{1}{\hbar\varepsilon_0\mathscr{V}_{mol}}\sum_i^N\tanh\left(\frac{\hbar\omega_{ex,i}}{2k_BT}\right)\frac{|\mu_i|^2}{\omega-\omega_{ex,i}+i\frac{\gamma}{2}}. \tag{4.5}$$

Considering the case when $\hbar\omega_{ex,i}\gg k_BT$ and assuming that all N two-level systems have the same transition-dipole amplitude μ, the molecular susceptibility, multiplied by a factor $\frac{\omega_{ph}}{2}$,

becomes

$$\frac{\omega_{ph}}{2}\chi(\omega) = -\lim_{\gamma\to 0^+} g^2 N \int d\omega_{ex} \frac{p(\omega_{ex})}{\omega - \omega_{ex} + i\frac{\gamma}{2}}$$
$$= \frac{\omega_{ph}}{2}\Big[\chi'(\omega) + i\chi''(\omega)\Big], \tag{4.6}$$

where $g^2 = |\lambda\mu|^2$ is the square of the single molecule light-matter coupling, $p(\omega_{ex})$ is the probability distribution of excitation frequencies, and the real and imaginary parts of the molecular susceptibility, multiplied by a factor $\frac{\omega_{ph}}{2}$, are $\frac{\omega_{ph}}{2}\chi'(\omega) = -g^2 N\mathscr{P}\int d\omega_{ex}\frac{p(\omega_{ex})}{\omega-\omega_{ex}}$, where $\mathscr{P}$ is the Cauchy principal value, and $\frac{\omega_{ph}}{2}\chi''(\omega) = g^2 N\pi p(\omega)$. It is insightful to note that the simple dependence of the polariton absorption spectrum on the bare molecular linear susceptibility is similar to the simple dependence of the spectroscopic response of molecular aggregates, under the coherent potential approximation, on the response of the isolated monomeric units [210].

To explore the effects of $p(\omega_{ex})$, we consider Lorentzian,

$$p(\omega_{ex}) = \frac{1}{\pi}\frac{\sigma/2}{(\omega_{ex}-\omega_0)^2 + (\sigma/2)^2}, \tag{4.7}$$

Gaussian,

$$p(\omega_{ex}) = \frac{1}{\sqrt{2\pi}\sigma} e^{-\frac{1}{2}(\frac{\omega_{ex}-\omega_0}{\sigma})^2}, \tag{4.8}$$

and rectangular

$$p(\omega_{ex}) = \frac{1}{\sigma}\mathrm{rec}[2(\omega_{ex}-\omega_0)/\sigma], \tag{4.9}$$

$$\mathrm{rec}[y] = \begin{cases} 1, & |y| \le 1 \\ 0, & |y| > 1 \end{cases} \tag{4.10}$$

disorder. Table 4.1 lists the analytical expressions of $\chi'(\omega)$ and $\chi''(\omega)$ for the three different

distributions.

4.3 Results

4.3.1 Lorentzian disorder

For Lorentzian disorder, the real and imaginary parts of the susceptibility, multiplied by a factor $\frac{\omega_{ph}}{2}$, are

$$\frac{\omega_{ph}}{2}\chi'(\omega) = -g^2 N \frac{(\omega-\omega_0)}{(\omega-\omega_0)^2+(\sigma/2)^2}, \tag{4.11}$$

$$\frac{\omega_{ph}}{2}\chi''(\omega) = g^2 N \frac{\sigma/2}{(\omega-\omega_0)^2+(\sigma/2)^2}. \tag{4.12}$$

From Eqs. 4.2 and 4.3, the absorption, transmission, and reflection spectra are given by

$$A(\omega) = \frac{\kappa_L \sigma g^2 N}{|(\omega-\omega_{ph}+i\frac{\kappa}{2})(\omega-\omega_0+i\frac{\sigma}{2})-g^2N|^2}, \tag{4.13}$$

$$T(\omega) = \frac{\kappa_L \kappa_R[(\omega-\omega_0)^2+(\sigma/2)^2]}{|(\omega-\omega_{ph}+i\frac{\kappa}{2})(\omega-\omega_0+i\frac{\sigma}{2})-g^2N|^2}, \tag{4.14}$$

$$R(\omega) = 1 - \frac{\kappa_L\left\{\kappa_R[(\omega-\omega_0)^2+(\sigma/2)^2]+\sigma g^2 N\right\}}{|(\omega-\omega_{ph}+i\frac{\kappa}{2})(\omega-\omega_0+i\frac{\sigma}{2})-g^2N|^2}. \tag{4.15}$$

Figure 4.2 presents the numerically calculated spectra.

To find the extrema of each spectrum, we solve for $\frac{d}{d\omega}T(\omega)=0$, $\frac{d}{d\omega}A(\omega)=0$, and $\frac{d}{d\omega}R(\omega)=0$ separately. Lorentzian disorder affords exact analytical expressions for all regimes of σ. In the case where the photon mode is resonant with the center of the Lorentzian distribution, *i.e.*, $\omega_{ph}=\omega_0$, we find that the upper (ω_+^A) and lower (ω_-^A) polariton peaks in the absorption are located at the frequencies

$$\omega_\pm^A = \omega_0 \pm \Im\left[\sqrt{\frac{1}{8}(\sigma^2+\kappa^2)-g^2N}\right]. \tag{4.16}$$

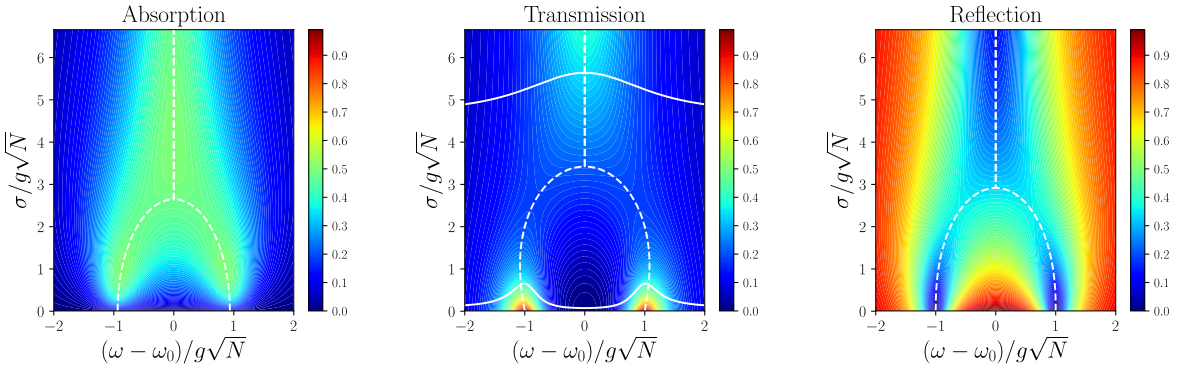

Figure 4.2. *Numerically calculated spectra for a Lorentzian distribution*: (a) absorption, (b) transmission, and (c) reflection spectra for a Lorentzian distribution of excitation energies $p(\omega_{ex})$ centered at $\omega_{ex} = \omega_0$; $\omega_{ph} = \omega_0$ and $\kappa_L = \kappa_R = \frac{1}{2}g\sqrt{N}$. The white dashed lines indicate our analytical results for the polariton frequencies, showing strong agreement with the calculated spectra over all magnitudes of disorder. As done in Ref. [196], the white solid lines in (B) represent individual spectra for weak and strong disorder systems, highlighting the transition from two distinct peaks to a broad central peak as disorder increases.

Similarly, the upper and lower polariton peaks in the transmission spectrum are located at

$$\omega_{\pm}^{T} = \omega_0 \pm \Im\left[\sqrt{\frac{\sigma^2}{4} - g^2N\sqrt{1+\frac{\sigma(\kappa+\sigma)}{2g^2N}}}\right], \tag{4.17}$$

and the peaks in the reflection spectrum are at

$$\omega_{\pm}^{R} = \omega_0 \pm \Im\left[\left(\frac{\sigma^2}{4} + \frac{\sigma g^2 N}{\kappa_R} - g^2N\sqrt{\frac{\sigma(\kappa+\sigma)(\sigma-\kappa+2\kappa_R)}{4\kappa_R g^2 N} + \left(1+\frac{\sigma}{\kappa_R}\right)^2}\right)^{1/2}\right]. \tag{4.18}$$

With prior information on the molecular disorder (σ) and cavity linewidth (κ), one can use the above equations to extract the correct value for the collective coupling $g\sqrt{N}$ from experimentally obtained spectra. For the transmission spectra, we observe similar behavior to that was shown in Refs. [196, 197, 198, 199, 200] for Gaussian disorder: the VRS initially increases with

Table 4.2. Vacuum Rabi splitting trends with disorder

	Gaussian		Lorentzian		Rectangle	
Optical Signal	$\sigma < g\sqrt{N}$	$\sigma > g\sqrt{N}$	$\sigma < g\sqrt{N}$	$\sigma > g\sqrt{N}$	$\sigma < g\sqrt{N}$	$\sigma > g\sqrt{N}$
$A(\omega)$	increases	decreases	decreases	decreases	increases	decreases; narrow side bands
$T(\omega)$	increases	decreases	increases	decreases	increases	decreases; narrow side bands
$R(\omega)$	increases	decreases	increases or decreases[a]	decreases	increases	decreases; narrow side bands

[a]For the Lorenzian, the VRS in the reflection spectrum increases if $\kappa_L^2/\kappa_R^2 < 1$ and decreases if $\kappa_L^2/\kappa_R^2 > 1$ (See Table 4.3)

increasing disorder; as disorder increases further, the VRS saturates, and then decreases to zero. It is interesting that this trend is not observed for absorption, as VRS only *decreases* with disorder. Table 4.2 summarizes the intricate behavior of VRS across spectra for different disorder distributions. Qualitatively, the increase of VRS with weak disorder is a manifestation of level repulsion (see Figure 4.1b). Additionally, the collapse of the VRS and the transition from two peaks to a single central peak can be related to an exceptional point pertaining to the complex-valued pole of the polariton transmission spectrum [35]. It should be noted that Eqs. 4.13-4.14 are the same as those presented in Ref. [193]. Furthermore, the expressions for $\kappa = 0$, Eq. 4.16 looks similar to the analytical expressions derived by Refs. [35, 197] and [201], but the decrease in VRS for weak disorder differs by a factor of a half compared to our result. This is due to the fact that the real parts of the poles for Eqs. 4.16-4.18 do not correspond to the true extrema along the real-value frequency axis.

4.3.2 Gaussian and rectangular disorder

For Gaussian and Rectangular disorder, we can still extract semi-analytical results when $\sigma \ll g\sqrt{N}$ (weak disorder) and $|\omega - \omega_0| \approx g\sqrt{N}$ (about the polariton peaks). For the Gaussian distribution, we employ the asymptotic expansion of the Dawson function [211], similar to Ref. [197], up to $O[(\frac{\sigma}{\omega-\omega_0})^3]$ to obtain an approximate expression for the real part of the susceptibility, multiplied by a factor $\frac{\omega_{ph}}{2}$,

$$\frac{\omega_{ph}}{2}\chi'(\omega) \approx -g^2 N\left[\frac{1}{\omega-\omega_0} + \frac{\sigma^2}{(\omega-\omega_0)^3}\right]. \tag{4.19}$$

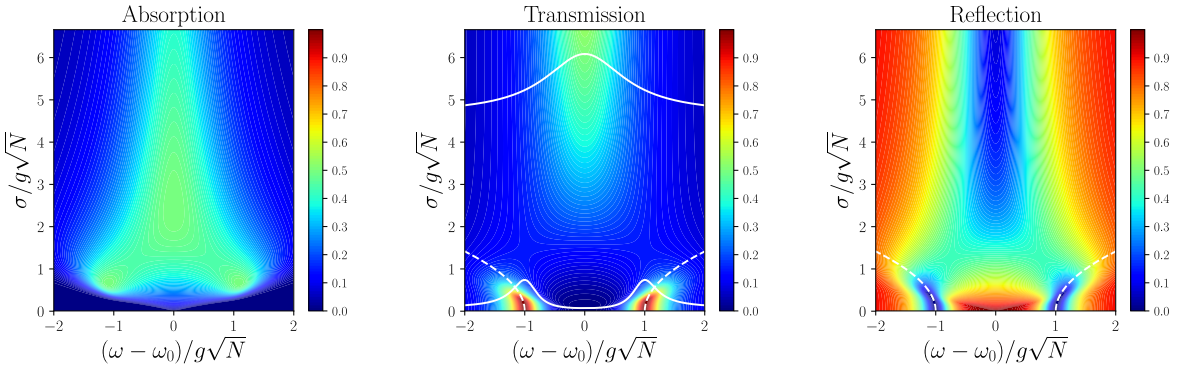

Figure 4.3. *Numerically calculated spectra for a Gaussian distribution*: (a) absorption, (b) transmission, and (c) reflection spectra for a Gaussian distribution of excitation energies $p(\omega_{ex})$ centered at $\omega_{ex} = \omega_0$; $\omega_{ph} = \omega_0$ and $\kappa_L = \kappa_R = \frac{1}{2}g\sqrt{N}$. The white dashed lines indicate our analytical results for the polariton frequencies, showing strong agreement with the calculated spectra for weak disorder. The white solid lines in (b) represent individual spectra for weak and strong disorder systems, highlighting the transition from two distinct peaks to a broad central peak as disorder increases.

Meanwhile, for the rectangular distribution, we get,

$$\frac{\omega_{ph}}{2}\chi'(\omega) \approx -g^2 N\left[\frac{1}{\omega-\omega_0}+\frac{\sigma^2}{12(\omega-\omega_0)^3}\right]. \tag{4.20}$$

Note that for both distributions $\chi''(\omega) \approx 0$ at the polaritonic windows, so no VRS is predicted in the absorption spectrum for both Gaussian and rectangular distributions for low disorder. The lack of VRS in the absorption spectrum in the case of low disorder for these distributions is due to the minimal overlap between the molecular absorption spectrum and the polariton transmission, since the tails of the Gaussian die quickly away from ω_0, while the rectangular distribution has no tails. Contrast this observation with the analogous one for the Lorentzian distribution, which does present VRS in its absorption spectrum owing to the long tails of the Lorentzian. As disorder increases, the tails of the Gaussian and rectangular distributions overlap more with the polariton transmission peaks, and VRS begins to appear in the polariton absorption spectrum. However, as disorder becomes increasingly stronger, the VRS collapses, resulting in a broad central peak (see Figs. 4.3A and 4.4A). Understanding the difference in overlap of the Lorenzian

and Gaussian tails with the polariton transmission peaks can be used to engineer systems with higher polariton quality factors; for example, Ref. [212] proposes using an applied magnetic field to convert a Lorentzian disorder distribution into a Gaussian one in order to remove the influence of the Lorentzian tails.

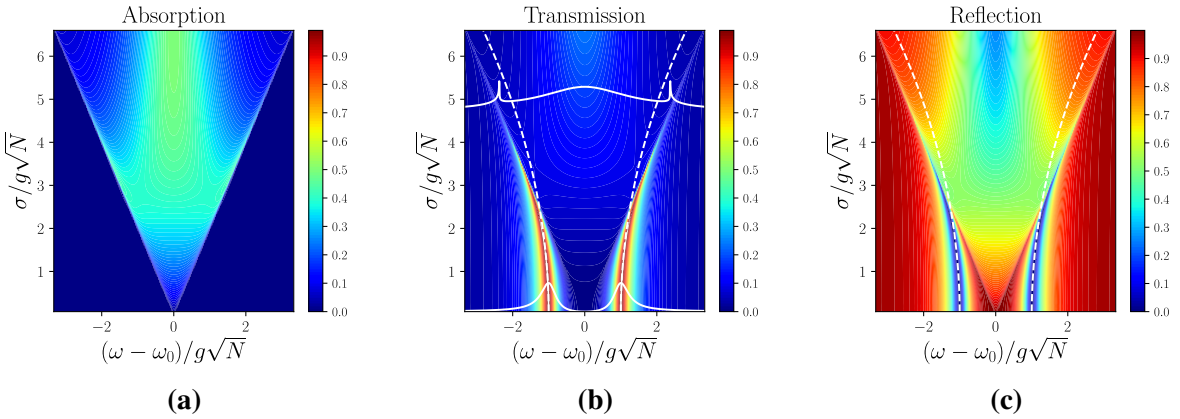

Figure 4.4. *Numerically calculated spectra for a rectangular distribution*: (a) absorption, (b) transmission, and (c) reflection spectra for a rectangular distribution of excitation energies $p(\omega_{ex})$ centered at $\omega_{ex} = \omega_0$; $\omega_{ph} = \omega_0$ and $\kappa_L = \kappa_R = \frac{1}{2}g\sqrt{N}$. The white dashed lines indicate our analytical results for the polariton frequencies, showing strong agreement with the calculated spectra for weak disorder. The white solid lines in (B) represent individual spectra for weak and strong disorder systems, highlighting the transition from two distinct peaks to a broad central peak as disorder increases. Remarkably, for large disorder, two peaks that are narrower than the line width of the cavity and molecular disorder emerge on either side of the broad central peak.

Using these approximations, we find that for $\omega_{ph} = \omega_0$, the transmission and reflection spectra for Gaussian distribution are approximately

$$T(\omega) \approx \frac{\kappa_L \kappa_R g^6 N^3}{|(\omega-\omega_0)^4 - g^2N(\omega-\omega_0)^2 - g^2N\sigma^2 + ig^3N^{\frac{3}{2}}\frac{\kappa}{2}|^2}, \tag{4.21}$$

$$R(\omega) \approx 1 - T(\omega), \tag{4.22}$$

with the polariton frequencies for both spectra approximately located at

$$\omega_\pm = \omega_0 \pm \sqrt{\frac{1}{2}g^2N + \frac{1}{2}\sqrt{g^4N^2 + 4g^2N\sigma^2}}. \tag{4.23}$$

Similarly, we find that the transmission and reflection spectra for the rectangular distribution are approximately

$$T(\omega) \approx \frac{\kappa_L \kappa_R g^6 N^3}{|(\omega-\omega_0)^3 - g^2 N(\omega-\omega_0) - \frac{g^2 N \sigma^2}{12} + i g^3 N^{\frac{3}{2}} \frac{\kappa}{2}|^2}, \tag{4.24}$$

$$R(\omega) \approx 1 - T(\omega). \tag{4.25}$$

In this case the polariton frequencies are approximately located at

$$\omega_\pm = \omega_0 \pm \sqrt{\frac{1}{2} g^2 N + \frac{1}{2}\sqrt{g^4 N^2 + \frac{\sigma^2 g^2 N}{3}}}, \tag{4.26}$$

which is similar to Eq. 4.23.

Figure 4.3 shows the numerically calculated spectra for Gaussian disorder. The trend in VRS in the transmission and reflection spectra as a function of σ is qualitatively the same as that for the Lorentzian: the VRS initially increases for $\sigma < g\sqrt{N}$, and then decreases to zero for $\sigma > g\sqrt{N}$ (see Table 2). Additionally, the initial increase in VRS for the Gaussian and rectangular distributions, for weak disorder, can be understood through the mechanism of level repulsion between the polariton states and the dark states, which are coupled by the molecular disorder. Eq. 4.23 is in good agreement with the numerical results for $\sigma \ll g\sqrt{N}$, and upon Taylor expanding around $\sigma = 0$ to second order, reduces to the analytical results of Refs. [197] and [200]. The analytical results of Refs. [196] and [199] qualitatively capture the behavior of the transmission spectrum; however, quantitatively they fit better with the Lorentzian disorder. The transformation of Gaussian into Lorentzian disorder in these references appears to be due to the usage of the Markovian approximation. Figure 4.3 also highlights the dangers for taking VRS at face value. We observe that the largest VRS in the transmission and reflection spectra is approximately $1.5 \times 2g\sqrt{N}$. This implies that one must be careful using VRS to determine the strength of the collective light-matter coupling. For example, if $\mathrm{VRS}/2\omega_0 \approx 0.1$ one may

mistakenly claim to be in the ultrastrong coupling regime, which is typically defined as the region where $g\sqrt{N}/\omega_0 \gtrsim 0.1$ [213, 214], while in reality the collective light-matter coupling $g\sqrt{N}/\omega_0 \approx 0.07$ is still within the strong coupling regime.

Figure 4.4 displays the numerically calculated spectra for the rectangular disorder. Such a scenario was briefly considered in Ref [197]; here, we provide further analysis. At low disorder, the rectangular distribution exhibits similar behavior to the Gaussian distribution, as predicted by Eq. 4.26. As disorder increases, a broad central peak forms, consistent with both the Lorentzian and Gaussian distributions. Intriguingly, as disorder increases, two sharp sidebands for the polaritons also emerge, each narrower than the cavity linewidth and the width of the rectangular distribution, respectively. This is reminiscent of the pronounced spectral narrowing witnessed in plasmonic surface lattice resonances [202]. The unique characteristics of the rectangular disorder, including singularities in its real part of the susceptibility $\chi'(\omega)$ near these polariton peaks (see Table 4.1), are responsible for this phenomenon. The reduced linewidth of these peaks indicates a higher degree of coherence lifetime within the system, even in the presence of significant energetic disorder. Consequently, this observation presents a promising avenue for applications in molecular polariton systems requiring prolonged coherences between the cavity and molecules. In a realistic experiment, this phenomenon will only occur if the underlying members of the disorder distribution have a small Lorentzian homogeneous linewidth (which has not been treated in this work); a large such linewidth will smoothen the singularity and reduce the problem to the Lorentzian case.

For completeness, we study the effects of rounding the discontinuous edge of the rectangular distribution. Consider the continuous distribution

$$p_m(\omega_{ex}) = \frac{1}{\sigma} R_m[2(\omega_{ex} - \omega_0)/\sigma], \tag{4.27}$$

where

$$R_m[y] = \frac{1}{y^{2m}+1} \tag{4.28}$$

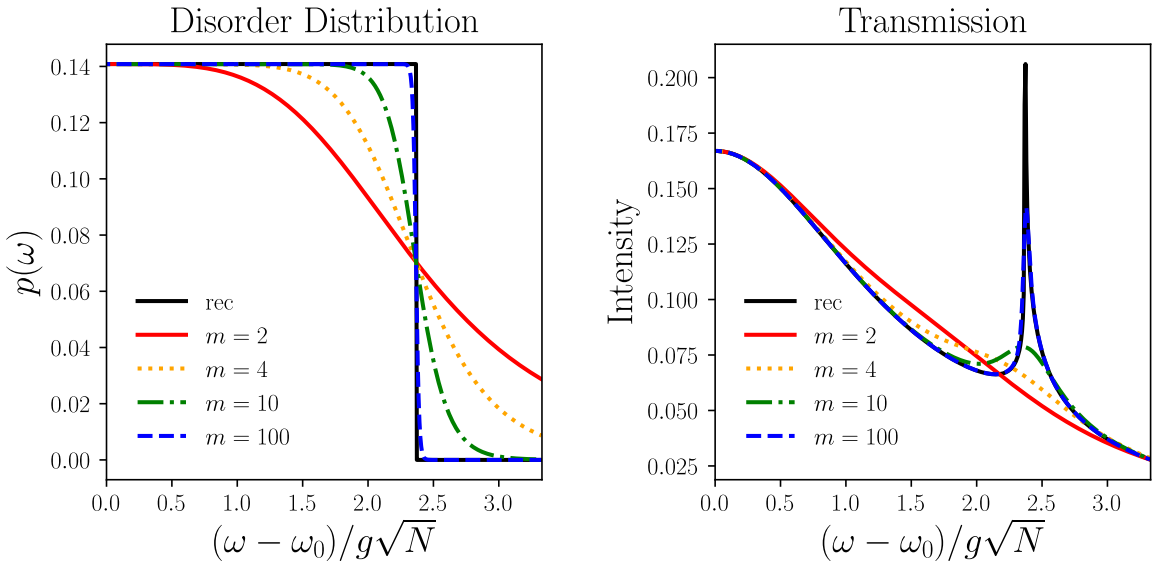

Figure 4.5. *Discontinuous versus continuous disorder distribution edge*: (a) Comparing the discontinuous rectangular (rec) distribution with the continuous function R_m for different values of m. As m increases, the edge becomes sharper, such that the continuous distribution begins to mimic the rectangular one. (b) Comparing the resulting polariton transmission spectra for large disorder where the rectangular distribution has sharp sidebands. For $m = 2$, only a broad central peak is observed, but as m increases the sidebands emerge and become sharper.

and m is a positive integer. In the limit $m \to \infty$, $R_m[y]$ mimics the rectangular function rec$[y]$ (see Eq. 4.9). Figure 4.5 shows that for small values of m, where the "edge" of the distribution is relatively smooth, only a single broad central peak is observed. As m increases, the two sidebands emerge and become sharper, as does the edge of the distribution. These results highlight that the survival of these sidebands heavily depends on the steep rise at the edge of the distribution, though this edge need not be perfect due to the fact that these spectral features are observed for finite m where the corners of the distribution are rounded. A candidate system would be a uniform distribution of quantum emitter frequencies, possibly engineered with quantum dots that have a narrow homogeneous linewidth.

Table 4.3. Vacuum Rabi splitting expressions for when $\sigma \ll g\sqrt{N}$

Optical Signal	Vacuum Rabi Splitting		
	Gaussian	Lorentzian[a]	Rectangle
$A(\omega)$	0	$2g\sqrt{N} - \frac{\sigma^2}{8\sqrt{g^2N - \frac{\kappa^2}{8}}}$	0
$T(\omega)$	$2\sqrt{\frac{1}{2}g^2N + \frac{1}{2}\sqrt{g^4N^2 + 4g^2N\sigma^2}}$	$2g\sqrt{N} + \frac{\kappa\sigma}{4g\sqrt{N}}$	$2\sqrt{\frac{1}{2}g^2N + \frac{1}{2}\sqrt{g^4N^2 + \frac{\sigma^2 g^2 N}{3}}}$
$R(\omega)$	$2\sqrt{\frac{1}{2}g^2N + \frac{1}{2}\sqrt{g^4N^2 + 4g^2N\sigma^2}}$	$2g\sqrt{N} - \frac{(\frac{\kappa_L^2}{\kappa_R} - \kappa_R)\sigma}{8g\sqrt{N}}$	$2\sqrt{\frac{1}{2}g^2N + \frac{1}{2}\sqrt{g^4N^2 + \frac{\sigma^2 g^2 N}{3}}}$

[a]For larger values of σ, Eqs. 4.16-4.18 should be used to extract the correct value for $g\sqrt{N}$.

4.3.3 Sum rule

From our extensive study of disorder effects on the polariton linear spectrum, it is evident from the three disorder distributions studied in this work, that disorder significantly impacts the value of VRS, seemingly posing a challenge in extracting the precise value of the collective light-matter coupling. However, a simple sum rule can be utilized when both the absorption and transmission polariton spectra are accessible. By integrating the ratio of these two signals (I), which is proportional to the imaginary part of the linear molecular susceptibility multiplied by a factor of $\frac{\omega_{ph}}{2}$ [*i.e.* $\frac{\omega_{ph}}{2}\chi''(\omega) = g^2 N\pi p(\omega)$], a robust method for determining the collective light-matter coupling is revealed (see Eqs. 4.2 and 4.3):

$$I = \int d\omega \frac{A(\omega)}{T(\omega)} = \frac{2\pi}{\kappa_R} g^2 N. \tag{4.29}$$

Importantly, this expression is general for any form and strength of disorder. The final form of this sum rule is similar to the well-established sum rule for the bare molecular system [215]. Note that Eq. 4.29 is presented in the low-temperature limit. For finite temperature effects, see C. Therefore, experimental setups that enable the measurement of both absorption and transmission spectra are deemed ideal for extracting accurate collective-light-matter coupling values.

4.4 Conclusions

Our comprehensive investigation has unraveled the intricate relationship between molecular disorder and VRS in molecular polaritons. We have derived precise analytical expressions for absorption, transmission, and reflection spectra across various disorder distributions. Furthermore, our study introduces a generalized sum rule for determining the collective light-matter coupling under any form of disorder. These findings not only clarify the nuanced behavior of VRS amidst disorder but also establish a reliable framework for extracting light-matter coupling parameters with high accuracy from experimental data. In practical terms, when the experimental setup allows access to both transmission and absorption signals, the sum rule can be readily applied. In situations where accessing both signals is not possible, researchers can leverage Eq. 4.2-4.4, coupled with the analytical forms of the molecular susceptibility outlined in Table 4.1, to effectively fit their experimental results. Both these approaches ensure the extraction of the correct value of $g\sqrt{N}$ in the presence of disorder of any magnitude. Additionally, for scenarios involving mild disorder, the simplified expressions provided in Table 4.3 offer a convenient solution for data fitting. Furthermore, our study has unveiled a fascinating phenomenon associated with rectangular disorder – the emergence of narrow sidebands alongside a broad central peak. This intriguing line narrowing, observed in the presence of significant disorder, suggests a higher degree of coherence lifetime within the system. Such behavior is especially promising for applications requiring long-lived coherences between the cavity and molecules, providing an exciting avenue for future research in the realm of molecular polaritons.

Chapter 4, in full, is adapted from the material as it appears in "Extracting accurate light-matter coupling from disordered polaritons," by K. Schwennicke, N. C. Giebink, and J. Yuen-Zhou, *Nanophotonics* (2024) [68]. The dissertation author was the primary investigator and author of this paper.

Chapter 5

Classical linear optics effects in molecular polaritonics

5.1 Introduction

The interaction of matter with light drives numerous chemical, physical, and biological processes, and typically lies within the "weak" coupling regime in nature. Here, light and matter are considered distinct entities where the former perturbatively influences the latter. This weak coupling is attributed to the rate of energy exchange between light and matter being slow compared to their natural dissipation rates, and well-defined light absorption and emission events can be identified. By confining the radiation field within a small mode volume, light and matter can coherently exchange energy multiple times before the photon escapes, giving rise to the "strong" coupling regime. In this regime, light and matter yield hybrid eigenmodes known as polaritons.

The hybridization of light and matter excitations in crystalline solids outside of cavities has been long known since the seminal works of Tolpygo [11] and Huang [12] on phonon-polaritons and Agranovich [13] and Hopfield [14] on exciton-polaritons in the 1950s. It wasn't, however, until 1992 that Weisbuch [15] demonstrated that these strong coupling phenomena in inorganic semiconductors could be enhanced with optical microcavities (this statement is not always true, as recent work has shown that dielectric contrast between a bulk semiconductor and its surroundings can give rise to effective polariton formation too [16]). A few years later,

Lidzey [17] reported the same feat with excitons in disordered organic films. The study of strong coupling for ensembles of molecular vibrations is much more recent [18, 19], yet serves as a testament to the ubiquity of polaritonic phenomena across the electromagnetic spectrum.

Today, the burgeoning field of polaritonics shows promise in diverse applications ranging from manipulating chemical reactivity in both ground [20, 21, 22, 23, 24] and excited states [25, 26, 27, 28, 29, 30, 31, 32, 216] to enhancing exciton transport [33, 34, 35, 36, 37, 38], facilitating long-range energy transfer [39, 217, 40, 41, 42, 43, 44], enabling room temperature polariton condensation [45, 46, 47, 48, 218, 49], altering organic photophysical dynamics [50, 51, 52, 53, 54, 219], and modifying phase transitions [55]. Despite these advancements, the field is still marked by contradictory findings, with some studies reporting no polaritonic modification to chemical reactivity [56, 57, 58, 59] and little to no modification to spin conversion rates [60, 220]. Furthermore, with respect to modification of phase transitions, recent reports find that the re-scaling of the local temperature inside the cavity with respect to the temperature measured outside the cavity is the dominant mechanism over the proposed mechanism of renormalization of the material's free energy [61, 62]. This mix of positive and negative results underscores the nascent nature of the field and the need for further experimental and theoretical understanding, as highlighted by recent perspectives [63, 64, 65].

In an attempt to deepen this understanding at the recent Strong Coupling with Organic Molecules Conference (SCOM 2023 in La Jolla, California), an important discussion came to the limelight as to the need of drawing a clear divide between phenomena that can be understood solely through the language of classical optics, and those that go beyond this description. Amidst this and similar discussions, a curious revelation has emerged: consistently, classical optical methods, notably linear ones like transfer matrix methods [221, 222, 223, 224], elucidate many experimental findings [225, 226, 227], even in the realm of nonlinear optics [228, 229, 43, 230, 231, 232]. This begs the question: Why does classical linear optics elucidate phenomena attributed to molecular polaritons? Could it be that the language of cavity quantum-electrodynamics is unnecessary under certain circumstances?

This perspective endeavors to provide a succinct yet comprehensive, account of a class of molecular polaritonic phenomena that can be easily understood through the lens of classical optics, and in particular, of linear optics. Drawing from our own work [209] and seminal works of Keeling and coworkers [208, 233], we begin by establishing a theoretical framework for understanding linear polaritonic spectra in the limit $N \to \infty$, where N is the number of molecules coupled to each photon mode. In the regime where the polaritonic transmission and bare molecular absorption spectra are well separated in frequency, we make a connection to classical transfer matrix methods, demonstrating the agreement between the large N limit and the classical linear optics. Finally, we connect this frequency domain picture to the dynamical perspective offered by the recently developed Collective dynamics Using Truncated Equations (CUT-E) method [234, 189].

We provide explicit examples where seemingly nontrivial polaritonic phenomena can be easily explained with linear optics concepts. In the examples presented, it observed that both the relative steady-state populations and short-time dynamics obtained by pumping polaritonic systems with a broadband pulse, are identical to the situation of pumping the bare molecular system outside of the cavity with a filtered laser pulse whose intensity profile matches the polariton transmission spectrum. This observation cautions making claims of "polaritonic" effects before optical filtering has been judiciously ruled out. We further argue that a large number of nonlinear optical experiments can also be understood via optical filtering arguments, albeit with the caveat that the corresponding transmission spectrum through which filtering occurs is itself a (time-dependent) function of the molecular excitation dynamics. Finally, we discuss the limitations of this approach, particularly in the limit of finite N (*i.e.*, few-molecule strong coupling), and in other situations that extend beyond this classical optics treatment of molecular polaritons.

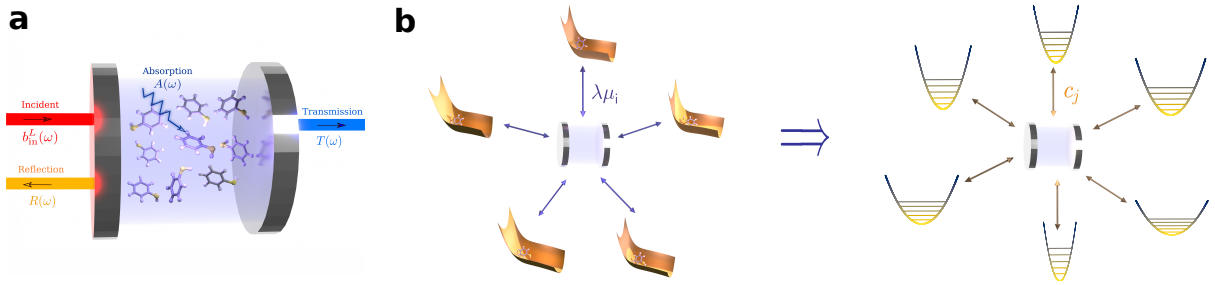

Figure 5.1. *Molecular polaritons and their spectroscopies*: (a) Linear spectroscopy as transmission, absorption, and reflection. (b) The molecular polariton problem, where anharmonic degrees of freedom of a large number N of molecules are coupled to a single (harmonic) photon mode can be regarded as a quantum impurity model. When $N \to \infty$, the reduced dynamics of the photon can be computed exactly by replacing the molecular degrees of freedom with a surrogate harmonic bath (Figure adapted from Ref. [209]).

5.2 Theory

5.2.1 Exact solutions of the polariton Hamiltonian

This section explores the scenario where N molecules are coupled to a single (harmonic) cavity mode of frequency ω_{ph}. The relevant Hamiltonian is the Tavis-Cummings Hamiltonian, extended to include the molecular vibrational degrees of freedom [181, 234, 209, 235]:

$$H = H_{mol} + H_{ph} + V, \tag{5.1}$$

where,

$$H_{ph} = \hbar\omega_{ph} a^{\dagger} a, \qquad H_{mol} = \sum_{i}^{N} H_i(q_i, Q_i), \tag{5.2}$$

are the zeroth order bare cavity and molecular Hamiltonians respectively and

$$V = -\hbar\lambda(a + a^{\dagger})\mu \tag{5.3}$$

is the dipolar light-matter interaction. Here a is the photon annihilation operator that satisfies $[a, a^\dagger] = 1$, and $H_i(q_i, Q_i)$ is the molecular Hamiltonian for the i-th molecule, depending on the respective electronic q_i and nuclear Q_i degrees of freedom. In Eq. 5.3, $\mu = \sum_i \mu_i(q_i, Q_i)$ is the molecular dipole operator and $\hbar\lambda = \sqrt{\frac{\hbar\omega_{ph}}{2\varepsilon_0 \mathscr{V}_{ph}}}$ is the vacuum electric field. The scalar ε_0 is the vacuum permittivity and $\mathscr{V}_{ph}$ is the cavity mode volume (hereafter, we consider for simplicity the case where the molecular sample volume $\mathscr{V}_{mol} = \mathscr{V}_{ph}$).

Typically, the number of molecules per cavity modes is $N \approx 10^7$ for electronic strong coupling [236] and $N \approx 10^{12}$ for vibrational strong coupling [237] (See Section D.1 for calculations). Considering the photon mode as the *system* and the molecular degrees of freedom as the *bath*, the polariton setup can be mapped to a quantum impurity model with the *impurity* (system) being coupled to a 'large' environment. Makri [238] has demonstrated that, in the limit of an infinite *bath* size ($N \to \infty$), and starting from an uncorrelated thermal system-bath state, the *reduced system dynamics* can be exactly obtained by replacing the complex anharmonic molecular bath with a surrogate bath of harmonic oscillators, $H_{mol} \to H_{mol}^{\text{eff}} = \sum_j \hbar\omega_j b_j^\dagger b_j$, coupled to the impurity (cavity mode), $V \to V^{\text{eff}} = -(a + a^\dagger)\sum_j \hbar\bar{c}_j (b_j + b_j^\dagger)$, where $\bar{c}_j$ are the respective effective couplings.

In recent work, we have generalized this result to any arbitrary uncorrelated stationary initial state (not necessarily thermal) [209]. This mapping is a consequence of the central limit theorem, and relies on the fact that the n^{th} order bath correlation functions, for $n > 2$, decay with increasing system size at a rate of $\mathscr{O}(N^{-1/2})$, given that the single molecule coupling strengths, $\bar{c}_i = \mathscr{O}(N^{-1/2})$, a condition typically satisfied in the polariton problem [209]. This vanishing of the higher-order correlations essentially translates to the cavity probing only the linear response of the molecular bath. Owing to an argument by Fano, the linear response of an anharmonic n-level system can be decomposed into the response of independent harmonic oscillators at each transition frequency (see Eq. 5.6) [239, 240]. These transitions correspond to the harmonic frequencies contributing to the surrogate bath [209, 241, 208].

Table 5.1. Molecular polariton linear spectra for arbitrary N and $N \to \infty$

Signal	Arbitrary N[a]	$N \to \infty$
$A(\omega)$	$-\kappa_L[\kappa\lvert D^{(R)}(\omega)\rvert^2 + 2\Im D^{(R)}(\omega)]$	$\frac{\kappa_L \omega_{ph} \Im\chi(\omega)}{\lvert\omega-\omega_{ph}+i\frac{\kappa}{2}+\frac{\omega_{ph}}{2}\chi(\omega)\rvert^2}$
$T(\omega)$	$\kappa_L\kappa_R\lvert D^{(R)}(\omega)\rvert^2$	$\frac{\kappa_L\kappa_R}{\lvert\omega-\omega_{ph}+i\frac{\kappa}{2}+\frac{\omega_{ph}}{2}\chi(\omega)\rvert^2}$
$R(\omega)$	$1+2\kappa_L\Im D^{(R)}(\omega)+\kappa_L^2\lvert D^{(R)}(\omega)\rvert^2$	$1-\frac{\kappa_L\left[\kappa_R+\omega_{ph}\Im\chi(\omega)\right]}{\lvert\omega-\omega_{ph}+i\frac{\kappa}{2}+\frac{\omega_{ph}}{2}\chi(\omega)\rvert^2}$

[a]Here $D^{(R)}(\omega) = -i\int_{-\infty}^{\infty} dt e^{i\omega t}\Theta(t)\langle[a(t),a^\dagger]\rangle$ is the retarded Green's function of the cavity.

5.2.2 Spectroscopic observables from the photon Green's function

It can be shown that standard polaritonic linear spectroscopic observables can be expressed in terms of the retarded Green's function of the cavity,

$$D^{(R)}(\omega) = -i\int_{-\infty}^{\infty} dt e^{i\omega t}\Theta(t)\langle[a(t),a^\dagger]\rangle \tag{5.4}$$

(see Tab. 5.1), where $\langle\ldots\rangle$ denotes a trace with respect to the initial system bath density matrix. In the limit $N \to \infty$, the mapping discussed above reduces the polariton problem into one of the linearly coupled harmonic oscillators: the originally harmonic cavity photon mode couples to the surrogate harmonic bath, leading to readily obtainable analytical solutions [209, 208, 233, 68].

In the $N \to \infty$ limit, the frequency-resolved absorption, transmission, and reflection in the first excitation manifold, under the rotating wave approximation (RWA) in the cavity-laser interaction, are [209]:

$$A(\omega) = \frac{\kappa_L \omega_{ph} \Im\chi^{(1)}(\omega)}{\lvert\omega-\omega_{ph}+i\frac{\kappa}{2}+\frac{\omega_{ph}}{2}\chi^{(1)}(\omega)\rvert^2}, \tag{5.5a}$$

$$T(\omega) = \frac{\kappa_L\kappa_R}{\lvert\omega-\omega_{ph}+i\frac{\kappa}{2}+\frac{\omega_{ph}}{2}\chi^{(1)}(\omega)\rvert^2}, \tag{5.5b}$$

$$R(\omega) = 1 - A(\omega) - T(\omega). \tag{5.5c}$$

Here the cavity line width is $\kappa = \kappa_L + \kappa_R$, with the cavity decay rates into the left and right photon continua denoted by κ_L and κ_R. The molecular linear susceptibility [240] is given by

$$\chi^{(1)}(\omega) = \lim_{\gamma \to 0^+} \frac{1}{\hbar \varepsilon_0 \mathscr{V}_{mol}} \sum_{y,z} [p_y - p_z] \frac{|\langle z|\mu|y\rangle|^2}{\omega_{zy} - \omega - i\frac{\gamma}{2}} \tag{5.6}$$

where $\mathscr{V}_{mol}$ is the volume of the molecular sample, $|y\rangle$ and $|z\rangle$ are the many-body eigenstates of H_{mol} in Eq. 5.2, and p_y and p_z are the corresponding initial populations. It is important to note here that although Eqs. 5.5a, 5.5b, and 5.5c assume the RWA in the cavity-laser interaction and a single photon mode interacting with the molecules, the implications hold beyond the RWA and for a multimode cavity as Ćwik *et al.* [208] imply. The validity of this formalism for a multimode cavity relies on the fact that, in the regime of $N \to \infty$, the different cavity modes do not couple [208, 36], allowing for mode-wise separation of the photon Green's function, $D_k^{(R)}(\omega)$.

This formalism presented above is quite significant, given that, over the years, a variety of computational methods have been developed for the simulation of the polariton spectra. These include quantum optical methods based on input-output theory that require simplification of the rich molecular complexity [242, 243, 244, 245], to models incorporating *ab initio* treatments, but limited to a single or a few molecules within a cavity [246]. Eqs. 5.5a, 5.5b, and 5.5c essentially demonstrate that linear polaritonic spectra can be computed directly using the molecular linear susceptibility of the bare molecule outside the cavity, avoiding explicit simulations with N molecules coupled to a photon mode. This idea is reminiscent of classical optical transfer matrix methods, presented in the following section.

5.2.3 Connection to classical linear optics: Transfer matrix methods

The simplified dependence on the molecular linear susceptibility within Eqs 5.5a-5.5c parallels classical optics treatments, particularly transfer matrix methods (TMM) [221, 222, 223]. A typical TMM expression for the transmission through a Fabry-Perot cavity of length $\mathscr{L}$

containing a dielectric molecular sample is

$$T(\omega) = \frac{T_L T_R e^{-\alpha(\omega)\mathscr{L}}}{|1 - \sqrt{R_L R_R} e^{-\alpha(\omega)\mathscr{L}} e^{i\frac{4\omega n(\omega)\mathscr{L}}{c}}|^2}, \tag{5.7}$$

where $T_{L,R}$ and $R_{L,R}$ are the transmission and reflective of the left and right mirrors and $\alpha(\omega)$ and $n(\omega)$ are the frequency-dependent absorption coefficient and refractive index for the molecular sample. Assuming that the cavity mirrors are highly reflective and the molecular absorptivity rapidly decays away from the molecular resonance, the TMM expression for transmission near the polariton frequencies approximates to:

$$T(\omega) \approx \frac{T_L T_R {\omega_{FSR}}^2}{4\pi^2 |\omega - m\omega_{FSR} + i\frac{\omega_{FSR}}{4\pi}(T_L + T_R) + \frac{\omega}{2}\chi^{(1)}(\omega)|^2}, \tag{5.8}$$

where $\omega_{FSR} = \frac{\pi c}{\mathscr{L}}$, m is a positive integer, and $\chi^{(1)}(\omega) = [n(\omega) + i\frac{1}{2}\frac{c}{\omega}\alpha(\omega)]^2 - 1$ is the linear susceptibility of the molecular sample. By taking $\frac{T_{L,R}\omega_{FSR}}{2\pi} \to \kappa_{L,R}$ and $m\omega_{FSR} \to \omega_{ph}$, and $\frac{\omega}{2}\chi^{(1)}(\omega) \to \frac{\omega_{ph}}{2}\chi^{(1)}(\omega)$, the quantum mechanical expression emerges (see Eq. 5.5b). This agreement between TMM and the quantum treatment in the large N limit elucidates the success of classical linear optics methods at modeling the molecular polariton spectra in the collective strong coupling regime.

5.2.4 Polariton linear absorption as optical filtering

A closer inspection of Eqs. 5.5a and 5.5b reveals an intuitive relation,

$$A(\omega) = \frac{\omega_{ph}\Im\chi^{(1)}(\omega)}{\kappa_R} T(\omega). \tag{5.9}$$

This equation shows that absorption within the cavity is directly proportional to the product of the bare molecular absorption $\Im\chi^{(1)}(\omega)$ outside of the cavity and the polariton transmission spectrum $T(\omega)$. Viewed through the lens of linear optics (pun intended), the polariton transmission peaks function as "optical filters" [32], selectively allowing radiation from select frequencies from

outside to enter the cavity, where the molecules absorb based on their bare spectrum. This is consistent with the work of Groenhof et al. which finds through molecular dynamics calculations that the population transfer between polaritons and dark states is determined by the overlap between the polaritonic and molecular absorption spectra [247].

5.2.5 Quantum dynamics perspective

The result that the polariton transmission peaks function as optical filters not only applies to the linear polaritonic response, but also to all dynamical processes occurring before high-order bath correlation functions become relevant [238]. In this context, this corresponds to all molecular processes before relaxation from dark states to polaritons. We can understand this by carefully examining the large N limit at the core of the derivation of Eq. 5.9. Here we do so using our formalism called Collective dynamics Using Truncated Equations (CUT-E) [234], which in the large N limit is equivalent to the formalism independently developed by Cui and Nitzan [248], and whose implications are consistent with the works by the group of Keeling [233, 249].

CUT-E is a formalism that dramatically simplifies the quantum dynamics of molecular polaritons by separating the light-matter coupling term into its collective and single-molecule components [234, 189]. In the large N limit, the latter can be treated perturbatively, which gives rise to a hierarchy of timescales where ultrafast collective effects $\mathcal{O}(g\sqrt{N})$ are separated by much slower single-molecule effects $\mathcal{O}(g)$, where $g = \lambda \cdot \mu_i$ is the single molecule light-matter coupling strength. Notably, this hierarchy is preserved even in the presence of disorder (dCUT-E) [189]. The most important conclusion from CUT-E is that collective light-matter coupling operates while molecules remain at their Franck-Condon (FC) configuration. Therefore, Rabi oscillations are dominated by Rayleigh-like molecular processes, while Raman-like processes (emission and absorption events that create phonons in the ground electronic state) become relevant only at longer timescales (see Fig. 5.2). This observation is consistent with previous works by Spano in the context of J-aggregates [250], and the works by Cui [248] and Keeling [233, 249] in the context of molecular polaritons. Keeping the collective coupling $g\sqrt{N}$ constant and finite (since

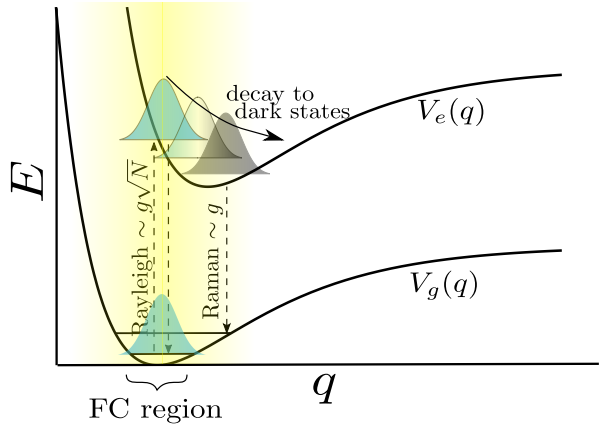

Figure 5.2. *Collective and single-molecule coupling effects*: Light-matter coupling is collectively enhanced while molecules remain at their FC region, *i.e.*, while inter-exciton coherence is preserved. This implies that only Rayleigh-like processes are relevant in the large N limit (Figure adapted from Refs. [234, 189]).

it is an experimental observable), the limit $N \to \infty$ is equivalent to $g \to 0$, and consequently leads to the dismissal of single-molecule light-matter processes $\mathscr{O}(g)$ such as radiative pumping and Raman scattering (an approximation referred to as zeroth-order CUT-E). This limit is valid for Eqs. 5.5a-5.5c since the spectroscopic measurement is faster than single-molecule processes ($\sim$ ns for the UV-visible and $\sim$ ms for the IR). Therefore, the cavity can solely probe Rayleigh-like processes, and hence only the molecular linear susceptibility $\chi^{(1)}(\omega)$ (which is proportional to the two-point correlation function of the molecules, and hence harmonic) contributes to the polaritonic response [209] (See Section 5.2.1).

Under the assumptions discussed in the previous paragraph and in Section 5.2.1, Eq. 5.9 suggests that molecular dynamics triggered by pumping the polaritonic system with a linear optical source can be reproduced by choosing the right linear laser pulse outside of the cavity. In Section 5.3.3 we provide quantum dynamics simulations to demonstrate this. Crucially, in the example mentioned, the polaritonic system is initiated with a broadband pulse, while the bare molecular system is initiated with a pulse whose intensity profile mimics the polariton transmission spectrum. In the bare molecular case, the shaped pulse initiates the same excited state wavepacket that is created *in-situ* via Rabi oscillations for the broadband excited polaritonic

case. This analysis indicates that, although changes in chemical dynamics between inside and outside the cavity are observed when identical pulses are used (e.g., one of our recent works in Ref. [189]), such differences vanish with the right choice of the laser pulse that prepares the bare molecular system in the correct initial state (see Section 5.3.3).

It is worth mentioning that using an optically filtered linear source to excite the bare molecules will not reproduce the ultrafast polariton dynamics unless the resulting light is also coherent. However, it is well known that coherent and incoherent optical sources yield the same result at steady state (in this context, steady-state occurs after decay to dark states but before relaxation back to the polaritons), as pointed out by Brumer and Shapiro when demystifying one-photon laser control schemes [251]. Therefore, whether one uses a shaped coherent pulse or a filtered incoherent source, the same steady-state will be observed outside as compared to inside the cavity.

5.3 Examples of collective polaritonic effects behaving as optical filtering

This section employs a linear optics viewpoint to demystify cavity-mediated non-statistical energy redistribution, control of photoreactivity, and short-time excited state dynamics. These phenomena have been discussed in the literature as polaritonic phenomena of interest. While we do not question their correctness, we want to demystify them in light of the very simple insights discussed in the last section. In each instance, the limit $N \to \infty$ is considered, enabling direct application of Eq. 5.9. As such, we find that we can obtain similar results outside of the cavity by using a laser field that has the same intensity profile $|E(\omega)|^2$ as the polariton transmission spectrum $T(\omega)$. As discussed in the previous Section, Eq. 5.9 not only pertains solely to steady-state molecular populations but also implies that even the short-time ($t < 1/g$) excited state dynamics coincide. In this Section, we numerically verify this result. It is important to note, however, that these findings do not consider dynamics at longer times nor when strong

coupling is attained with small N, caveats that will be discussed in subsequent sections.

5.3.1 Non-statistical energy redistribution

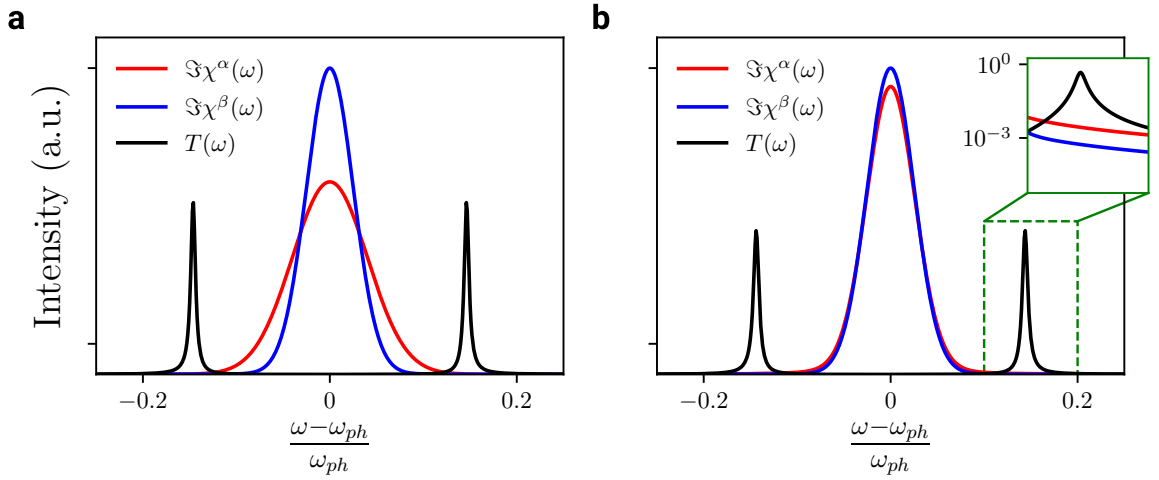

Figure 5.3. *Demystifying cavity-mediated "non-statistical" energy redistribution*: Molecular species α and β are modeled as two Voigt profiles centered at the same frequency. The two species are simultaneously coupled with the same collective coupling strength $g\sqrt{N}/\omega_{ph} = 0.1$ to a single resonant cavity mode with $\kappa/\omega_{ph} = 2\kappa_R/\omega_{ph} = 2\kappa_L/\omega_{ph} = 0.01$. (a) In this instance, α and β have the same Lorentzian (homogeneous) broadening ($\sigma_L^{\alpha,\beta}/\omega_{ph} = 0.001$), but α features larger Gaussian (inhomogeneous) broadening ($\sigma_G^{\alpha}/\omega_{ph} = 0.04$) compared to β ($\sigma_G^{\beta}/\omega_{ph} = 0.025$). Here, the spectral overlap between α and the polariton transmission $T(\omega)$ spectrum is notably larger, and the result is that the ratio of the total energy absorbed by α over that absorbed by β is $\Delta E^{\alpha}/\Delta E^{\beta} = 2.2$. (b) Here α and β have the same inhomogeneous broadening $\sigma_G^{\alpha,\beta} = 0.025$, but α has larger homogeneous broadening, $\sigma_L^{\alpha}/\omega_{ph} = 0.005$, than β, $\sigma_L^{\beta}/\omega_{ph} = 0.001$. Despite the superficial similarity of their absorption bands outside of the cavity due to the predominant inhomogeneous broadening, we find that $\Delta E^{\alpha}/\Delta E^{\beta} = 2.7$, an outcome that seems surprising at first glance. The inset (which is log scale) highlights that while the centers of the molecular profiles are similar, the tails of α are considerably fatter, leading to a larger spectral overlap with $T(\omega)$. Therefore, while scenarios (a) and (b) may seem distinct, their outcomes are explained by the same underlying mechanism.

In this example, we consider a system where two molecular species couple to a single cavity mode, and upon optical excitation of the cavity, the polaritons selectively funnel energy into one of the species with a "non-statistical" energy redistribution that differs from what one would expect if the same excitation acted directly on the molecules outside the cavity. This

intriguing phenomenon has been originally studied with computational rigor by Groenhof and Toppari [252] for a scenario involving up to 1,000 molecules of one species and revisited by Pérez-Sánchez et al. [234] in the limiting case that the number of both molecules tends to infinity. The intriguing observation in both studies is that even though excitation energy might start in one of the species or in both, eventually it can funnel selectively into the molecule that features the fastest dephasing. This phenomenon was explained with a time-domain interpretation where the cavity and the molecules exchange energy, and the molecule with the fastest dephasing absorbs energy at a faster rate, therefore returning less of its excitation energy back to the cavity at every Rabi oscillation. There is no mistake in this interpretation, but there is a much simpler reasoning behind the observations. The Rabi cycling of energy between molecules and cavity is just the filtering of a broadband pulse through the polariton windows. At long times, a frequency-domain picture clarifies the mechanism behind this energy funneling. From Eq. 5.9, for two distinct, non-interacting molecular species α and β coupled to the same cavity mode, the collective molecular absorption inside the cavity is

$$A(\omega) = A^{(\alpha)}(\omega) + A^{(\beta)}(\omega) \tag{5.10}$$

where $A^{(\alpha,\beta)}(\omega) = \frac{\omega_{ph}\Im\chi^{(1\alpha,\beta)}(\omega)}{\kappa_R}T(\omega)$ is the absorption by molecular species α,β in the cavity. The insight from Eq. 5.10 clarifies the origin of the non-statistical energy redistribution, or funneling, for this system: the molecular species exhibiting the largest overlap between its bare absorption spectrum and the polariton transmission peaks absorbs the most energy.

Fig. 5.3 showcases two instructive theoretical scenarios that elucidate the connection between the bare molecular spectral overlap with the polariton transmission spectrum and the ratio of the total energy absorbed by molecular species α (ΔE^{α}) to the total energy absorbed by molecular species β (ΔE^{β}) upon broadband excitation:

$$\frac{\Delta E^{\alpha}}{\Delta E^{\beta}} = \frac{\int d\omega \Im\chi^{(1\alpha)}(\omega)T(\omega)}{\int d\omega \Im\chi^{(1\beta)}(\omega)T(\omega)}, \tag{5.11}$$

In both instances, the species with a more significant spectral overlap with the polariton transmission spectrum exhibits greater energy absorption. Notably, Fig. 5.3b emphasizes the significance of the Lorentzian (homogeneous) tails of the linear molecular absorption spectrum in this energy absorption process (see inset). In passing, we note that a similar explanation also serves to demystify the celebrated result by Houdré [194] on why for sufficiently strong light-matter coupling, polaritons showcase the homogeneous (Lorentzian) but not the inhomogeneous (Gaussian) broadening of their parent molecules: Gaussian tails die faster than Lorentzian ones so, for large Rabi splittings, polaritons only overlap significantly with the latter.

Viewed through the lens of linear optics, polariton peaks function as optical filters, determining the specific frequencies from the broadband pulse that are permitted into the cavity. Consequently, the molecular species that overlaps more substantially with these frequencies absorbs the greater amount of energy. In fact, if a linear optical source mimicking the intensity profile of the polariton transmission spectrum is employed outside of the cavity, the ratio of the energy absorbed by the two molecular species is the same outside of the cavity as it would be by shining a broadband pulse onto the polaritonic system:

$$\frac{\Delta E^{\alpha}}{\Delta E^{\beta}} = \frac{\int d\omega \omega \Im \chi^{(1\alpha)}(\omega)|E(\omega)|^2}{\int d\omega \omega \Im \chi^{(1\beta)}(\omega)|E(\omega)|^2}, \tag{5.12}$$

where $|E(\omega)|^2 \propto \frac{T(\omega)}{\omega}$. This linear optics perspective offers a unified framework for interpreting previous findings. In Ref. [252], the preferential energy channeling to hydroxyphenylbenzothiazole (HBT) over rhodamine (Rho) when the lower polariton is excited can be attributed to the bare HBT linear absorption having more substantial overlap with the lower polariton compared to that of Rho. Similarly, the observation that one molecular species predominates in energy absorption over the other, despite apparent spectral similarities [234], is explained by the dominant molecule having more pronounced tails in its absorption spectrum that align with the polariton peaks. The complex dynamics at each Rabi cycling corresponds to transients of the frequency filtering that the cavity polaritons enact on a broadband pulse. However, these

transients are immaterial if one is asking for steady-state observables such as the energy redistribution into molecules excitations of α and β. These insights underscore that in the limit of $N \to \infty$, the relative steady-state molecular populations can be straightforwardly deduced from the interplay between the linear polariton and the bare molecular spectra.

5.3.2 Changes in photoreactivity

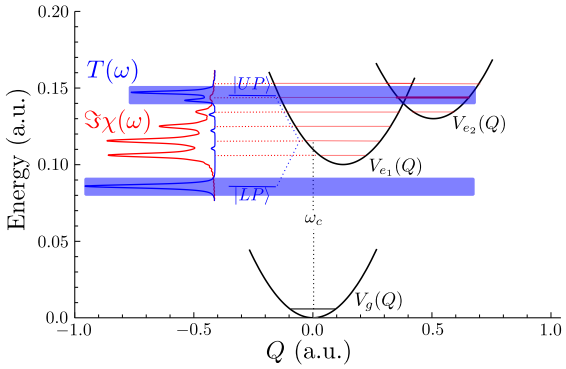

Figure 5.4. *Photoreactivity of molecular polaritons I*: We consider a molecule that consists of a ground electronic state g and two excited electronic states e_1 and e_2, where only the $g \to e_1$ transition is coupled to the cavity mode. The potential energy surfaces $V_{g/e_{1,2}}(Q)$ are parameterized by a single nuclear vibrational coordinate Q. The inset illustrates, for zero disorder, the spectral overlap between the linear polariton transmission $T(\omega)$ under strong coupling and the bare molecular absorption $\Im\chi(\omega)$ outside of the cavity. Note that the upper polariton (UP) overlaps with states high in e_2 character, while the lower polariton (LP) does not overlap with any significant features of the bare molecular spectrum.

Here, we delve into changes in photoreactivity of a disordered ensemble of molecules coupled to a single cavity mode, utilizing a similar d-CUT-E effective Hamiltonian that we previously deployed [189] (see Fig. 5.4). Just like in the previous section, both inside and outside the cavity, the system is excited with a broadband pulse facilitating a comparison of the excited state population dynamics in both scenarios (see Fig. 5.5). In the absence of disorder (Fig. 5.5b), initial observations suggest that strong coupling significantly alters photoreactivity compared to the bare molecule scenario, as evidenced by an increased e_2 to e_1 population ratio $P_{e_2}(t)/P_{e_1}(t)$ at a time $t \sim 30$ fs. As disorder increases (Figs. 5.5d and 5.5f), this population ratio gradually

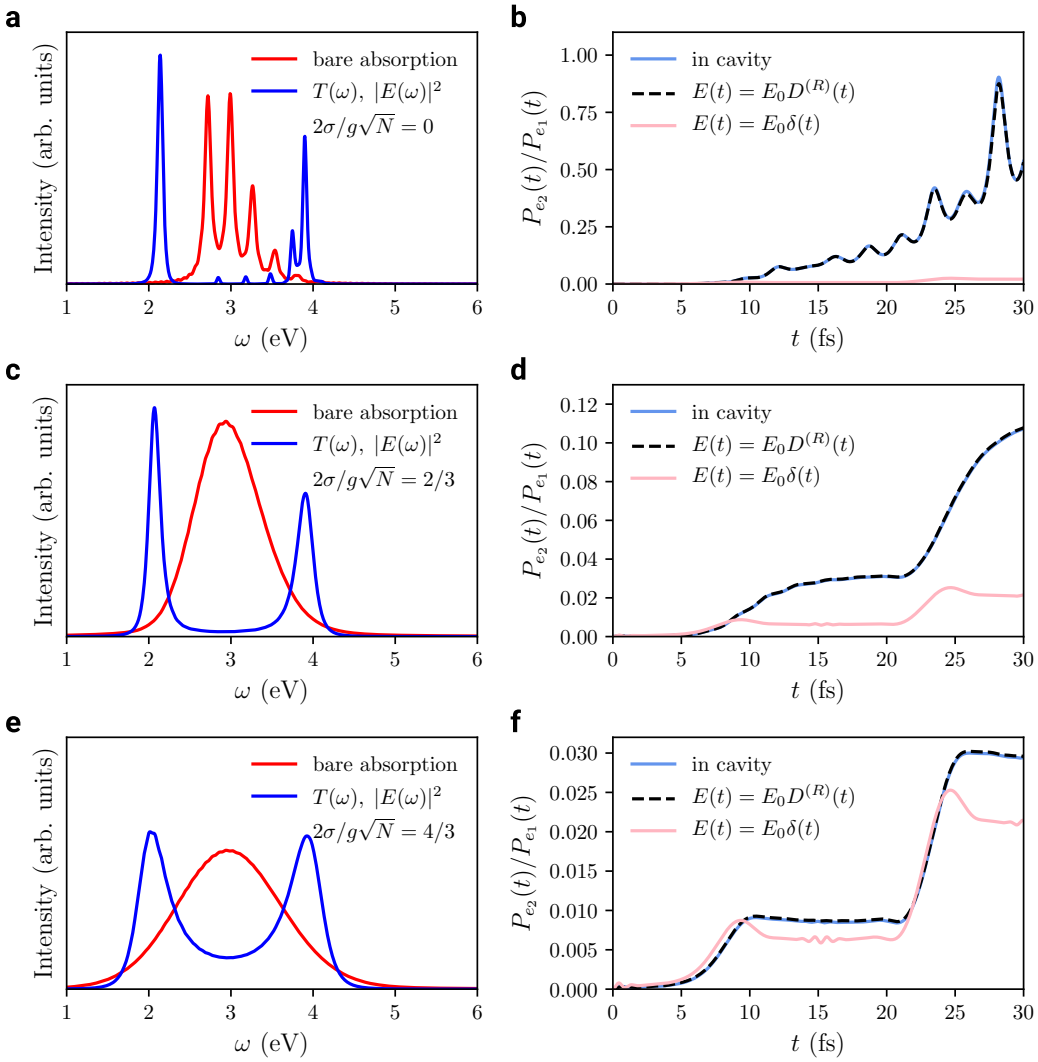

Figure 5.5. *Photoreactivity of molecular polaritons II*: Panels (a,c,e) depict the overlap between the bare molecular absorption spectrum with the polariton transmission spectrum $T(\omega)$ under strong coupling and a laser field with an identical intensity $|E(\omega)|^2$ across varying degrees of molecular disorder σ. The in-cavity simulations were carried out with a collective light-matter coupling of $g\sqrt{N} = 0.816$ eV. Panels (b,d,f) present the corresponding short-time excited state dynamics for inside and outside the cavity. In the latter case both a shaped pulse $E(t) = E_0 D^{(R)}(t)$ and a delta pulse $E(t) = E_0\delta(t)$ are considered. Notably, the photoreactivity appears enhanced in the cavity when compared to the delta pulse scenario; however, the dynamics align with those observed using an external pulse shaped to match the polariton transmission spectrum's intensity profile. As molecular disorder increases, the dynamics for both in-cavity and shaped external pulse scenarios converge with those observed using a broadband pulse externally. This convergence is attributed to the increased spectral overlap between $T(\omega)$ and $|E(\omega)|^2$ with the bare molecular absorption, mirroring the conditions of employing a broadband pulse externally.

aligns with that observed outside the cavity.

Drawing from the insights gained in Section 5.3.1, in the disorder-free scenario, the upper polariton (UP) transmission window coincides with a peak in the bare molecular spectrum predominantly characterized by e_2, while the lower polariton (LP) transmission overlaps slightly with the low-energy tail of the molecular spectrum (see Fig. 5.4 inset). Eq. 5.9 aids in rationalizing the observed photoreactivity enhancement under strong coupling: the light that the cavity selectively channels through the polaritonic transmission windows significantly overlaps with the portion of the bare molecular absorption spectrum that is rich in product character. Additionally, as disorder increases, the polariton transmission spectrum more closely aligns with the reactant features of the bare molecular spectrum (see Figs. 5.5c and 5.5e), leading to a scenario where, within the cavity, linear absorption mimics that of a broadband pulse outside the cavity. This explains why our simulations inside the cavity tend towards the out-of-cavity scenario under broadband excitation with increasing disorder.

These results are in alignment with recent reports in the literature. Thomas et al. [58] has reported experimental results for the modification of the photoisomerization of spiropyran to merocyanin under strong coupling, proposing that the change was due to a non-polaritonic effect predominantly influenced by molecular absorption of ultraviolet radiation within the cavity. Concurrently, Dutta et al. [32] explored the ultrafast photochemistry of 10-hydroxybenzo[h]quinoline under strong coupling through molecular dynamics simulations and experiments, suggesting a key role played by the congruence between bright polaritons and molecular dark states. Together with our study, these findings indicate that at short times ($t < 1/g$), polaritons serve as selective optical "filters" [32] that allow specific frequencies into the cavity, which are then absorbed by the molecular (dark) states. As a result, when compared to excitation outside with a pulse whose intensity profile significantly differs from the polariton transmission spectrum, the photoreactivity changes under strong coupling because the available light within the cavity is now different in terms of its frequency distribution juxtaposed to the optical pump outside the cavity. For instance, if the polaritonic windows coincide with the bare molecular energy levels that lead

to a desired reaction pathway, that pathway will be selectively enhanced due to the increased *relative* absorption at those frequencies. Conversely, if the polaritonic windows overlap with less reactive, or unreactive, bare molecular states, the photoreactivity can be suppressed.

Similarly, this linear optics viewpoint provides another way to explain the same strong coupling control of photochemical processes through polaron decoupling [26, 27] in the $N \to \infty$ limit. This phenomenon was explained as a version of motional narrowing where the exchange of energy between light and matter is so fast that the LP does not "feel" much coupling to vibrations, with the consequence of suppressed reactivity. Calculations showed that the UP does not enjoy such polaron decoupling to the same degree, presumably due to strong mixing with high-lying vibronic states [233]. As an illustration, the inset of Fig. 5.4 shows that the LP transmission peak is off-resonant from any bare molecular vibronic transitions, therefore little to no absorption occurs so it is not surprising that no nuclear motion occurs upon excitation of the LP, and we expect a decrease in photoreactivity [26, 27]. There is nothing wrong about adjudicating the suppression of reactivity to polaron decoupling of the LP potential energy surface, but we believe it is much simpler to understand it in terms of the lack of absorption cross-section. Conversely, the UP is off-resonant from the dominant vibronic features, so we do expect some polaron decoupling, but the UP is resonant with a product peak leading to an enhancement in photoreactivity compared to exciting the reactant peak. Importantly, regardless of interpretation, in both scenarios the same suppression or enhancement can be achieved outside of the cavity by driving at the corresponding polariton frequencies: pumping at the LP frequency implies off-resonant pumping of the system, so little photoreactivity is expected, while at the UP frequency one is resonantly driving the product peak so an increase in photoreactivity is expected. This selective enhancement or suppression of reaction pathways based on the alignment of polaritonic and bare molecular states underscores the nuanced interplay between polaritonic effects and bare molecular linear absorption, highlighting the importance of considering both in the analysis of the excited state dynamics of polaritonic systems, as well as the importance of providing the correct comparison between inside and outside of cavity scenarios. It is crucial to

emphasize that the linear polaritonic response for systems under strong coupling with sufficiently small N may not be accurately captured by Eq. 5.9. Consequently, polaritonic phenomena in such cases *cannot* be described using an optical filtering viewpoint.

5.3.3 Short-time coherent dynamics

Until now, we have contrasted the short-time excited state dynamics under strong coupling with those obtained by broadband excitation of the molecular ensemble outside the cavity. However, as discussed in Section 5.2.5, we should observe exactly the same photoreactivity between this setup and the strong coupling arrangement if we instead use an optical pulse outside the cavity whose intensity profile has been "shaped" to mimic the polariton transmission spectrum. As an example, let us consider the case where the polaritonic system is pumped with a broadband pulse (a delta pulse in time). An appropriate choice for the optical pulse acting of the bare molecules is the one where the time-dependent electric field matches the strong coupling photon-photon correlation function, *i.e.*, $E(t) = E_0 D^{(R)}(t)$. The value of the constant field amplitude E_0 is chosen to be low enough to ensure we remain in the linear regime. Our simulations using the CUT-E method confirm that the photoreactivity of the bare molecules triggered by $E(t)$ is, up to a constant that depends on the value of E_0, *identical* to that observed inside the cavity (see Figs. 5.5b, 5.5d, 5.5f and Fig. 5.6). A common misunderstanding in the field is that Rabi oscillations, which give rise to the Rabi splitting in the linear polaritonic response, imply the existence of nonlinear optical processes. Here, we show that they can be reproduced in the linear regime simply via constructive and destructive interference between the excited state amplitudes promoted by the filtered pulse at different times (see Fig. 5.6). This phenomenon has been well-known for a long time in the field of ultrafast spectroscopy as linear wavepacket interferometry [253, 85]; in fact, nonlinear wavepacket interferometry has been suggested as an alternative to provide real "pump-dump" control and detection of molecular dynamics beyond the FC region [254, 255].

The presented example makes it evident that choosing the same initial state preparation

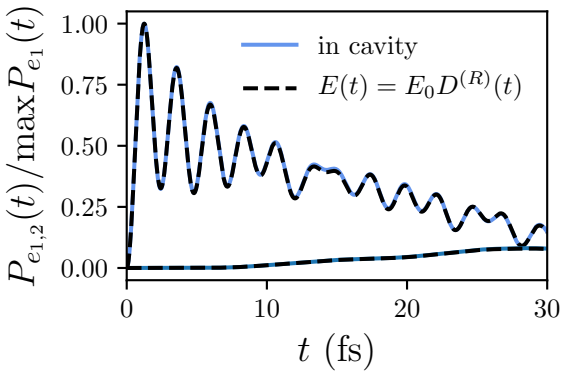

Figure 5.6. *Short-time coherent dynamics*: Short-time excited dynamics inside the cavity versus when the system outside of the cavity is driven with a time-dependent pulse $E(t)$ that has the same intensity profile as the polariton transmission spectrum. It is observed that the dynamics, up to a constant, are identical, with both scenarios presenting Rabi oscillations in the e_1 population dynamics.

conditions inside and outside of the cavity when performing quantum dynamics simulations can be misleading. Initial conditions outside the cavity must be sampled in a way that they account for the filtering of the hypothetical laser acting on the polaritonic system; otherwise, erroneous differences in the subsequent dynamics may occur.

5.4 Long-time polaritonic dynamics as optical filtering

As we have made clear throughout the discussion so far, the presented examples of linear optics, or "optical filtering", do not consider the long-time dynamics, *i.e.*, $t \sim 1/g$ or $t > 1/g$. At long times, Raman-like processes of $\mathcal{O}(g)$ begin to matter, leading to relaxation from the incoherent dark states to coherent polaritons. This relaxation can be through the single-molecule emission of a photon, *i.e.*, radiative pumping, or through vibrational relaxation [256]. The timescales of these processes are much slower than the Rabi oscillations.

Although we do not explicitly perform calculations that include these dark-state-to-polariton processes, the timescale hierarchy described in Section 5.2.5 allows us to understand the long-time dynamics as the alternation of two basic mechanisms that can be addressed separately: (1) relaxation from polaritons to dark states as optical filtering, and (2) slow relaxation from dark

states back to polaritons via radiative pumping and vibrational relaxation [257, 258]. We argue that in the large N limit step (1) can be described by linear optics even if multiple instances of step (2) have previously occurred, given that the latter is sufficiently slow to allow for "complete" exciton decoherence before polaritons are repopulated. In the following sections, we explain how decay to dark states to polaritons via radiative pumping can also be described as optical filtering, which allows the description of slow $\mathscr{O}(g)$ processes as multiple instances of optical filtering events.

5.4.1 Incoherent nonlinear spectroscopy of polaritons

The linear response implications of the quantum impurity model presented in Section 5.2 for $N \to \infty$ hold for arbitrary initial states so long as the light and matter are decoupled and stationary. As discussed in Subsection 5.2.1, this does not only include thermal states but can be equally applied to nonequilibrium stationary states resulting from optical pumping. As we shall argue, the stationarity condition can be taken liberally to mean "slowly varying with respect to the timescale corresponding to the spectral resolution". This is particularly relevant for a large class of incoherent nonlinear spectroscopy experiments, where, upon optical pumping, polaritons have relaxed into incoherent "dark states" away from the FC region, but have not fully thermalized, provided that the timescale corresponding to the dynamics of the dark states $\tau \gg \frac{2\pi}{\Gamma}$, where Γ can be regarded as the minimum of the cavity and molecular dephasing linewidth. The latter is a parameter that characterizes the decay rate of the photon-photon correlation function and hence dictates the resolution of the acquired spectrum. Thus any dynamics slower than the corresponding timescale, $\frac{2\pi}{\Gamma}$, can be treated adiabatically, ensuring the validity of the stationarity condition within the spectral resolution of the polaritonic spectrum; in other words, the molecular state can be regarded as frozen during that timescale. This means that the response triggered by the probe pulse can be regarded as the linear response of this "stationary state" which parametrically changes as a function of a coarse-grained waiting time τ [sampled at intervals coarser than $\mathscr{O}(2\pi/\Gamma)$] and can be characterized by an effective (time-dependent) molecular

susceptibility $\chi(\omega;t)$. Figs. 5.7 shows an illustration of an incoherent pump-probe experiment after optical pumping, for a simplified three-level system. Here a, b, and c represent the system at three different stationary non-thermal configurations at times $t_1 < t_2 < t_3$. In the regime where the time delay in the acquisition of the spectra, $\Delta t = t_i - t_{i+1}$, is greater than τ, the equations presented in Eq. 5.5 can be used to compute the spectroscopic observables. Thus the implications of the optical filtering presented in the previous sections hold, but with an important caveat: here the polariton windows change in time t, adiabatically adjusting to the $\chi(\omega;t = n\tau)$ at each configuration. It is not surprising then that a wide range of experimental ultrafast nonlinear spectroscopy studies [228, 229, 43, 230, 231, 232] successfully use transfer matrix methods with an effective time-dependent $\chi(\omega;t)$ (Eqs. 5.5, 5.7, and 5.8) to model their data.

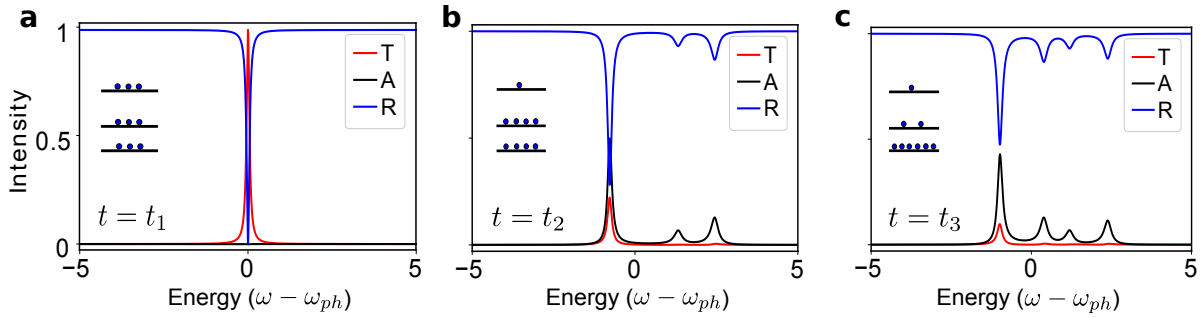

Figure 5.7. *Incoherent nonlinear spectroscopy of polaritons*: A representative example of a polaritonic incoherent nonlinear spectroscopic experiment showing transmission, reflection, and absorption for an ensemble of identical three-level systems with $\mu = \mu_{12} + \mu_{23} + \mu_{13}$, at three different configurations, (a) $p_1 = p_2 = p_3$, (b) $p_1 = 0.45$, $p_2 = 0.45$, $p_3 = 0.1$, (c) $p_1 = 0.7$, $p_2 = 0.2$, $p_3 = 0.1$, at times $t_1 < t_2 < t_3$ respectively and $\Delta t \gg \tau$, obtained upon optical pumping. The parameters used are: $\omega_{ph} = \omega_{12}, \omega_{23} = 2\omega_{12}$, $\kappa = 0.1, \gamma = 0.3$, and the collective light-matter coupling $\sqrt{N}g = 1$ (arbitrary frequency units). Configuration (a) represents the state created upon optical pumping with complete saturation rendering the medium transparent to the cavity. After a time of $t_2 - t_1$, upon relaxation, the system moves to (b) where the $|1\rangle \rightarrow |2\rangle$ transition is still saturated; hence we see three polariton peaks. Note that the molecules are still in a non-thermal stationary state. The system further relaxes to reach (c) at time t_3 and we can see all four polariton peaks appearing. The time-varying spectra have been computed using Eq. 5.5 with a molecular susceptibility, $\chi(\omega;t)$, that adjusts adiabatically to each configuration.

5.4.2 Radiative pumping as a form of optical filtering

For large but finite N, both experimental results [39] and phenomenological models [257, 258] suggest that the rate of radiative pumping is proportional to the bare molecular emission into polariton modes, modulated by the photon Hopfield coefficients. Therefore, photoluminescence via radiative pumping can be thought of as a form of optical filtering of molecular emission through polariton windows if photons quickly leak out of the cavity.

This phenomenon is analogous to bare molecular emission outside of a cavity. Despite laser-induced fluorescence being technically a third-order nonlinear optical signal, owing to the large separation of timescales between photoexcitation of the molecule and the formation of the Stokes-shifted incoherent emissive state, the emission of the latter can be regarded as the linear response triggered by the photonic vacuum. Similarly, in the cavity emission from the dark states can be regarded as the linear response of the bare molecules triggered by the empty polariton modes.

This optical filtering perspective of photoluminescence breaks down in two scenarios: 1) for small N, and 2) if the decay of polaritons to dark states is faster than cavity leakage, i.e., polaritons significantly overlap with the bare absorption of the molecules. We elaborate on the latter case below.

5.5 What is beyond optical filtering: The nontrivial polaritonic effects

5.5.1 Vibrational relaxation and other nontrivial ultrafast phenomena

Experimental studies report that there is an alternative mechanism for the repopulation of polaritons starting from incoherent dark states which is mediated by the matter component of the polaritons; this is known as *vibrational relaxation* [259, 260, 261] and cannot be explained as an optical filtering effect. However, this $\mathcal{O}(g)$ mechanism remains somewhat of a mystery, as it seems uncompetitive with radiative pumping when N is large [256, 237, 262]. A possible

resolution to this conundrum is to note that this value of N is at most a parameter that is made to fit the coarse-grained model of a molecular ensemble coupled to a single-mode cavity, while the real system contains many modes, albeit still at a giant ratio of $\sim 10^6$ molecules per photon mode. It could be that upon account of the photon dispersion, vibrational relaxation rates can become competitive with radiative pumping, although this is not easy to demonstrate beyond the weak vibronic coupling limit originally explored by Litinskaia and co-workers [256].

Similarly, a number of nonlinear spectroscopy experiments keep surprising us by revealing polaritonic effects in photochemistry and photophysics [217, 44, 37] (and their vibrational counterparts [263, 232]) that do not seem to be understandable using optical filtering arguments. They are surprising in that they occur in ultrafast timescales, yet cannot be explained with the hereby presented framework of classical optics, so they must be due to single-molecule $\mathscr{O}(g)$ light-matter couplings. The puzzle is: why are they manifesting in ultrafast timescales?

5.5.2 Few molecule strong coupling

In scenarios where strong coupling is achieved with small N, higher-order correlations that go as $\mathscr{O}(N^{-1/2})$ can no longer be disregarded (see Section 5.2.1), rendering effects which go beyond the linear optics and optical filtering perspective laid out here. From a dynamics viewpoint, this means that the $\mathscr{O}(g)$ processes are no longer considered to be slow, and thus need to be taken into account in the short-time dynamics. Promising environments for this regime are plasmonic nano- and picocavites, where the small mode volumes allow for strong coupling with a single or few molecules [264, 265, 266, 267], as well as specialized optical setups that do not require such tiny mode volumes [268, 269].

5.5.3 Large number of excitations

The model presented in Sec 5.2 only considers the first excitation manifold, *i.e.* $N_{ex}/N \to 0$, where N_{ex} is the number of excitations per cavity mode. In this limit it is highly unlikely for a single molecule to be excited more than once. This is based on the assumption that the

probe laser is of low intensity, as is the internal (circulating) field of the cavity. If either of these conditions is violated, two interesting situations may occur: (1) higher-order molecular susceptibilities, *i.e.* $\chi^{(i>1)}(\omega)$, become important and (2) phenomena that were of $\mathscr{O}(1/N)$ in the first excitation manifold can now be magnified. An example of this is the radiative pumping rate into an exciton-polariton condensate. The radiative decay is filtered by the polaritons and stimulated by the number of excitations [270, 218, 49], whose rate now becomes of $\mathscr{O}(N_{exc}/N)$. Notably, in the limit of $N_{exc} \sim N$, photoluminescence can be faster than the dephasing rate and the dynamics can no longer be separated into fast and slow components.

5.6 Conclusion and outlook

This perspective explores the linear optical behavior of molecular polaritons within the collective regime, focusing on the implications of the large N limit. It is established that in this limit, the molecular absorption inside a cavity solely depends on the overlap between the polariton linear transmission and the bare molecular absorption spectrum. This re-evaluation of multiple observations in the molecular polaritonics field suggests that as $N \to \infty$, polaritons fundamentally function as optical filters, selectively allowing certain frequencies to enter the cavity and be absorbed by the molecules. Through the examples presented, it is demonstrated how this linear optics perspective can straightforwardly account for various polaritonic phenomena and that similar outcomes can be replicated outside the cavity using appropriately tailored laser pulses. This finding urges caution in attributing phenomena solely to "polaritonic" effects without first thoroughly excluding the possibility of optical filtering.

This linear optical treatment of polaritons is *exact* in the asymptotic limit of $N \to \infty$ and remains accurate for short times when N is large. However, it breaks down at long times, especially as the role of $\mathscr{O}(g)$ processes becomes significant. Similarly, in systems under strong coupling with a small number of molecules or with many excitations, the slow relaxation from dark states to polariton begins to coincide with the short-time dynamics, further

limiting the scope of the linear optical perspective. Finally, there is experimental evidence for ultrafast single-molecule processes that cannot be reconciled. Thus, for both theorists and experimentalists aiming to uncover polaritonic phenomena that transcend the realm of linear optics, the focus should shift toward these regions of interest. This approach will not only expand our understanding of polaritonic effects beyond the linear regime but also pave the way for novel applications and insights into the complex interplay between light and matter under strong coupling.

Chapter 5, in full, is adapted from the materials as it appears in "Classical linear optics effects in molecular polaritonics" by K. Schwennicke, A. Koner, J. B. Pérez-Sánchez, and J. Yuen-Zhou, in preparation (2024) [69]. The dissertation author was the primary investigator and author of this paper.

Chapter 6

Conclusion

This dissertation employs novel laser protocols and strong coupling to traverse the challenges in molecular detection and modification that arise from traditionally weak light-matter couplings. Here we employ laser driving setups to generate Aharonov-Bohm phases and pseudo-magneto optical effects in molecular systems as well as a modified microwave-three wave mixing protocol to generate a topological chiroptical spectroscopic technique for sensitize and robust enantiomeric discrimination. Additionally, we demystify molecular disorder effects in molecular polaritonics, as well as other "exotic" polaritonic phenomena. We show that in many cases the polaritonic windows act as "optical" filters, implying that the same phenomena can be observed in a bare molecular system if the correct filtered (or shaped) linear optical source is employed.

First, we proposed the use of elliptically polarized light to realize a molecular exciton version of the Aharonov-Bohm effect in an isotropic ensemble of achiral homotetramers. The generation of a nontrivial Aharonov-Bohm phase results in a nonzero circular dichroism signal. This pseudo-magnetic effect is maximized when the Aharonov-Bohm phase is $\Phi = \frac{\pi}{2}, \frac{2\pi}{3}$. Unfeasible static magnetic field strengths would be required to observe such large Aharonov-Bohm phases in electronic systems of similar size to the homotetramers we studied. This work highlights the advantage of using time-varying electric fields and electric transition dipole moments in place of static magnetic fields in certain scenarios, supporting further exploration into pseudo-magneto optical effects in molecular systems.

Next, we presented a modified microwave three-wave mixing setup to realize enantioselective topological frequency conversion. We derived that the resulting chiroptical signal is proportional to the following topologically invariant Chern number: $C_L^R = -2\text{sgn}(m)\text{sgn}(\mathscr{O}^R)$. Since $\mathscr{O}^R = -\mathscr{O}^S$ for the *R*- and *S*-enantiomers, that toplogical invariant is enantiomer-dependent. Due to its topological nature, the chiroptical signal is robust to perturbative changes to the molecular structure and electric field parameters. Therefore, we propose that this technique can be used for robust and sensitive measurement of enantiomeric excess. This work is the first to show the explicit dependence of a chiroptical spectroscopic signal on a topological invariant, providing an exciting new area of interest for further conceptual connections between topological phases of matter and molecular chirality.

We then transition from classical optical sources to cavity quantum electrodynamics and strong coupling. We began by studying molecular disorder effects on the linear response of molecular polaritons. For weak disorder, compared to the collective light-matter coupling, we derived analytical expressions for the absorption, transmission, and reflection spectra for Lorentzian, Gaussian, and rectangular disorder. Notably, for rectangular disorder, we observed the emergence of two narrow side bands in the presence of strong disorder. These sharp peaks appear to arise due to the sharp edge of the rectangular distribution, but our numerical calculations show that this edge does not need to be discontinuous and therefore could be realizable in realistic systems. Additionally, we derive a novel sum rule by integrating the ratio of the polariton absorption and transmission spectra. This resulting signal is directly proportional to the square of the collective light-matter coupling and has no dependence on the strength or type of disorder. Thus, this sum rule offers a generalized method for extracting accurate collective light-matter coupling values from experiments.

Finally, we show that in the thermodynamic limit, the polariton absorption spectrum is the product of the bare molecular absorption and polariton transmission spectra. This realization led to a remarkable revelation: the polariton transmission windows act as "optical filters" that dictate what radiation frequencies enter the cavity which are then absorbed by the molecules following

their intrinsic absorption spectra. This implies that the same "polaritonic" effect can be observed outside of the cavity if the right linear optical source, *i.e.*, one whose intensity profile mimics the polariton transmission profile, is chosen. We provide non-statistical energy redistribution, changes in photoreactivity, and short-time coherent dynamics as explicit examples of this statement. This classical linear optics treatment is exact in the limit that the number of molecules and accurate for large, but finite, number of molecules at short times ($t \lesssim 1/g$). In the latter case, even at long times certain phenomena can be explained through an optical filtering lens. For example, relaxation from the incoherent dark states to the coherent polaritons through radiative pumping is proportional to the bare molecular emission into the polariton modes modulated by the photon Hopfield coefficients. Additionally, if the incoherent dynamics of the dark states is slow compared to the decay of the photon-photon correlation function, the dynamics of the dark state population can be treated adiabatically. In this scenario, the bare molecular susceptibility is replaced by an effective, time-dependent, molecular susceptibility. This observation, along with previous statements in this paragraph, demystifying why classical techniques like transfer matrix methods consistently elucidate phenomena attributed to molecular polaritonics. We do concede that this optical filter perspective breaks down for few molecule strong coupling and when there is a large number of excitations inside the cavity since in these scenarios the distinction between "short-" and "long-time" dynamics is blurred. Furthermore, our approach cannot rectify experimental observations of ultrafast relaxation from dark state to polaritons (possibly due to vibrational relaxation). Thus our work highlights that both experimental and theorist should shift their focus to these ultrafast dynamics, and the scenarios discussed prior, to uncover truly novel polaritonic phenomena that transcend the realm of classical linear optics.

Appendix A

Supplementary Information: Optical activity from the exciton Aharonov-Bohm effect: A Floquet engineering approach

A.1 Isotropic average of circular dichroism signal: Monte Carlo integration

Here we present the Monte Carlo integration method used to compute the isotropic CD spectrum, followed by a discussion on the convergence of the spectrum. To reiterate, the isotropic CD spectrum is defined in the main text in Eq. 2.19, which we rewrite as:

$$\langle S(\omega)\rangle = \frac{\langle \delta W(\omega)\rangle}{\langle W_+(\omega)\rangle + \langle W_-(\omega)\rangle} \tag{A.1}$$

where

$$\langle \delta W(\omega)\rangle = \frac{1}{8\pi^2}\int_0^{2\pi}\int_0^{2\pi}\int_0^{\pi} d\chi d\psi d\theta\, \delta W(\omega;\chi,\psi,\theta)\sin\theta \tag{A.2a}$$

$$\langle W_\pm(\omega)\rangle = \frac{1}{8\pi^2}\int_0^{2\pi}\int_0^{2\pi}\int_0^{\pi} d\chi d\psi d\theta\, W_\pm(\omega;\chi,\psi,\theta)\sin\theta. \tag{A.2b}$$

Consider the average of a function $f(x,y,z)$ over the interval $x\in[a,b], y\in[c,d], z\in[l,m]$:

$$f_{av} = \frac{1}{V}\int_a^b\int_c^d\int_l^m dxdydz f(x,y,z), \tag{A.3}$$

where $V = (b-a)(d-c)(m-l)$ is the volume that the function is integrated over. One can approximate f_{av} by randomly selecting a finite number N of points $\{(x_i, y_i, z_i)\}$ within V and then find the average of the value of $f(x_i)$:

$$f_{av} \approx \frac{1}{N} \sum_{i=1}^{N} f(x_i, y_i, z_i). \tag{A.4}$$

As N approaches infinity, the value of Eq. (A.4) approaches that of Eq. (A.3). Then the integral can be calculated as:

$$\int_a^b \int_c^d \int_l^m dxdydzf(x,y,z) = \lim_{N\to\infty} \frac{V}{N} \sum_{i=1}^{N} f(x_i, y_i, z_i). \tag{A.5}$$

For our calculations we set $f(\chi, \psi, \theta) = \delta W(\omega; \chi, \psi, \theta) \sin\theta$ and selected a finite number N points $\{(\chi_i, \psi_i, \theta_i)\}$. Using the prescription of Eq. (A.5), we can approximate Eq. (A.2a) as:

$$\langle \delta W(\omega) \rangle \approx \langle \delta W(\omega) \rangle^{(N)} = \frac{1}{8\pi^2} \frac{V}{N} \sum_{i=1}^{N} \delta W(\omega; \chi_i, \psi_i, \theta_i) \sin\theta_i, \tag{A.6}$$

where $V = 4\pi^3$. To test for optimal values of N, we computed the $\langle \delta W(\omega) \rangle$ when $\Delta\phi = \frac{\pi}{2}$ for increasing values of N (in increments of 100). We compared the new spectrum with the previous spectrum by calculating the relative error:

$$\langle \Delta^2(N) \rangle = \frac{1}{k} \sum_{i=1}^{k} \left[\langle \delta W(\omega_i) \rangle^{(N)} - \langle \delta W(\omega_i) \rangle^{(N-100)} \right]^2, \tag{A.7}$$

where $N = 100z + 10$ and z is a positive integer, k is the number of different frequencies that the CD signal was calculated at, and $\langle \delta W(\omega_i) \rangle^{(N)}$, $\langle \delta W(\omega_i) \rangle^{(N-100)}$ are the computed isotropic values at frequency ω_i using N and $N-100$ points in the Monte Carlo Integration. The quantity $\sqrt{\langle \Delta^2(N) \rangle}$ is the *L2*-norm of the difference between the two spectra.

Since the absorption spectrum is sparse, we calculated Eq. (A.7) by only sampling two different sets of frequencies ω_i, each spanning $50\,\mathrm{cm}^{-1}$, where one set was centered at

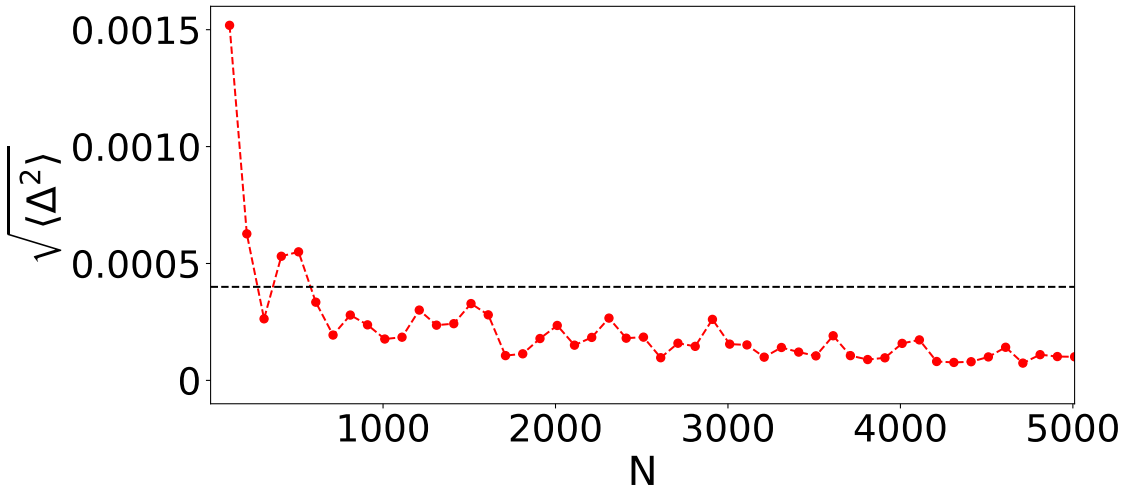

Figure A.1. *Convergence of Monte Carlo integration.* Plot of the relative error of the numerical isotopic average of the CD signal, $\sqrt{\langle\Delta^2(N)\rangle}$, as a function of N random molecular aggregate orientations. The relative error falls below the tolerance value 4×10^{-4}. Hence we choose $N = 2000$ for our calculations.

ω_E and the other at ω_F. We selected 50 distinct frequencies from each set; therefore, in our calculations $k = 100$. As seen in Fig. A.1, the calculations are already converged at $N = 2000$, when $\sqrt{\langle\Delta^2(N)\rangle} \leq 4\times10^{-4}$. We then approximate A.2b, employing the same procedure as Eq. A.6 with $N = 2000$. Finally, we then substitute the calculated values for $\langle\delta W(\omega)\rangle$ and $\langle W_{\pm}(\omega)\rangle$ into Eq. A.1 to calculate the CD spectrum presented in Fig. 2.5 in the main text.

Appendix B

Supplementary Information: Enantioselective topological frequency conversion

B.1 Rotational eigenstates

Here we present the low angular momentum eigenstates of the asymmetric top. For completeness, we reintroduce the asymmetric top Hamiltonian

$$H_0 = AJ_a^2 + BJ_b^2 + CJ_c^2, \tag{B.1}$$

where J_a, J_b, J_c are the angular momentum operators with respect to the principal axes $\hat{a}$, $\hat{b}$, $\hat{c}$, and $A > B > C$ are the corresponding rotational constants. The $B = C$ case corresponds to a prolate top with eigenstates labeled $|J,K,M\rangle$, where $J = 0,1,2...$ is the rotational quantum number and $M,K = -J,-J+1,-J+2,...,J$ are the quantum numbers that characterize the projection of the total angular momentum along the a-principal axis and z-laboratory-fixed axis. The eigenstates of the asymmetric top Hamiltonian can be expressed as superpositions of the prolate top eigenstates as follows:

$$|J,\tau,M\rangle = \sum_K A_K^{J,M}(\tau)|J,K,M\rangle. \tag{B.2}$$

Note that the quantum numbers J, M are conserved by H_0, and τ serves as the quantum number to differentiate between states with the same J and M. The eigenstates of Eq. B.1 with a rotational

quantum number of $J = 0$ or $J = 1$ are

$$
\begin{aligned}
|0, \tau = 1, 0\rangle &\equiv |0, K = 0, 0\rangle, \\
|1, \tau = 1, M\rangle &\equiv |1, K = 0, M\rangle, \\
|1, \tau = 2, M\rangle &\equiv \frac{1}{\sqrt{2}}|1, K = 1, M\rangle - \frac{1}{\sqrt{2}}|1, K = -1, M\rangle, \\
|1, \tau = 3, M\rangle &\equiv \frac{1}{\sqrt{2}}|1, K = 1, M\rangle + \frac{1}{\sqrt{2}}|1, K = -1, M\rangle,
\end{aligned} \tag{B.3}
$$

where $M = -1, 0, 1$ [165]. In the main text, we do not couple the states $|1, \tau = 1, M\rangle$ to others, and thus ignore them.

B.2 Change of basis

We present the necessary change of basis to obtain the effective Hamiltonian presented in Eq. 3.8 in the main text. We first introduce $|2, B\rangle = \frac{1}{\sqrt{2}}(|2, 1\rangle + |2, -1\rangle)$ and $|2, D\rangle = \frac{1}{\sqrt{2}}(|2, 1\rangle - |2, -1\rangle)$, which we refer to as the "bright" and "dark" state respectively. It is easy to see that bright state couples to $|1, 0\rangle$ and $|3, 0\rangle$, while the dark state is uncoupled (see Eq. 7). Ignoring the dark state, the Hamiltonian in the rotating frame becomes

$$
\mathscr{H}^{R,S}(t) = \frac{1}{2}\begin{pmatrix}
-2\hbar\delta & -\frac{\mu_b^{R,S}}{\sqrt{3}}\mathscr{E}_{21}(t) & -\frac{i\mu_c^{R,S}}{\sqrt{3}}\mathscr{E}_{31}(t) \\
-\frac{\mu_b^{R,S}}{\sqrt{3}}\mathscr{E}_{21}(t) & 0 & -\frac{\mu_a^{R,S}}{2}\mathscr{E}_{32}(t) \\
\frac{i\mu_c^{R,S}}{\sqrt{3}}\mathscr{E}_{31}(t) & -\frac{\mu_a^{R,S}}{2}\mathscr{E}_{32}(t) & 2\hbar\delta
\end{pmatrix} \tag{B.4}
$$

In the complex basis $|+\Pi\rangle, |0\rangle, |-\Pi\rangle$, where $—\pm\Pi\rangle = \frac{1}{\sqrt{2}}(|1, 0\rangle \pm i|3, 0\rangle)$ and $|0\rangle = |2, B\rangle$, Eq. B.4 becomes

$$
\begin{aligned}
\mathscr{H}^{R,S}(t) = &-\frac{\mu_b^{R,S}\mathscr{E}_{21}(t)}{2\sqrt{3}\hbar}L_x - \frac{\mu_a^{R,S}\mathscr{E}_{32}(t)}{4\hbar}L_y \\
&+ \frac{\mu_c^{R,S}\mathscr{E}_{31}(t)}{2\sqrt{3}\hbar}L_z - \frac{\delta}{2\hbar}(L_+^2 + L_-^2)
\end{aligned} \tag{B.5}
$$

where $L_x = \frac{\hbar}{\sqrt{2}}\begin{pmatrix} 0 & 1 & 0 \\ 1 & 0 & 1 \\ 0 & 1 & 0 \end{pmatrix}$, $L_y = \frac{\hbar}{\sqrt{2}}\begin{pmatrix} 0 & -i & 0 \\ i & 0 & -i \\ 0 & i & 0 \end{pmatrix}$, $L_z = \hbar\begin{pmatrix} 1 & 0 & 0 \\ 0 & 0 & 0 \\ 0 & 0 & -1 \end{pmatrix}$ are the angular momentum operators for a spin-1 particle and $L_+ = \hbar\sqrt{2}\begin{pmatrix} 0 & 1 & 0 \\ 0 & 0 & 1 \\ 0 & 0 & 0 \end{pmatrix}$, $L_- = \hbar\sqrt{2}\begin{pmatrix} 0 & 0 & 0 \\ 1 & 0 & 0 \\ 0 & 1 & 0 \end{pmatrix}$ are the corresponding ladder operators. Eq. B.5 is the effective Hamiltonian used to study the topology of the system presented in the main text.

B.3 Adiabatic perturbation theory

For completeness, we briefly review adiabatic perturbation theory. Let

$$|\tilde{\psi}(t)\rangle = \sum_l \tilde{c}_l(t)|\varepsilon_l(t)\rangle \tag{B.6}$$

be the solution of the time-dependent Schrödinger equation (TDSE) $i\hbar\partial_t|\tilde{\psi}(t)\rangle = \mathscr{H}(t)|\tilde{\psi}(t)\rangle$, where $\{|\varepsilon_l(t)\rangle\}$ are the adiabatic eigenstates satisfying $\mathscr{H}(t)|\varepsilon_l(t)\rangle = \varepsilon_l(t)|\varepsilon_l(t)\rangle$. Employing the TDSE, the following differential equation is obtained for $\tilde{c}_l(t)$,

$$i\hbar\partial_t\tilde{c}_l(t) = \varepsilon_l(t)\tilde{c}_l(t) - i\hbar\sum_{l'}\langle\varepsilon_l(t)|\omega\cdot\nabla_{\omega t}|\varepsilon_{l'}(t)\rangle\tilde{c}_{l'}(t), \tag{B.7}$$

where $\omega = (\omega_1, \omega_2)$. Ignoring non-adiabatic terms in Eq. B.7 for $l' \neq l$,

$$\tilde{c}_l(t) \approx \tilde{c}_l(0)e^{-i\int_0^t dt'[\varepsilon_l(t') - i\hbar\langle\varepsilon_l(t')|\omega\cdot\nabla_{\omega t}|\varepsilon_l(t'))]/\hbar}. \tag{B.8}$$

Hereafter, we assume that the system is initialized in the $l-$th adiabatic state $|\tilde{\psi}(0)\rangle = |\varepsilon_l(0)\rangle$. Eq. B.8 is a statement of the adiabatic theorem and implies that the system shall remain in the $l-$th adiabatic state, $|\tilde{\psi}(t)\rangle \approx$ (phase factor) $\times\, |\varepsilon_l(t)\rangle$.

However, we are interested in $O(\hbar\omega)$ non-adiabatic corrections to Eq. B.8. We rewrite $\tilde{c}_{l'} = \hbar\omega\tilde{c}_l(t)a_{l'}(t)$ for $l' \neq l$,

$$|\tilde{\psi}(t)\rangle = \tilde{c}_l(t)[|\varepsilon_l(t)\rangle + \sum_{l'\neq l}\hbar\omega a_{l'}(t)|\varepsilon_{l'}(t)\rangle], \tag{B.9}$$

and insert this ansatz into Eq. B.7,

$$\varepsilon_l(t)\tilde{c}_l(t)a_{l'}(t)\hbar\omega + O(\hbar^2\omega^2) = \hbar\omega\varepsilon_{l'}(t)\tilde{c}_l(t)a_{l'}(t) - i\hbar\langle\varepsilon_{l'}(t)|\omega\cdot\nabla_{\omega t}|\varepsilon_l(t)\rangle\tilde{c}_l(t) + O(\hbar^2\omega^2), \tag{B.10}$$

where we used $\partial_t a_{l'}(t) = \hbar\omega\cdot\nabla_{\omega t}a_{l'}(t)$. Solving for $a_{l'}(t)$, the $O(\hbar\omega)$ wavefunction is,

$$|\tilde{\psi}(t)\rangle = \tilde{c}_l(t)\left[|\varepsilon_l(t)\rangle - i\hbar\sum_{l'\neq l}\frac{|\varepsilon_{l'}(t)\rangle\langle\varepsilon_{l'}(t)|\omega\cdot\nabla_{\omega t}|\varepsilon_l(t)\rangle}{\varepsilon_l(t)-\varepsilon_{l'}(t)}\right]. \tag{B.11}$$

B.4 Deriving Eq. 3.12a and 3.12b

Here, $\langle\tilde{\psi}(t)|\partial_{\omega_i t}\mathscr{H}(t)|\tilde{\psi}(t)\rangle$ is derived when the system is initiated in the adiabatic state $|\varepsilon_l(0)\rangle$ and evolved near the adiabatic limit. Employing Eq. B.11 for $|\tilde{\psi}(t)\rangle$, and making the change of variables $(\omega_1 t, \omega_2 t) = (\theta_1, \theta_2)$, the following expression to $O(\hbar\omega)$ is obtained:

$$\begin{aligned}
\langle\tilde{\psi}(t)|\nabla_{\omega t}\mathscr{H}(t)|\tilde{\psi}(t)\rangle &= \langle\varepsilon_l(\theta)|\nabla_\theta\mathscr{H}(\theta)|\varepsilon_l(\theta)\rangle \\
&\quad - \left\{i\hbar\sum_{l'\neq l}\frac{\langle\varepsilon_l(\theta)|\nabla_\theta\mathscr{H}(\theta)|\varepsilon_{l'}(\theta)\rangle\langle\varepsilon_{l'}(\theta)|\omega\cdot\nabla_\theta|\varepsilon_l(\theta)\rangle}{\varepsilon_l(\theta)-\varepsilon_{l'}(\theta)} + \text{h.c}\right\} \\
&= \nabla_\theta\varepsilon_l(\theta) - \left\{i\hbar\langle\nabla_\theta\varepsilon_l(\theta)|\omega\cdot\nabla_\theta|\varepsilon_l(\theta)\rangle + \text{h.c}]\right\} \\
&= \nabla_\theta\varepsilon_l(\theta) - \hbar\omega\times\hat{v}_\perp F_l(\theta),
\end{aligned} \tag{B.12}$$

where $\omega \times \hat{v}_\perp = (\omega_2, -\omega_1)$ and $F_l(\theta) = i\langle \partial_{\theta_1} \varepsilon_l(\theta) | \partial_{\theta_2} \varepsilon_l(\theta) \rangle + \text{h.c.}$ is the Berry curvature of the $l-$th band.

B.5 Analytical evaluation of Chern numbers

Here, we analytically compute the Chern numbers for the bands of the system in the main text when $\delta = 0$. We follow the procedure described in [271]. We first consider the three-level Hamiltonian:

$$\mathscr{H}(\theta) = \sum_{s=\pm 1} s h_3(\theta) |s\rangle\langle s| + \Big\{ [h_1(\theta) - i s h_2(\theta)] |s\rangle\langle 0| + \text{h.c.} \Big\}, \tag{B.13}$$

where $h_1(\theta)$, $h_2(\theta)$, $h_3(\theta)$ are real valued. Next, we invoke the unitary transformation $U(\theta) = \sum_{s=0,\pm 1} e^{is\alpha(\theta)} |s\rangle\langle s|$, such that $\tan \alpha(\theta) = h_2(\theta)/h_1(\theta)$, to define the real-valued Hamiltonian,

$$\begin{aligned} \mathscr{H}'(\theta) &= U(\theta) \mathscr{H}(\theta) U^\dagger(\theta) \\ &= \sum_{s=\pm 1} s h_3(\theta) |s\rangle\langle s| + \sqrt{h_1^2(\theta) + h_2^2(\theta)} (|s\rangle\langle 0| + \text{h.c.}). \end{aligned} \tag{B.14}$$

A set of eigenstates for $\mathscr{H}'(\theta)$ can be defined as $|\varepsilon'_l(\theta)\rangle = \sum_{s=0,\pm 1} c_{l,s}(\theta) |s\rangle$, where the coefficients $c_{l,s}(\theta)$ are real. The eigenstates of $\mathscr{H}(\theta)$ are

$$|\varepsilon_l(\theta)\rangle = U^\dagger(\theta) |\varepsilon'_l(\theta)\rangle = \sum_{s=0,\pm 1} c_{l,s}(\theta) e^{-is\alpha(\theta)} |s\rangle. \tag{B.15}$$

The Berry connection for the $l-$th band is

$$\begin{aligned} A_l(\theta) &= i\langle \varepsilon_l(\theta) | \nabla_\theta | \varepsilon_l(\theta) \rangle \\ &= \nabla_\theta \alpha(\theta) \sum_{s=\pm 1} s c_{l,s}^2(\theta), \end{aligned} \tag{B.16}$$

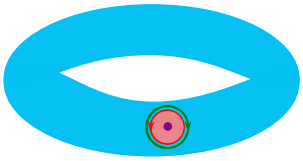

Figure B.1. *Contour integration procedure to evaluate Chern number* $C_l^{R,S}$. The closed curve ∂_r bounds both the pink region, which contains the singularity of $A_l^{R,S}(\theta)$, and the blue region, which is rest of the torus. To apply Stokes theorem, we integrate counter-clockwise (red curve) along ∂_r to find the surface integral for the pink region, and clockwise along ∂_R (green curve) to find the surface integral for the blue region. The procedure can be extended to an arbitrary number of singularities of $A_l^{R,S}(\theta)$.

where we used the fact that $\sum_{s=0,\pm1} c_{l,s}(\theta)\nabla_\theta c_{l,s}(\theta) = \frac{1}{2}\nabla_\theta \sum_{s=0,\pm1} |c_{l,s}|^2 = 0$. The Berry curvature is defined as the z-component of the curl of the Berry connection, *i.e.*, $F_l(\theta) = (\nabla_\theta \times A_l(\theta)) \cdot \hat{z}$. Note that there are singularities in the Berry connection when $\nabla_\theta \alpha(\theta) = \frac{h_1(\theta)\nabla_\theta h_2(\theta) - h_2(\theta)\nabla_\theta h_1(\theta)}{h_1^2(\theta)+h_2^2(\theta)}$ is undefined; they occur at the critical points where $h_1(\theta) = h_2(\theta) = 0$.

Considering Eqs. 3.8 and 3.9 from the main text and taking $\delta = 0$, the values $h_1^{R,S}(\theta)$, $h_2^{R,S}(\theta)$, $h_3^{R,S}(\theta)$ are

$$
\begin{aligned}
h_1^{R,S}(\theta) &= -\frac{\mu_b^{R,S} E_{21} \sin(\theta_1)}{4\hbar\sqrt{6}}, \\
h_2^{R,S}(\theta) &= -\frac{\mu_a^{R,S} E_{32} \sin(\theta_2)}{5\hbar\sqrt{2}}, \\
h_3^{R,S}(\theta) &= \frac{\mu_c^{R,S}}{2\hbar\sqrt{3}} E_{31}[m - \cos(\theta_1) - \cos(\theta_2)],
\end{aligned}
\tag{B.17}
$$

and the aforementioned singularities occur at the $\theta = (\theta_1, \theta_2)$ values $\theta_{00} = (0,0)$, $\theta_{0\pi} = (0,\pi)$, $\theta_{\pi 0} = (\pi,0)$, and $\theta_{\pi\pi} = (\pi,\pi)$. Physically, these critical points indicate geometric conditions where certain components of light-matter coupling vanish.

The Chern number for the $R-$ and $S-$ enantiomer is proportional to the surface integral

of the corresponding Berry curvature over the torus $\mathbb{T}$,

$$C_l^{R,S} = \frac{1}{2\pi} \int_{\mathbb{T}} d\theta F_l^{R,S}(\theta). \tag{B.18}$$

Using Stokes theorem, it can be written as a contour integral of the Berry connection; however, the singularities must be removed. To motivate the general procedure, first consider the case where the Berry connection $A_l^{R,S}(\theta)$ contains only one singularity. The curve ∂_r can be drawn, such that it defines an infinitesimal region containing the singularity (region I) and the rest of the torus (region II) (see Fig. B.1). Applying a gauge transformation $|\varepsilon_l^{R,S}(\theta)\rangle \to e^{i\phi_l^{R,S}(\theta)}|\varepsilon_l^{R,S}(\theta)\rangle$ in region I can remove the singularity, $A_l^{R,S}(\theta) \to A_l'^{R,S}(\theta) = A_l^{R,S}(\theta) - \nabla_\theta \phi_l^{R,S}(\theta)$, while the Berry curvature is unaffected [272, 271]. Taking $\nabla_\theta \phi_l^{R,S}(\theta) = A_l^{R,S}(\theta)$ achieves this desired result. The Chern numbers can then be written as the summation of contour integrals for each region:

$$\begin{aligned}
C_l^{R,S} &= \frac{1}{2\pi} \int_{\mathbb{T}} d\theta F_l^{R,S}(\theta) \\
&= \frac{1}{2\pi} \oint_{\partial_r} d\theta \cdot A_l'^{R,S}(\theta) - \frac{1}{2\pi} \oint_{\partial_R} d\theta \cdot A_l^{R,S}(\theta) \\
&= \frac{1}{2\pi} \oint_{\partial_r} d\theta \cdot [A^{R,S}{}_l(\theta) - \nabla_\theta \phi_l^{R,S}(\theta)] - \frac{1}{2\pi} \oint_{\partial_R} d\theta \cdot A_l^{R,S}(\theta) \\
&= -\frac{1}{2\pi} \oint_{\partial_r} d\theta \cdot \nabla_\theta \phi_l^{R,S}(\theta) \\
&= -\frac{1}{2\pi} \oint_{\partial_r} d\theta \cdot A_l^{R,S}(\theta).
\end{aligned} \tag{B.19}$$

In going from the first to the second line, we applied Stokes' theorem in region I by traversing ∂_r in a counterclockwise fashion, and in region II by doing so in a clockwise way (see Fig. B.1).

If the Berry connection $A_l^{R,S}(\theta)$ contains multiple singularities θ_{ij}, then local gauge transformations must be carried out in multiple regions to remove all of them. Then the Chern

number results in

$$C_l^{R,S} = -\sum_{ij} \frac{1}{2\pi} \oint_{\partial_{r_{ij}}} d\theta \cdot A_l^{R,S}(\theta) \tag{B.20}$$

where the curves $\{\partial_{r_{ij}}\}$ enclose an infinitesimal region around each of the singularities θ_{ij}. Therefore, the Chern number can be calculated by studying the behavior of $A_l^{R,S}(\theta)$ near the singularities.

Let $q = (q_1, q_2)$ be a small displacement from the point θ_{ij}. Since $\sin(x) \approx x$ and $\sin(\pi + x) \approx -x$ as $x \to 0$, then

$$\begin{aligned}
\alpha^{R,S}(\theta_{00} + q) &\approx \beta^{R,S}, \\
\alpha^{R,S}(\theta_{0\pi} + q) &\approx -\beta^{R,S}, \\
\alpha^{R,S}(\theta_{\pi 0} + q) &\approx -\beta^{R,S}, \\
\alpha^{R,S}(\theta_{\pi\pi} + q) &\approx \beta^{R,S},
\end{aligned} \tag{B.21}$$

where $\tan\beta^{R,S} = \frac{4\sqrt{3}\mu_a^{R,S}E_{32}q_2}{5\mu_b^{R,S}E_{21}q_1}$. The gradients $\nabla_q \alpha^{R,S}(\theta)$ near the critical points can be readily evaluated in polar coordinates, $|q|e^{i\gamma} = q_1 + iq_2$,

$$\begin{aligned}
\nabla_q \alpha^{R,S}(\theta_{00} + q) &= -\nabla_q \alpha^{R,S}(\theta_{\pi 0} + q) \\
&= -\nabla_q \alpha^{R,S}(\theta_{0\pi} + q) \\
&= \nabla_q \alpha^{R,S}(\theta_{\pi\pi} + q) \\
&\approx \frac{1}{|q|} \frac{(4\sqrt{3}\mu_a^{R,S}E_{32})(5\mu_b^{R,S}E_{21})}{(4\sqrt{3}\mu_a^{R,S}E_{32})^2 \sin^2\gamma + (5\mu_b^{R,S}E_{21})^2 \cos^2\gamma} \hat{\gamma}.
\end{aligned} \tag{B.22}$$

The line integral of $\nabla_q \alpha^{R,S}(\theta_{00} + q)$ over a small circle in the limit when $|q| \to 0$,

$$
\begin{aligned}
&\oint_{|q|\to 0} dq\cdot\nabla_q \alpha^{R,S}(\theta_{00}+q)\\
=&\Big(\int_0^{\pi/2^-} d\gamma+\int_{\pi/2^+}^{3\pi/2^-} d\gamma\\
&+\int_{3\pi/2^+}^{2\pi} d\gamma\Big)\frac{(4\sqrt{3}\mu_a^{R,S}E_{32})(5\mu_b^{R,S}E_{21})}{(4\sqrt{3}\mu_a^{R,S}E_{32})^2\sin^2\gamma+(5\mu_b^{R,S}E_{21})^2\cos^2\gamma}\\
=&\Big(\int_0^{\mathrm{sgn}[(\mu_a^{R,S}E_{32})(\mu_b^{R,S}E_{21})]\infty} dx+\int_{-\mathrm{sgn}[(\mu_a^{R,S}E_{32})(\mu_b^{R,S}E_{21})]\infty}^{\mathrm{sgn}[(\mu_a^{R,S}E_{32})(\mu_b^{R,S}E_{21})]\infty} dx\\
&+\int_{-\mathrm{sgn}[(\mu_a^{R,S}E_{32})(\mu_b^{R,S}E_{21})]\infty}^{0} dx\Big)\frac{1}{1+x^2}\\
=&2\pi\mathrm{sgn}[(\mu_a^{R,S}E_{32})(\mu_b^{R,S}E_{21})].
\end{aligned}
\tag{B.23}
$$

In the second line, we split the integral into three parts, noticing that the integral in the remaining infinitesimal regions around $\gamma=\pi/2$ and $\gamma=3\pi/2$ vanish given that the integrand is finite, $\int_{\pi/2^-}^{\pi/2^+} d\gamma(\cdot)=\int_{3\pi/2^-}^{3\pi/2^+} d\gamma(\cdot)=0$. In the third line, we let $x=\frac{4\sqrt{3}\mu_a^{R,S}E_{32}}{5\mu_b^{R,S}E_{21}}\tan\gamma$, and $dx=\frac{4\sqrt{3}\mu_a^{R,S}E_{32}}{5\mu_b^{R,S}E_{21}}\sec^2\gamma d\gamma$ and recognized that $x\to\mathrm{sgn}[(\mu_a^{R,S}E_{32})(\mu_b^{R,S}E_{21})]\infty$ as $\gamma\to(\pi/2)^-,(3\pi/2)^-$ and $x\to-\mathrm{sgn}[(\mu_a^{R,S}E_{32})(\mu_b^{R,S}E_{21})]\infty$ as $\gamma\to(\pi/2)^+,(3\pi/2)^+$.

The procedure of Eqs. (B.22) and (B.23) can be repeated for the other critical points, yielding,

$$
\begin{aligned}
\oint_{|q|\to 0} dq\nabla_q\alpha^{R,S}(\theta_{0\pi}+q)&=-2\pi\mathrm{sgn}[(\mu_a^{R,S}E_{32})(\mu_b^{R,S}E_{21})],\\
\oint_{|q|\to 0} dq\nabla_q\alpha^{R,S}(\theta_{\pi 0}+q)&=-2\pi\mathrm{sgn}[(\mu_a^{R,S}E_{32})(\mu_b^{R,S}E_{21})],\\
\oint_{|q|\to 0} dq\nabla_q\alpha^{R,S}(\theta_{\pi\pi}+q)&=2\pi\mathrm{sgn}[(\mu_a^{R,S}E_{32})(\mu_b^{R,S}E_{21})].
\end{aligned}
\tag{B.24}
$$

Using Eqs. B.16 and B.20, the Chern number for the l-th band is

Table B.1. *Example Chern number calculation.* Shown are the values of the $|s=\pm 1\rangle$ amplitudes $|c_{U,s}^{R,S}(\theta_{00})|^2$ for the upper band eigenstate at the singularity points θ_{ij} for $|m|<2$. Using these values and Eq. B.25, we find that $C_U^{R,S} = 2\text{sgn}[m(\mu_a^{R,S}E_{32})(\mu_b^{R,S}E_{21})(\mu_c^{R,S}E_{31})]$.

	$\lvert c_{U,s}^{R,S}(\theta_{00})\rvert^2$	$\lvert c_{U,s}^{R,S}(\theta_{0\pi})\rvert^2$	$\lvert c_{U,s}^{R,S}(\theta_{\pi 0})\rvert^2$	$\lvert c_{U,s}^{R,S}(\theta_{\pi\pi})\rvert^2$
$s=1$	$\frac{1}{2}-\frac{1}{2}\text{sgn}[(\mu_c^{R,S}E_{31})]$	$\frac{1}{2}+\frac{1}{2}\text{sgn}[m(\mu_c^{R,S}E_{31})]$	$\frac{1}{2}+\frac{1}{2}\text{sgn}[m(\mu_c^{R,S}E_{31})]$	$\frac{1}{2}+\frac{1}{2}\text{sgn}[(\mu_c^{R,S}E_{31})]$
$s=-1$	$\frac{1}{2}+\frac{1}{2}\text{sgn}[(\mu_c^{R,S}E_{31})]$	$\frac{1}{2}-\frac{1}{2}\text{sgn}[m(\mu_c^{R,S}E_{31})]$	$\frac{1}{2}-\frac{1}{2}\text{sgn}[m(\mu_c^{R,S}E_{31})]$	$\frac{1}{2}-\frac{1}{2}\text{sgn}[(\mu_c^{R,S}E_{31})]$

$$\begin{aligned} C_l^{R,S} &= -\sum_{ij}\frac{1}{2\pi}\oint_{\partial_{r_{ij}}} d\theta\cdot A_l^{R,S}(\theta) \\ &= -\text{sgn}[(\mu_a^{R,S}E_{21})(\mu_b^{R,S}E_{32})]\sum_{s=\pm 1} s[|c_{l,s}^{R,S}(\theta_{00})|^2 \\ &\quad -|c_{l,s}^{R,S}(\theta_{0\pi})|^2-|c_{l,s}^{R,S}(\theta_{\pi 0})|^2+|c_{l,s}^{R,S}(\theta_{\pi\pi})|^2] \end{aligned} \tag{B.25}$$

For $|m|<2$ the Chern numbers for the upper, middle, and lower adiabatic states can be seen to yield,

$$\begin{aligned} C_U^{R,S} &= 2\text{sgn}[m(\mu_a^{R,S}E_{32})(\mu_b^{R,S}E_{21})(\mu_c^{R,S}E_{31})], \\ C_M^{R,S} &= 0, \\ C_L^{R,S} &= -2\text{sgn}[m(\mu_a^{R,S}E_{32})(\mu_b^{R,S}E_{21})(\mu_c^{R,S}E_{31})]. \end{aligned} \tag{B.26}$$

For $|m|>2$, all $C_l^{R,S}=0$. For the benefit of the reader, Table B.1 provides an example calculation of the upper band Chern number $C_U^{R,S}$ for $|m|<2$.

B.6 Laser shot-noise

The laser shot noise is defined as the width of the photon distribution of the driving field. In the main text, the laser field strength is assumed to be approximately $E=10^{-9}$ a.u., or $500\,\frac{\text{V}}{\text{m}}$.

Assuming that the laser-beam waist area is $A = 1\text{cm}^2$, its power is given by,

$$\begin{aligned} P &= \frac{cA\varepsilon_0 E^2}{8\pi} \\ &= \frac{3\times 10^8 \frac{\text{m}}{\text{s}} \times 1\,\text{cm}^2 \times \frac{1\text{m}^2}{100^2\text{cm}^2} \times 8.85\times 10^{-12}\frac{\text{C}^2}{\text{J}\cdot\text{m}} \times (500\frac{\text{V}}{\text{m}})^2}{8\pi} \\ &= 3\,\text{mW} \end{aligned} \tag{B.27}$$

where c is the speed of light and ε_0 is the permittivity of free space. The frequencies of the molecular transitions in the main text are on the order of $v = 10\,\text{GHz}$. Then the expected number of photons produced by the laser after a long enough time $t^* = 2000\times 2\pi/\omega_2$ which guarantees TFC is

$$N = \frac{Pt^*}{hv} = \frac{3\times 10^{-3}\text{W}\times 8\times 10^{-3}\text{s}}{6.63\times 10^{-34}\text{J}\cdot\text{s}\times 10\times 10^9\text{s}^{-1}} = 4\times 10^{18} \tag{B.28}$$

The photon distribution is taken to be Poissonian. The standard deviation of this distribution is $\sqrt{N}$, so the laser shot noise is $\sqrt{N}\sim 10^9$.

Appendix C

Supplementary Information: Extracting accurate light-matter coupling from disordered polaritons

C.1 Sum rule for finite temperature

From Eqs. 4.2 and 5.5b, we have that

$$I = \int d\omega \frac{A(\omega)}{T(\omega)} = \frac{\omega_{ph}}{\kappa_R} \int d\omega \chi''(\omega) \tag{C.1}$$

From Eq. 4.5, for N two-level systems coupled to a single cavity mode at a given temperature T, Eq. C.1 becomes:

$$\begin{aligned} I = \frac{i}{\kappa_R} \lim_{\gamma \to 0^+} \sum_{i=1}^{N} \tanh\left(\frac{\hbar\omega_{ex,i}}{2k_B T}\right) |\lambda \mu_i|^2 \\ \times \int d\omega \Big[\frac{1}{\omega - \omega_{ex,i} + i\frac{\gamma}{2}} - \frac{1}{\omega - \omega_{ex,i} - i\frac{\gamma}{2}} \Big] \end{aligned} \tag{C.2}$$

Note that if we evaluate the integral counterclockwise over a semicircle S_+ with an infinite radius in the upper half of the complex plane, we have that

$$\begin{aligned} 0 &= \oint_{S_+} d\omega \Big[\frac{1}{\omega - \omega_{ex,i} + i\frac{\gamma}{2}}\Big] \\ &= \int d\omega \Big[\frac{1}{\omega - \omega_{ex,i} + i\frac{\gamma}{2}}\Big] + i\pi \end{aligned} \tag{C.3a}$$

$$\begin{aligned} i2\pi &= \oint_{S_+} d\omega \Big[\frac{1}{\omega - \omega_{ex,i} - i\frac{\gamma}{2}}\Big] \\ &= \int d\omega \Big[\frac{1}{\omega - \omega_{ex,i} - i\frac{\gamma}{2}}\Big] + i\pi \end{aligned} \tag{C.3b}$$

This implies that $\int d\omega \Big[\frac{1}{\omega-\omega_{ex,i}+i\frac{\gamma}{2}}\Big] = -i\pi$ and $\int d\omega \Big[\frac{1}{\omega-\omega_{ex,i}-i\frac{\gamma}{2}}\Big] = i\pi$. Substituting these values into Eq. C.2, we arrive at the generalized sum rule for arbitrary T:

$$I = \frac{2\pi}{\kappa_R} \sum_{i=1}^{N} \tanh\Big(\frac{\hbar\omega_{ex,i}}{2k_BT}\Big) |\lambda\mu_i|^2 = \frac{2\pi}{\kappa_R} N g_{eff}^2 \tag{C.4}$$

where

$$g_{eff}^2 = \int d\omega_{ex} p(\omega_{ex}) \tanh\Big(\frac{\hbar\omega_{ex}}{2k_BT}\Big) |\lambda\mu(\omega_{ex})|^2 \tag{C.5}$$

is the square of the effective single-molecule light-matter coupling. Here $p(\omega_{ex})$ is the probability distribution of excitation frequencies. Note in the limit that $\hbar\omega_{ex,i} \gg k_BT$ and $\mu(\omega_{ex}) \to \mu$, we have that $g_{eff}^2 \to g^2$, recovering the version of the sum rule presented in the main text.

Appendix D

Supplementary Information: Classical linear optics effects in molecular polaritonics

D.1 Estimating number of molecules per cavity mode

For a one-dimensional cavity of length L_z, the dispersion for the $m-$th transversal mode is:

$$\omega = \frac{c}{\sqrt{\varepsilon}}\sqrt{|\vec{k}_{\parallel}|^2 + \left(\frac{m\pi}{L_z}\right)^2}, \tag{D.1}$$

where $\vec{k}_{\parallel}$ is the component of the wave vector parallel to the plane of the cavity mirrors, c is the speed of light, and ε is the background permittivity. Assuming periodic boundary conditions parallel to the mirrors, the wave vector values are discrete points in a reciprocal lattice with grid spacing $\Delta_{k_{x,y}} = \frac{2\pi}{L_{x,y}}$, where L_x and L_y refer to the height and width of the cavity mirrors. The protocol is to define an area in this reciprocal lattice and then divide by the area unit of the grid ($\Delta_{k_x}\Delta_{k_y}$) to calculate the number of cavity modes N_{modes} within this area of interest. Next the total number of molecules N_{mol} within the cavity is calculated, and finally, the number of molecules per cavity modes is estimated as $N = N_{mol}/N_{modes}$.

D.1.1 Electronic strong coupling

Here we estimate N for electronic strong coupling following the protocol of Ref. [236]. The authors consider a square in reciprocal space of length $|\vec{k}_{max}| = \frac{2\pi}{\lambda}$, where λ is a characteristic

wavelength associated with UV-visible organic exciton-polaritons (~ 500 nm). Assuming a one-dimensional cavity, the total number of cavity modes is:

$$\begin{aligned} N_{modes} &= 2 \times \frac{|\vec{k}_{max}|^2}{\Delta_{k_x}\Delta_{k_y}} \\ &= L_x L_y \frac{2}{\lambda^2} \end{aligned} \tag{D.2}$$

where the factor of two accounts for the fact that for each k there are two polarizations. The number of molecules in the cavity is given by

$$N_{mol} = \rho L_x L_y L_z, \tag{D.3}$$

where ρ is the molecule number density. Then the number of molecules per mode is:

$$N = \frac{N_{mol}}{N_{modes}} = \frac{\rho L_z \lambda^2}{2}. \tag{D.4}$$

Taking $\rho = 10^9\ \mu\text{m}^{-3}$ and $L_z = 100$ nm from Ref. [236], we estimate the number of molecules per mode for electronic strong coupling to be $N \sim 1.25 \times 10^7$ as reported in the main text.

D.1.2 Vibrational strong coupling

Here we estimate N following the protocol of Ref. [237]. From Eq. D.1, the magnitude of the parallel wave vector component for $m = 1$ is:

$$|\vec{k}_{\parallel}| = \sqrt{\frac{\varepsilon\omega^2}{c^2} - \left(\frac{\pi}{L_z}\right)^2}. \tag{D.5}$$

Considering a circle in reciprocal space of radius $|\vec{k}_{max}|$, the number of photon cavity modes is

$$\begin{aligned} N_{modes} &= \frac{\pi |k_{\parallel,max}|^2}{\Delta_{k_x}\Delta_{k_y}} \\ &= \frac{\pi\left[\frac{\varepsilon\omega_{max}^2}{c^2} - \left(\frac{\pi}{L_z}\right)^2\right]}{\Delta_{k_x}\Delta_{k_y}} \\ &= \frac{L_x L_y}{4\pi}\left[\frac{\varepsilon\omega_{max}^2}{c^2} - \left(\frac{\pi}{L_z}\right)^2\right] \end{aligned} \tag{D.6}$$

The number of molecules in the cavity is given by

$$N_{mol} = \rho L_x L_y L_z \tag{D.7}$$

where ρ is the molecule number density. Then the number of molecules per mode is:

$$N = \frac{N_{mol}}{N_{modes}} = \frac{4\pi\rho L_z}{\left[\frac{\varepsilon\omega_{max}^2}{c^2} - \left(\frac{\pi}{L_z}\right)^2\right]}. \tag{D.8}$$

From Ref. [237], we take $\varepsilon = (1.41)^2$, $\omega_{max} = 0.3581 \times 10^{15}$ s^{-1} (which is characteristic for vibrational strong coupling), $L_z = 2$ μm, and $\rho = 8 \times 10^9$ μm^{-3}, resulting in $N \sim 10^{12}$ as reported in the main text.

Bibliography

[1] L. D. Barron, *Molecular Light Scattering and Optical Activity* Cambridge University Press, (2009).

[2] J. Thorne, "Applications of the faraday effect end magnetic circular dichroism in chemistry and physics," in *Optical Polarimetry: Instrumentation and Applications,* vol. 112 International Society for Optics and Photonics, (1977), pp. 120–126.

[3] R. M. Jones, F. E. Inscore, R. Hille, and M. L. Kirk, "Freeze-quench magnetic circular dichroism spectroscopic study of the "very rapid" intermediate in xanthine oxidase," *Inorg. Chem.* **38**, 4963–4970 (1999).

[4] B. J. Stadler and T. Mizumoto, "Integrated magneto-optical materials and isolators: a review," *IEEE Photonics Journal* **6**, 1–15 (2013).

[5] O. Neufeld, D. Ayuso, P. Decleva, M. Y. Ivanov, O. Smirnova, and O. Cohen, "Ultrasensitive chiral spectroscopy by dynamical symmetry breaking in high harmonic generation," *Phys. Rev. X* **9**, 031002 (2019).

[6] D. Ayuso, O. Neufeld, A. F. Ordonez, P. Decleva, G. Lerner, O. Cohen, M. Ivanov, and O. Smirnova, "Synthetic chiral light for efficient control of chiral light–matter interaction," *Nat. Photonics* **13**, 866–871 (2019).

[7] D. Patterson, M. Schnell, and J. M. Doyle, "Enantiomer-specific detection of chiral molecules via microwave spectroscopy," *Nature* **497**, 475–477 (2013).

[8] D. Patterson and J. M. Doyle, "Sensitive chiral analysis via microwave three-wave mixing," *Phys. Rev. Lett.* **111**, 023008 (2013).

[9] Y. Shoji and T. Mizumoto, "Magneto-optical non-reciprocal devices in silicon photonics," *Sci. Technol. Adv. Mat.* **15**, 014602 (2014).

[10] Y. Shoji, K. Miura, and T. Mizumoto, "Optical nonreciprocal devices based on magneto-optical phase shift in silicon photonics," *Journal of Optics* **18**, 013001 (2015).

[11] K. Tolpygo, "Physical properties of a rock salt lattice made up of deformable ions," *Zh. Eksp. Teor. Fiz* **20**, 497 (1950).

[12] K. Huang, "Lattice vibrations and optical waves in ionic crystals," *Nature* **167**, 779–780 (1951).

[13] V. Agranovich, "The influence of reabsorption upon the duration of the fluorescence of molecular crystals," (1957).

[14] J. Hopfield, "Theory of the contribution of excitons to the complex dielectric constant of crystals," *Physical Review* **112**, 1555 (1958).

[15] C. Weisbuch, M. Nishioka, A. Ishikawa, and Y. Arakawa, "Observation of the coupled exciton-photon mode splitting in a semiconductor quantum microcavity," *Physical Review Letters* **69**, 3314 (1992).

[16] A. Canales, D. G. Baranov, T. J. Antosiewicz, and T. Shegai, "Abundance of cavity-free polaritonic states in resonant materials and nanostructures," *The Journal of Chemical Physics* **154** (2021).

[17] D. G. Lidzey, D. Bradley, M. Skolnick, T. Virgili, S. Walker, and D. Whittaker, "Strong exciton–photon coupling in an organic semiconductor microcavity," *Nature* **395**, 53–55 (1998).

[18] A. Shalabney, J. George, J. a. Hutchison, G. Pupillo, C. Genet, and T. W. Ebbesen, "Coherent coupling of molecular resonators with a microcavity mode," *Nature Communications* **6**, 5981 (2015).

[19] J. P. Long and B. Simpkins, "Coherent coupling between a molecular vibration and fabry–perot optical cavity to give hybridized states in the strong coupling limit," *ACS Photonics* **2**, 130–136 (2015).

[20] A. Thomas, J. George, A. Shalabney, M. Dryzhakov, S. J. Varma, J. Moran, T. Chervy, X. Zhong, E. Devaux, C. Genet *et al.*, "Ground-state chemical reactivity under vibrational coupling to the vacuum electromagnetic field," *Angewandte Chemie* **128**, 11634–11638 (2016).

[21] A. Thomas, L. Lethuillier-Karl, K. Nagarajan, R. M. Vergauwe, J. George, T. Chervy, A. Shalabney, E. Devaux, C. Genet, J. Moran *et al.*, "Tilting a ground-state reactivity landscape by vibrational strong coupling," *Science* **363**, 615–619 (2019).

[22] J. A. Campos-Gonzalez-Angulo, R. F. Ribeiro, and J. Yuen-Zhou, "Resonant catalysis of thermally activated chemical reactions with vibrational polaritons," *Nature Communications* **10**, 4685 (2019).

[23] M. Du and J. Yuen-Zhou, "Catalysis by dark states in vibropolaritonic chemistry," *Physical Review Letters* **128**, 096001 (2022).

[24] W. Ahn, J. F. Triana, F. Recabal, F. Herrera, and B. S. Simpkins, "Modification of ground-state chemical reactivity via light–matter coherence in infrared cavities," *Science* **380**, 1165–1168 (2023).

[25] J. A. Hutchison, T. Schwartz, C. Genet, E. Devaux, and T. W. Ebbesen, "Modifying chemical landscapes by coupling to vacuum fields," *Angewandte Chemie International Edition* **51**, 1592–1596 (2012).

[26] F. Herrera and F. C. Spano, "Cavity-controlled chemistry in molecular ensembles," *Physical Review Letters* **116**, 238301 (2016).

[27] J. Galego, F. J. Garcia-Vidal, and J. Feist, "Suppressing photochemical reactions with quantized light fields," *Nature Communications* **7**, 13841 (2016).

[28] J. Galego, F. J. Garcia-Vidal, and J. Feist, "Many-molecule reaction triggered by a single photon in polaritonic chemistry," *Physical Review Letters* **119**, 136001 (2017).

[29] A. Mandal and P. Huo, "Investigating new reactivities enabled by polariton photochemistry," *The journal of physical chemistry letters* **10**, 5519–5529 (2019).

[30] N. M. Hoffmann, L. Lacombe, A. Rubio, and N. T. Maitra, "Effect of many modes on self-polarization and photochemical suppression in cavities," *The Journal of Chemical Physics* **153** (2020).

[31] H. Zeng, J. B. Pérez-Sánchez, C. T. Eckdahl, P. Liu, W. J. Chang, E. A. Weiss, J. A. Kalow, J. Yuen-Zhou, and N. P. Stern, "Control of photoswitching kinetics with strong light–matter coupling in a cavity," *Journal of the American Chemical Society* **145**, 19655–19661 (2023). PMID: 37643086.

[32] A. Dutta, V. Tiainen, L. Duarte, N. Markesevic, D. Morozov, H. A. Qureshi, G. Groenhof, and J. J. Toppari, "Ultra-fast photochemistry in the strong light-matter coupling regime," *ChemRxiv* (2023).

[33] G. G. Rozenman, K. Akulov, A. Golombek, and T. Schwartz, "Long-range transport of organic exciton-polaritons revealed by ultrafast microscopy," *ACS Photonics* **5**, 105–110 (2018).

[34] R. Pandya, A. Ashoka, K. Georgiou, J. Sung, R. Jayaprakash, S. Renken, L. Gai, Z. Shen, A. Rao, and A. J. Musser, "Tuning the coherent propagation of organic exciton-polaritons through dark state delocalization," *Advanced Science* **9**, 2105569 (2022).

[35] G. Engelhardt and J. Cao, "Unusual dynamical properties of disordered polaritons in microcavities," *Physical Review B* **105**, 064205 (2022).

[36] G. Engelhardt and J. Cao, "Polariton localization and dispersion properties of disordered quantum emitters in multimode microcavities," *Physical Review Letters* **130**, 213602 (2023).

[37] D. Xu, A. Mandal, J. M. Baxter, S.-W. Cheng, I. Lee, H. Su, S. Liu, D. R. Reichman, and M. Delor, "Ultrafast imaging of polariton propagation and interactions," *Nature Communications* **14**, 3881 (2023).

[38] I. Sokolovskii, R. H. Tichauer, D. Morozov, J. Feist, and G. Groenhof, "Multi-scale molecular dynamics simulations of enhanced energy transfer in organic molecules under strong coupling," *Nature Communications* **14**, 6613 (2023).

[39] D. M. Coles, N. Somaschi, P. Michetti, C. Clark, P. G. Lagoudakis, P. G. Savvidis, and D. G. Lidzey, "Polariton-mediated energy transfer between organic dyes in a strongly coupled optical microcavity," *Nature Materials* **13**, 712–719 (2014).

[40] X. Zhong, T. Chervy, L. Zhang, A. Thomas, J. George, C. Genet, J. A. Hutchison, and T. W. Ebbesen, "Energy transfer between spatially separated entangled molecules," *Angewandte Chemie* **129**, 9162–9166 (2017).

[41] K. Georgiou, P. Michetti, L. Gai, M. Cavazzini, Z. Shen, and D. G. Lidzey, "Control over energy transfer between fluorescent bodipy dyes in a strongly coupled microcavity," *ACS Photonics* **5**, 258–266 (2018).

[42] M. Du, L. A. Martínez-Martínez, R. F. Ribeiro, Z. Hu, V. M. Menon, and J. Yuen-Zhou, "Theory for polariton-assisted remote energy transfer," *Chemical science* **9**, 6659–6669 (2018).

[43] C. A. DelPo, S.-U.-Z. Khan, K. H. Park, B. Kudisch, B. P. Rand, and G. D. Scholes, "Polariton decay in donor–acceptor cavity systems," *The Journal of Physical Chemistry Letters* **12**, 9774–9782 (2021).

[44] M. Son, Z. T. Armstrong, R. T. Allen, A. Dhavamani, M. S. Arnold, and M. T. Zanni, "Energy cascades in donor-acceptor exciton-polaritons observed by ultrafast two-dimensional white-light spectroscopy," *Nature Communications* **13**, 7305 (2022).

[45] J. Kasprzak, M. Richard, S. Kundermann, A. Baas, P. Jeambrun, J. M. J. Keeling, F. Marchetti, M. Szymańska, R. André, J. Staehli *et al.*, "Bose–einstein condensation of exciton polaritons," *Nature* **443**, 409–414 (2006).

[46] S. Kéna-Cohen and S. Forrest, "Room-temperature polariton lasing in an organic single-crystal microcavity," *Nature Photonics* **4**, 371–375 (2010).

[47] K. Daskalakis, S. Maier, R. Murray, and S. Kéna-Cohen, "Nonlinear interactions in an organic polariton condensate," *Nature materials* **13**, 271–278 (2014).

[48] J. D. Plumhof, T. Stöferle, L. Mai, U. Scherf, and R. F. Mahrt, "Room-temperature bose–einstein condensation of cavity exciton–polaritons in a polymer," *Nature materials* **13**, 247–252 (2014).

[49] S. Pannir-Sivajothi, J. A. Campos-Gonzalez-Angulo, L. A. Martínez-Martínez, S. Sinha, and J. Yuen-Zhou, "Driving chemical reactions with polariton condensates," *Nature communications* **13**, 1645 (2022).

[50] K. Stranius, M. Hertzog, and K. Börjesson, "Selective manipulation of electronically excited states through strong light–matter interactions," *Nature Communications* **9**, 2273 (2018).

[51] L. A. Martínez-Martínez, M. Du, R. F. Ribeiro, S. Kéna-Cohen, and J. Yuen-Zhou, "Polariton-assisted singlet fission in acene aggregates," *The Journal of Physical Chemistry Letters* **9**, 1951–1957 (2018).

[52] S. Takahashi, K. Watanabe, and Y. Matsumoto, "Singlet fission of amorphous rubrene modulated by polariton formation," *The Journal of Chemical Physics* **151** (2019).

[53] A. M. Berghuis, A. Halpin, Q. Le-Van, M. Ramezani, S. Wang, S. Murai, and J. Gómez Rivas, "Enhanced delayed fluorescence in tetracene crystals by strong light-matter coupling," *Advanced Functional Materials* **29**, 1901317 (2019).

[54] D. Polak, R. Jayaprakash, T. P. Lyons, L. Á. Martínez-Martínez, A. Leventis, K. J. Fallon, H. Coulthard, D. G. Bossanyi, K. Georgiou, A. J. Petty *et al.*, "Manipulating molecules with strong coupling: harvesting triplet excitons in organic exciton microcavities," *Chemical science* **11**, 343–354 (2020).

[55] S. Wang, A. Mika, J. A. Hutchison, C. Genet, A. Jouaiti, M. W. Hosseini, and T. W. Ebbesen, "Phase transition of a perovskite strongly coupled to the vacuum field," *Nanoscale* **6**, 7243–7248 (2014).

[56] M. V. Imperatore, J. B. Asbury, and N. C. Giebink, "Reproducibility of cavity-enhanced chemical reaction rates in the vibrational strong coupling regime," *The Journal of Chemical Physics* **154** (2021).

[57] G. D. Wiesehan and W. Xiong, "Negligible rate enhancement from reported cooperative vibrational strong coupling catalysis," *The Journal of Chemical Physics* **155** (2021).

[58] P. A. Thomas, W. J. Tan, V. G. Kravets, A. N. Grigorenko, and W. L. Barnes, "Non-polaritonic effects in cavity-modified photochemistry," *Advanced Materials* **n/a**, 2309393 (2023).

[59] A. P. Fidler, L. Chen, A. M. McKillop, and M. L. Weichman, "Ultrafast dynamics of cn radical reactions with chloroform solvent under vibrational strong coupling," *The Journal of Chemical Physics* **159** (2023).

[60] E. Eizner, L. A. Martínez-Martínez, J. Yuen-Zhou, and S. Kéna-Cohen, "Inverting singlet and triplet excited states using strong light-matter coupling," *Science Advances* **5**, eaax4482 (2019).

[61] G. Jarc, S. Y. Mathengattil, A. Montanaro, F. Giusti, E. M. Rigoni, R. Sergo, F. Fassioli, S. Winnerl, S. Dal Zilio, D. Mihailovic *et al.*, "Cavity-mediated thermal control of metal-to-insulator transition in 1t-tas2," *Nature* **622**, 487–492 (2023).

[62] Z. Brawley, J. E. Yim, S. Pannir-Sivajothi, Y. R. Poh, J. Yuen-Zhou, and M. Sheldon, "Sub-wavelength chemical imaging of a modified reaction due to vibrational strong coupling," *ChemRxiv* (2023).

[63] D. S. Wang and S. F. Yelin, "A roadmap toward the theory of vibrational polariton chemistry," *ACS Photonics* **8**, 2818–2826 (2021).

[64] J. Campos-Gonzalez-Angulo, Y. Poh, M. Du, and J. Yuen-Zhou, "Swinging between shine and shadow: Theoretical advances on thermally activated vibropolaritonic chemistry," *The Journal of Chemical Physics* **158** (2023).

[65] T. Khazanov, S. Gunasekaran, A. George, R. Lomlu, S. Mukherjee, and A. J. Musser, "Embrace the darkness: An experimental perspective on organic exciton–polaritons," *Chemical Physics Reviews* **4** (2023).

[66] K. Schwennicke and J. Yuen-Zhou, "Optical activity from the exciton Aharonov–Bohm effect: A Floquet engineering approach," *The Journal of Physical Chemistry C* **124**, 4206–4214 (2020).

[67] K. Schwennicke and J. Yuen-Zhou, "Enantioselective topological frequency conversion," *The Journal of Physical Chemistry Letters* **13**, 2434–2441 (2022).

[68] K. Schwennicke, N. C. Giebink, and J. Yuen-Zhou, "Extracting accurate light-matter couplings from disordered polaritons," *Nanophotonics* (2024).

[69] K. Schwennicke, A. Koner, J. B. Pérez-Sánchez, and J. Yuen-Zhou, "Classical linear optics effects in molecular polaritonics," *in preparation* (2024).

[70] V. Lucarini, J. J. Saarinen, K.-E. Peiponen, and E. M. Vartiainen, *Kramers-Kronig Relations in Optical Materials Research*, vol. 110 Springer Science & Business Media, (2005).

[71] L. Ying, M. Zhou, X. Luo, J. Liu, and Z. Yu, "Strong magneto-optical response enabled by quantum two-level systems," *Optica* **5**, 1156–1162 (2018).

[72] P. Atkins and M. Miller, "Quantum field theory of optical birefringence phenomena: Iv. the inverse and optical faraday effects," *Mol. Phys.* **15**, 503–514 (1968).

[73] Y. Aharonov and D. Bohm, "Significance of electromagnetic potentials in the quantum theory," *Phys. Rev.* **115**, 485 (1959).

[74] K. v. Klitzing, G. Dorda, and M. Pepper, "New method for high-accuracy determination of the fine-structure constant based on quantized hall resistance," *Phys. Rev. Lett.* **45**, 494 (1980).

[75] T. Ando, Y. Matsumoto, and Y. Uemura, "Theory of hall effect in a two-dimensional electron system," *J. Phys. Soc. Jpn.* **39**, 279–288 (1975).

[76] K. S. Novoselov, Z. Jiang, Y. Zhang, S. Morozov, H. L. Stormer, U. Zeitler, J. Maan, G. Boebinger, P. Kim, and A. K. Geim, "Room-temperature quantum hall effect in graphene,"
Science **315**, 1379–1379 (2007).

[77] L. D. Tzuang, K. Fang, P. Nussenzveig, S. Fan, and M. Lipson, "Non-reciprocal phase shift induced by an effective magnetic flux for light," *Nat. Photonics* **8**, 701 (2014).

[78] M. Hafezi, S. Mittal, J. Fan, A. Migdall, and J. Taylor, "Imaging topological edge states in silicon photonics," *Nat. Photonics* **7**, 1001 (2013).

[79] K. Fang, Z. Yu, and S. Fan, "Realizing effective magnetic field for photons by controlling the phase of dynamic modulation," *Nat. Photonics* **6**, 782 (2012).

[80] H. Sigurdsson, O. Kibis, and I. Shelykh, "Optically induced aharonov-bohm effect in mesoscopic rings," *Phys. Rev. B* **90**, 235413 (2014).

[81] O. V. Kibis, H. Sigurdsson, and I. A. Shelykh, "Aharonov-bohm effect for excitons in a semiconductor quantum ring dressed by circularly polarized light," *Phys. Rev. B* **91**, 235308 (2015).

[82] V. Kozin, I. Iorsh, O. Kibis, and I. Shelykh, "Periodic array of quantum rings strongly coupled to circularly polarized light as a topological insulator," *Phys. Rev. B* **97**, 035416 (2018).

[83] J. H. Shirley, "Solution of the schrödinger equation with a hamiltonian periodic in time," *Phys. Rev.* **138**, B979 (1965).

[84] S.-I. Chu, "Generalized floquet theoretical approaches to intense-field multiphoton and nonlinear optical processes," *Adv. Chem. Phys.* **73**, 739–799 (1989).

[85] D. J. Tannor, *Introduction to Quantum Mechanics: a Time-Dependent Perspective* University Science Books, (2007).

[86] B. Gu and I. Franco, "Optical absorption properties of laser-driven matter," *Phys. Rev. A* **98**, 063412 (2018).

[87] M. Maiuri, M. B. Oviedo, J. C. Dean, M. Bishop, B. Kudisch, Z. S. Toa, B. M. Wong, S. A. McGill, and G. D. Scholes, "High magnetic field detunes vibronic resonances in photosynthetic light harvesting," *J. Phys. Chem. Lett.* **9**, 5548–5554 (2018).

[88] J. Yuen-Zhou, S. K. Saikin, N. Y. Yao, and A. Aspuru-Guzik, "Topologically protected excitons in porphyrin thin films," *Nat. Mater.* **13**, 1026 (2014).

[89] T. Oka and S. Kitamura, "Floquet engineering of quantum materials," *Annu. Rev. Conden. Ma. P.* **10**, 387–408 (2019).

[90] N. Thanh Phuc and A. Ishizaki, "Control of excitation energy transfer in condensed phase molecular ssystems by floquet engineering," *J. Phys. Chem. Lett.* **9**, 1243–1248 (2018).

[91] N. T. Phuc and A. Ishizaki, "Control of quantum dynamics of electron transfer in molecular loop structures: Spontaneous breaking of chiral symmetry under strong decoherence," *Phys. Rev. B* **99**, 064301 (2019).

[92] R. A. Römer and M. E. Raikh, "Aharonov-bohm oscillations in the exciton luminescence from a semiconductor nanoring," *Phys. Status Solidi B* **221**, 535–539 (2000).

[93] H. Hu, J.-L. Zhu, D.-J. Li, and J.-J. Xiong, "Aharonov-bohm effect of excitons in nanorings," *Phys. Rev. B* **63**, 195307 (2001).

[94] A. Govorov, S. Ulloa, K. Karrai, and R. Warburton, "Polarized excitons in nanorings and the optical aharonov-bohm effect," *Phys. Rev. B* **66**, 081309 (2002).

[95] F. Palmero, J. Dorignac, J. Eilbeck, and R. Römer, "Aharonov-bohm effect for an exciton in a finite-width nanoring," *Phys. Rev. B* **72**, 075343 (2005).

[96] I. L. Kuskovsky, W. MacDonald, A. Govorov, L. Mourokh, X. Wei, M. Tamargo, M. Tadic, and F. Peeters, "Optical aharonov-bohm effect in stacked type-ii quantum dots," *Phys. Rev. B* **76**, 035342 (2007).

[97] A. Bree and R. Zwarich, "Absorption spectrum of carbazole in a fluorene matrix," *The Journal of Chemical Physics* **49**, 3355–3358 (1968).

[98] A. R. Auty, A. C. Jones, and D. Phillips, "Time-resolved fluorescence of jet-cooled carbazoles and their weak complexes," *Journal of the Chemical Society, Faraday Transactions 2: Molecular and Chemical Physics* **82**, 1219–1230 (1986).

[99] C.-W. Wang, C. Zhu, and S. H. Lin, "Extremely solvent-enhanced absorbance and fluorescence of carbazole interpreted using a damped franck–condon simulation," *The Journal of Chemical Physics* **152**, 104106 (2020).

[100] I. Yamazaki, S. Akimoto, N. Aratani, and A. Osuka, "Observation of coherent recurrence motion of excitons in anthracene dimers," *Bull. Chem. Soc. Jpn.* **77**, 1959–1971 (2004).

[101] J. D. Biggs and J. A. Cina, "Calculations of nonlinear wave-packet interferometry signals in the pump-probe limit as tests for vibrational control over electronic excitation transfer," *J. Chem. Phys.* **131**, 224302 (2009).

[102] J. D. Biggs and J. A. Cina, "Studies of impulsive vibrational influence on ultrafast electronic excitation transfer," *J. Phys. Chem. A.* **116**, 1683–1693 (2012).

[103] A. Nitzan, *Chemical Dynamics in Condensed Phases: Relaxation, Transfer and Reactions in Condensed Molecular Systems* Oxford university press, (2006).

[104] E. J. Heller, *The Semiclassical Way to Dynamics and Spectroscopy* Princeton University Press, (2018).

[105] M. Maj, C. Ahn, D. Kossowska, K. Park, K. Kwak, H. Han, and M. Cho, "β-isocyanoalanine as an ir probe: comparison of vibrational dynamics between isonitrile and nitrile-derivatized ir probes," *Phys. Chem. Chem. Phys.* **17**, 11770–11778 (2015).

[106] D. R. Hofstadter, "Energy levels and wave functions of bloch electrons in rational and irrational magnetic fields," *Phy. Rev. B.* **14**, 2239 (1976).

[107] L. Baranowski, "Equations of motion of a spin-stabilized projectile for flight stability testing," *J. Theor. App. Mech.* **51**, 235–246 (2013).

[108] S. Mukamel, *Principles of Nonlinear Optical Spectroscopy*, vol. 29 Oxford university press New York, (1995).

[109] K. G. Wilson, "Confinement of quarks," *Phys. Rev. D* **10**, 2445 (1974).

[110] S. Stopkowicz, J. Gauss, K. K. Lange, E. I. Tellgren, and T. Helgaker, "Coupled-cluster theory for atoms and molecules in strong magnetic fields," *J. Chem. Phys.* **143**, 074110 (2015).

[111] Y. Wang, H. Steinberg, P. Jarillo-Herrero, and N. Gedik, "Observation of floquet-bloch states on the surface of a topological insulator," *Science* **342**, 453–457 (2013).

[112] G. D. Scholes, G. R. Fleming, L. X. Chen, A. Aspuru-Guzik, A. Buchleitner, D. F. Coker, G. S. Engel, R. Van Grondelle, A. Ishizaki, D. M. Jonas *et al.*, "Using coherence to enhance function in chemical and biophysical systems," *Nature* **543**, 647 (2017).

[113] L. F. Calderón and L. A. Pachón, "Nonadiabatic sunlight-harvesting," *arXiv preprint arXiv:1909.05029* (2019).

[114] V. Tiwari, W. K. Peters, and D. M. Jonas, "Electronic resonance with anticorrelated pigment vibrations drives photosynthetic energy transfer outside the adiabatic framework," *Proc. Natl. Acad. Sci. U.S.A.* **110**, 1203–1208 (2013).

[115] A. Chenu, N. Christensson, H. F. Kauffmann, and T. Mančal, "Enhancement of vibronic and ground-state vibrational coherences in 2d spectra of photosynthetic complexes," *Sci. Rep.* **3**, 2029 (2013).

[116] A. Noguchi, Y. Shikano, K. Toyoda, and S. Urabe, "Aharonov–bohm effect in the tunnelling of a quantum rotor in a linear paul trap," *Nat. Commun.* **5**, 3868 (2014).

[117] O. Hod, E. Rabani, and R. Baer, "Magnetoresistance of nanoscale molecular devices," *Accounts Chem. Res.* **39**, 109–117 (2006).

[118] K. Schwennicke and J. Yuen-Zhou, "Correction to 'Optical activity from the exciton Aharonov—Bohm effect: A Floquet engineering approach'," *The Journal of Physical Chemistry C* **126**, 15547–15548 (2022).

[119] L. Pasteur, "Sur les relations qui peuvent exister entre la forme crystalline, la composition chimique et le sens de la polarization rotatoire," *Ann. Chim. Phys.* **24**, 442–459 (1848).

[120] M. Quack, J. Stohner, and M. Willeke, "High-resolution spectroscopic studies and theory of parity violation in chiral molecules," *Annu. Rev. Phys. Chem.* **59**, 741–769 (2008).

[121] A. J. Hutt and S. C. Tan, "Drug chirality and its clinical significance," *Drugs* **52**, 1–12 (1996).

[122] B. Kasprzyk-Hordern, "Pharmacologically active compounds in the environment and their chirality," *Chem. Soc. Rev.* **39**, 4466–4503 (2010).

[123] D. G. Blackmond, "The origin of biological homochirality," *Cold Spring Harbor Perspect. Biol.* **2**, a002147 (2010).

[124] Y. Tang and A. E. Cohen, "Optical chirality and its interaction with matter," *Phys. Rev. Lett.* **104**, 163901 (2010).

[125] L. V. Poulikakos, P. Thureja, A. Stollmann, E. De Leo, and D. J. Norris, "Chiral light design and detection inspired by optical antenna theory," *Nano Lett.* **18**, 4633–4640 (2018).

[126] J. García-Guirado, M. Svedendahl, J. Puigdollers, and R. Quidant, "Enantiomer-selective molecular sensing using racemic nanoplasmonic arrays," *Nano Lett.* **18**, 6279–6285 (2018).

[127] A. F. Ordonez and O. Smirnova, "Generalized perspective on chiral measurements without magnetic interactions," *Phys. Rev. A* **98**, 063428 (2018).

[128] B. Ritchie, "Theory of the angular distribution of photoelectrons ejected from optically active molecules and molecular negative ions," *Phys. Rev. A* **13**, 1411 (1976).

[129] N. Böwering, T. Lischke, B. Schmidtke, N. Müller, T. Khalil, and U. Heinzmann, "Asymmetry in photoelectron emission from chiral molecules induced by circularly polarized light," *Phys. Rev. Lett.* **86**, 1187 (2001).

[130] C. Lux, M. Wollenhaupt, T. Bolze, Q. Liang, J. Köhler, C. Sarpe, and T. Baumert, "Circular dichroism in the photoelectron angular distributions of camphor and fenchone from multiphoton ionization with femtosecond laser pulses," *Angew. Chem., Int. Ed.* **51**, 5001–5005 (2012).

[131] P. V. Demekhin, A. N. Artemyev, A. Kastner, and T. Baumert, "Photoelectron circular dichroism with two overlapping laser pulses of carrier frequencies ω and 2 ω linearly polarized in two mutually orthogonal directions," *Phys. Rev. Lett.* **121**, 253201 (2018).

[132] P. Fischer, D. S. Wiersma, R. Righini, B. Champagne, and A. D. Buckingham, "Three-wave mixing in chiral liquids," *Phys. Rev. Lett.* **85**, 4253 (2000).

[133] P. Brumer, E. Frishman, and M. Shapiro, "Principles of electric-dipole-allowed optical control of molecular chirality," *Phys. Rev. A* **65**, 015401 (2001).

[134] S. Beaulieu, A. Comby, D. Descamps, B. Fabre, G. A. Garcia, R. Géneaux, A. G. Harvey, F. Légaré, Z. Mašín, L. Nahon *et al.*, "Photoexcitation circular dichroism in chiral molecules," *Nat. Phys.* **14**, 484–489 (2018).

[135] O. Neufeld, M. Even Tzur, and O. Cohen, "Degree of chirality of electromagnetic fields and maximally chiral light," *Phys. Rev. A* **101**, 053831 (2020).

[136] D. Ayuso, A. F. Ordonez, P. Decleva, M. Ivanov, and O. Smirnova, "Enantio-sensitive unidirectional light bending," *Nat. Commun.* **12**, 1–9 (2021).

[137] V. A. Shubert, D. Schmitz, D. Patterson, J. M. Doyle, and M. Schnell, "Identifying enantiomers in mixtures of chiral molecules with broadband microwave spectroscopy," *Angew. Chem., Int. Ed.* **53**, 1152–1155 (2014).

[138] S. Lobsiger, C. Perez, L. Evangelisti, K. K. Lehmann, and B. H. Pate, "Molecular structure and chirality detection by fourier transform microwave spectroscopy," *J. Phys. Chem. Lett.* **6**, 196–200 (2015).

[139] V. A. Shubert, D. Schmitz, C. Pérez, C. Medcraft, A. Krin, S. R. Domingos, D. Patterson, and M. Schnell, "Chiral analysis using broadband rotational spectroscopy," *J. Phys. Chem. Lett.* **7**, 341–350 (2016).

[140] P. Král and M. Shapiro, "Cyclic population transfer in quantum systems with broken symmetry," *Phy. Rev. Lett.* **87**, 183002 (2001).

[141] P. Král, I. Thanopulos, M. Shapiro, and D. Cohen, "Two-step enantio-selective optical switch," *Phys. Rev. Lett.* **90**, 033001 (2003).

[142] I. Thanopulos, P. Král, and M. Shapiro, "Theory of a two-step enantiomeric purification of racemic mixtures by optical means: The d 2 s 2 molecule," *J. Chem. Phys.* **119**, 5105–5116 (2003).

[143] Y. Li and C. Bruder, "Dynamic method to distinguish between left-and right-handed chiral molecules," *Phys. Rev. A* **77**, 015403 (2008).

[144] N. V. Vitanov and M. Drewsen, "Highly efficient detection and separation of chiral molecules through shortcuts to adiabaticity," *Phys. Rev. Lett.* **122**, 173202 (2019).

[145] Y.-H. Kang, Z.-C. Shi, J. Song, and Y. Xia, "Effective discrimination of chiral molecules in a cavity," *Opt. Lett.* **45**, 4952–4955 (2020).

[146] J.-L. Wu, Y. Wang, J.-X. Han, C. Wang, S.-L. Su, Y. Xia, Y. Jiang, and J. Song, "Two-path interference for enantiomer-selective state transfer of chiral molecules," *Phys. Rev. Appl.* **13**, 044021 (2020).

[147] I. Tutunnikov, L. Xu, R. W. Field, K. A. Nelson, Y. Prior, and I. S. Averbukh, "Enantioselective orientation of chiral molecules induced by terahertz pulses with twisted polarization," *Phys. Rev. Res.* **3**, 013249 (2021).

[148] W. Gerlach and O. Stern, "Der experimentelle nachweis der richtungsquantelung im magnetfeld," *Z. Phys.* **9**, 349–352 (1922).

[149] J. E. Hirsch, "Spin hall effect," *Phys. Rev. Lett.* **83**, 1834 (1999).

[150] Y. Li, C. Bruder, and C. P. Sun, "Generalized stern-gerlach effect for chiral molecules," *Phys. Rev. Lett.* **99**, 130403 (2007).

[151] X. Li and M. Shapiro, "Theory of the optical spatial separation of racemic mixtures of chiral molecules," *J. Chem. Phys.* **132**, 194315 (2010).

[152] Y.-Y. Chen, C. Ye, Q. Zhang, and Y. Li, "Enantio-discrimination via light deflection effect," *J. Chem. Phys.* **152**, 204305 (2020).

[153] C. L. Kane and E. J. Mele, "Quantum spin hall effect in graphene," *Phys. Rev. Lett.* **95**, 226801 (2005).

[154] D. J. Thouless, M. Kohmoto, M. P. Nightingale, and M. den Nijs, "Quantized hall conductance in a two-dimensional periodic potential," *Phy. Rev. Lett.* **49**, 405 (1982).

[155] M. Z. Hasan and C. L. Kane, "Colloquium: topological insulators," *Rev. Mod. Phys.* **82**, 3045 (2010).

[156] M. H. Kolodrubetz, F. Nathan, S. Gazit, T. Morimoto, and J. E. Moore, "Topological floquet-thouless energy pump," *Phys. Rev. Lett.* **120**, 150601 (2018).

[157] I. Mondragon-Shem, I. Martin, A. Alexandradinata, and M. Cheng, "Quantized frequency-domain polarization of driven phases of matter," *arXiv preprint arXiv:1811.10632* (2018).

[158] F. Nathan, I. Martin, and G. Refael, "Topological frequency conversion in a driven dissipative quantum cavity," *Phys. Rev. B* **99**, 094311 (2019).

[159] P. Leboeuf, J. Kurchan, M. Feingold, and D. P. Arovas, "Phase-space localization: topological aspects of quantum chaos," *Phys. Rev. Lett.* **65**, 3076 (1990).

[160] P. Leboeuf, J. Kurchan, M. Feingold, and D. P. Arovas, "Topological aspects of quantum chaos," *Chaos* **2**, 125–130 (1992).

[161] I. Martin, G. Refael, and B. Halperin, "Topological frequency conversion in strongly driven quantum systems," *Phys. Rev. X* **7**, 041008 (2017).

[162] A. F. Ordonez and O. Smirnova, "Propensity rules in photoelectron circular dichroism in chiral molecules. ii. general picture," *Phys. Rev. A* **99**, 043417 (2019).

[163] K. K. Lehmann, "Influence of spatial degeneracy on rotational spectroscopy: Three-wave mixing and enantiomeric state separation of chiral molecules," *J. Chem. Phys.* **149**, 094201 (2018).

[164] M. Leibscher, T. F. Giesen, and C. P. Koch, "Principles of enantio-selective excitation in three-wave mixing spectroscopy of chiral molecules," *J. Chem. Phys.* **151**, 014302 (2019).

[165] J. Simons, *An introduction to theoretical chemistry* Cambridge University Press, Cambridge, (2003).

[166] E. Boyers, P. J. D. Crowley, A. Chandran, and A. O. Sushkov, "Exploring 2d synthetic quantum hall physics with a quasiperiodically driven qubit," *Phys. Rev. Lett.* **125**, 160505 (2020).

[167] A. M. Samoilenko, *Elements of the mathematical theory of multi-frequency oscillations*, vol. 71 Springer Science & Business Media, Berlin, (2012).

[168] B. A. Bernevig and S.-C. Zhang, "Quantum spin hall effect," *Phys. Rev. Lett.* **96**, 106802 (2006).

[169] J. A. Schellman, "Circular dichroism and optical rotation," *Chem. Rev.* **75**, 323–331 (1975).

[170] G. B. Park and R. W. Field, "Perspective: The first ten years of broadband chirped pulse fourier transform microwave spectroscopy," *J. Chem. Phys.* **144**, 200901 (2016).

[171] M. Belkin, T. Kulakov, K.-H. Ernst, L. Yan, and Y. Shen, "Sum-frequency vibrational spectroscopy on chiral liquids: a novel technique to probe molecular chirality," *Phys. Rev. Lett.* **85**, 4474 (2000).

[172] P. Fischer, A. Buckingham, K. Beckwitt, D. Wiersma, and F. Wise, "New electro-optic effect: sum-frequency generation from optically active liquids in the presence of a dc electric field," *Phys. Rev. Lett.* **91**, 173901 (2003).

[173] F. Faure and B. Zhilinskii, "Topological chern indices in molecular spectra," *Phys. Rev. Lett.* **85**, 960 (2000).

[174] A. F. Ordonez, D. Ayuso, P. Decleva, and O. Smirnova, "Geometric magnetism and new enantio-sensitive observables in photoionization of chiral molecules," *arXiv preprint arXiv:2106.14264* (2021).

[175] A. Frisk Kockum, A. Miranowicz, S. De Liberato, S. Savasta, and F. Nori, "Ultrastrong coupling between light and matter," *Nature Reviews Physics* **1**, 19–40 (2019).

[176] M. Balasubrahmaniyam, A. Simkhovich, A. Golombek, G. Sandik, G. Ankonina, and T. Schwartz, "From enhanced diffusion to ultrafast ballistic motion of hybrid light–matter excitations," *Nature Materials* **22**, 338–344 (2023).

[177] T. Schwartz, J. A. Hutchison, C. Genet, and T. W. Ebbesen, "Reversible switching of ultrastrong light-molecule coupling," *Physical review letters* **106**, 196405 (2011).

[178] M. Mazzeo, A. Genco, S. Gambino, D. Ballarini, F. Mangione, O. Di Stefano, S. Patanè, S. Savasta, D. Sanvitto, and G. Gigli, "Ultrastrong light-matter coupling in electrically doped microcavity organic light emitting diodes," *Applied Physics Letters* **104** (2014).

[179] J. George, T. Chervy, A. Shalabney, E. Devaux, H. Hiura, C. Genet, and T. W. Ebbesen, "Multiple rabi splittings under ultrastrong vibrational coupling," *Physical review letters* **117**, 153601 (2016).

[180] E. Eizner, J. Brodeur, F. Barachati, A. Sridharan, and S. Kéna-Cohen, "Organic photodiodes with an extended responsivity using ultrastrong light–matter coupling," *ACS Photonics* **5**, 2921–2927 (2018).

[181] M. Tavis and F. W. Cummings, "Exact solution for an n-molecule—radiation-field hamiltonian," *Physical Review* **170**, 379 (1968).

[182] R. F. Ribeiro, L. A. Martínez-Martínez, M. Du, J. Campos-Gonzalez-Angulo, and J. Yuen-Zhou, "Polariton chemistry: controlling molecular dynamics with optical cavities," *Chemical science* **9**, 6325–6339 (2018).

[183] J. Feist and F. J. Garcia-Vidal, "Extraordinary exciton conductance induced by strong coupling," *Physical review letters* **114**, 196402 (2015).

[184] J. Schachenmayer, C. Genes, E. Tignone, and G. Pupillo, "Cavity-enhanced transport of excitons," *Physical review letters* **114**, 196403 (2015).

[185] T. Botzung, D. Hagenmüller, S. Schütz, J. Dubail, G. Pupillo, and J. Schachenmayer, "Dark state semilocalization of quantum emitters in a cavity," *Physical Review B* **102**, 144202 (2020).

[186] T. F. Allard and G. Weick, "Disorder-enhanced transport in a chain of lossy dipoles strongly coupled to cavity photons," *Physical Review B* **106**, 245424 (2022).

[187] E. Suyabatmaz and R. F. Ribeiro, "Vibrational polariton transport in disordered media," *The Journal of Chemical Physics* **159** (2023).

[188] N. Krainova, A. J. Grede, D. Tsokkou, N. Banerji, and N. C. Giebink, "Polaron photoconductivity in the weak and strong light-matter coupling regime," *Physical review letters* **124**, 177401 (2020).

[189] J. B. Pérez-Sánchez, F. Mellini, N. C. Giebink, and J. Yuen-Zhou, "Frequency-dependent photoreactivity in disordered molecular polaritons," *arXiv preprint arXiv:2308.03954* (2023).

[190] I. Diniz, S. Portolan, R. Ferreira, J. Gérard, P. Bertet, and A. Auffeves, "Strongly coupling a cavity to inhomogeneous ensembles of emitters: Potential for long-lived solid-state quantum memories," *Physical Review A* **84**, 063810 (2011).

[191] Z. Kurucz, J. Wesenberg, and K. Mølmer, "Spectroscopic properties of inhomogeneously broadened spin ensembles in a cavity," *Physical Review A* **83**, 053852 (2011).

[192] S. Pau, G. Björk, J. Jacobson, H. Cao, and Y. Yamamoto, "Microcavity exciton-polariton splitting in the linear regime," *Physical Review B* **51**, 14437 (1995).

[193] V. Savona, L. Andreani, P. Schwendimann, and A. Quattropani, "Quantum well excitons in semiconductor microcavities: Unified treatment of weak and strong coupling regimes," *Solid State Communications* **93**, 733–739 (1995).

[194] R. Houdré, R. Stanley, and M. Ilegems, "Vacuum-field rabi splitting in the presence of inhomogeneous broadening: Resolution of a homogeneous linewidth in an inhomogeneously broadened system," *Physical Review A* **53**, 2711 (1996).

[195] S. Pau, G. Björk, H. Cao, E. Hanamura, and Y. Yamamoto, "Theory of inhomogeneous microcavity polariton splitting," *Solid state communications* **98**, 781–784 (1996).

[196] C. Sommer, M. Reitz, F. Mineo, and C. Genes, "Molecular polaritonics in dense mesoscopic disordered ensembles," *Physical Review Research* **3**, 033141 (2021).

[197] T. Gera and K. L. Sebastian, "Effects of disorder on polaritonic and dark states in a cavity using the disordered tavis–cummings model," *The Journal of Chemical Physics* **156** (2022).

[198] T. Gera and K. L. Sebastian, "Exact results for the tavis cummings and hückel hamiltonians with diagonal disorder," *The Journal of Physical Chemistry A* **126**, 5449–5457 (2022).

[199] B. Cohn, S. Sufrin, A. Basu, and L. Chuntonov, "Vibrational polaritons in disordered molecular ensembles," *The Journal of Physical Chemistry Letters* **13**, 8369–8375 (2022).

[200] Z. Zhou, H.-T. Chen, J. E. Subotnik, and A. Nitzan, "Interplay between disorder, local relaxation, and collective behavior for an ensemble of emitters outside versus inside a cavity," *Physical Review A* **108**, 023708 (2023).

[201] C. Climent, J. E. Subotnik, and A. Nitzan, "Kubo-anderson theory of polariton lineshape," *arXiv preprint arXiv:2310.13860* (2023).

[202] V. G. Kravets, A. V. Kabashin, W. L. Barnes, and A. N. Grigorenko, "Plasmonic surface lattice resonances: a review of properties and applications," *Chemical reviews* **118**, 5912–5951 (2018).

[203] R. W. Wood, "On a remarkable case of uneven distribution of light in a diffraction grating spectrum," *The London, Edinburgh, and Dublin Philosophical Magazine and Journal of Science* **4**, 396–402 (1902).

[204] J. M. McMahon, J. Henzie, T. W. Odom, G. C. Schatz, and S. K. Gray, "Tailoring the sensing capabilities of nanohole arrays in gold films with rayleigh anomaly-surface plasmon polaritons," *Optics express* **15**, 18119–18129 (2007).

[205] F. G. De Abajo, "Colloquium: Light scattering by particle and hole arrays," *Reviews of Modern Physics* **79**, 1267 (2007).

[206] A. A. Darweesh, S. J. Bauman, D. T. Debu, and J. B. Herzog, "The role of rayleigh-wood anomalies and surface plasmons in optical enhancement for nano-gratings," *Nanomaterials* **8**, 809 (2018).

[207] E. Galiffi, Y.-T. Wang, Z. Lim, J. B. Pendry, A. Alù, and P. A. Huidobro, "Wood anomalies and surface-wave excitation with a time grating," *Physical Review Letters* **125**, 127403 (2020).

[208] J. A. Ćwik, P. Kirton, S. De Liberato, and J. Keeling, "Excitonic spectral features in strongly coupled organic polaritons," *Physical Review A* **93**, 033840 (2016).

[209] J. Yuen-Zhou and A. Koner, "Linear response of molecular polaritons," *arXiv preprint arXiv:2310.15424* (2023).

[210] A. Chenu and J. Cao, "Construction of multichromophoric spectra from monomer data: applications to resonant energy transfer," *Physical review letters* **118**, 013001 (2017).

[211] D. G. Hummer, "Expansion of dawson's function in a series of chebyshev polynomials," *Mathematics of Computation* **18**, 317–319 (1964).

[212] D. De Bernardis, M. Jeannin, J.-M. Manceau, R. Colombelli, A. Tredicucci, and I. Carusotto, "Magnetic-field-induced cavity protection for intersubband polaritons," *Physical Review B* **106**, 224206 (2022).

[213] A. Moroz, "A hidden analytic structure of the rabi model," *Annals of Physics* **340**, 252–266 (2014).

[214] L. A. Martínez-Martínez, R. F. Ribeiro, J. Campos-González-Angulo, and J. Yuen-Zhou, "Can ultrastrong coupling change ground-state chemical reactions?" *ACS Photonics* **5**, 167–176 (2018).

[215] P. W. Atkins and R. S. Friedman, *Molecular quantum mechanics* Oxford university press, (2011).

[216] I. Lee, S. R. Melton, D. Xu, and M. Delor, "Controlling molecular photoisomerization in photonic cavities through polariton funneling," *Journal of the American Chemical Society* (2024).

[217] X. Zhong, T. Chervy, S. Wang, J. George, A. Thomas, J. A. Hutchison, E. Devaux, C. Genet, and T. W. Ebbesen, "Non-radiative energy transfer mediated by hybrid light-matter states," *Angewandte Chemie International Edition* **55**, 6202–6206 (2016).

[218] R. T. Grant, P. Michetti, A. J. Musser, P. Gregoire, T. Virgili, E. Vella, M. Cavazzini, K. Georgiou, F. Galeotti, C. Clark *et al.*, "Efficient radiative pumping of polaritons in a strongly coupled microcavity by a fluorescent molecular dye," *Advanced Optical Materials* **4**, 1615–1623 (2016).

[219] D. Dovzhenko, M. Lednev, K. Mochalov, I. Vaskan, Y. Rakovich, A. Karaulov, and I. Nabiev, "Polariton-assisted manipulation of energy relaxation pathways: donor–acceptor role reversal in a tuneable microcavity," *Chem. Sci.* **12**, 12794–12805 (2021).

[220] B. Liu, V. M. Menon, and M. Y. Sfeir, "The role of long-lived excitons in the dynamics of strongly coupled molecular polaritons," *ACS Photonics* **7**, 2292–2301 (2020).

[221] Y. Zhu, D. J. Gauthier, S. Morin, Q. Wu, H. Carmichael, and T. Mossberg, "Vacuum rabi splitting as a feature of linear-dispersion theory: Analysis and experimental observations," *Physical Review Letters* **64**, 2499 (1990).

[222] M. Schubert, "Polarization-dependent optical parameters of arbitrarily anisotropic homogeneous layered systems," *Physical Review B* **53**, 4265 (1996).

[223] A. Yariv and P. Yeh, *Photonics: optical electronics in modern communications* Oxford University Press, (2007).

[224] N. Német, D. White, S. Kato, S. Parkins, and T. Aoki, "Transfer-matrix approach to determining the linear response of all-fiber networks of cavity-qed systems," *Physical Review Applied* **13**, 064010 (2020).

[225] F. Herrera and J. Owrutsky, "Molecular polaritons for controlling chemistry with quantum optics," *The Journal of Chemical Physics* **152** (2020).

[226] B. S. Simpkins, A. D. Dunkelberger, and I. Vurgaftman, "Control, modulation, and analytical descriptions of vibrational strong coupling," *Chemical Reviews* **123**, 5020–5048 (2023).

[227] A. D. Wright, J. C. Nelson, and M. L. Weichman, "Rovibrational polaritons in gas-phase methane," *Journal of the American Chemical Society* **145**, 5982–5987 (2023).

[228] A. Dunkelberger, B. Spann, K. Fears, B. Simpkins, and J. Owrutsky, "Modified relaxation dynamics and coherent energy exchange in coupled vibration-cavity polaritons," *Nature Communications* **7**, 13504 (2016).

[229] B. Xiang, R. F. Ribeiro, A. D. Dunkelberger, J. Wang, Y. Li, B. S. Simpkins, J. C. Owrutsky, J. Yuen-Zhou, and W. Xiong, "Two-dimensional infrared spectroscopy of vibrational polaritons," *Proceedings of the National Academy of Sciences* **115**, 4845–4850 (2018).

[230] S. Renken, R. Pandya, K. Georgiou, R. Jayaprakash, L. Gai, Z. Shen, D. G. Lidzey, A. Rao, and A. J. Musser, "Untargeted effects in organic exciton–polariton transient spectroscopy: A cautionary tale," *The Journal of Chemical Physics* **155** (2021).

[231] C.-Y. Cheng, N. Krainova, A. N. Brigeman, A. Khanna, S. Shedge, C. Isborn, J. Yuen-Zhou, and N. C. Giebink, "Molecular polariton electroabsorption," *Nature Communications* **13**, 7937 (2022).

[232] O. Hirschmann, H. H. Bhakta, and W. Xiong, "The role of ir inactive mode in w (co) 6 polariton relaxation process," *Nanophotonics* (2023).

[233] M. A. Zeb, P. G. Kirton, and J. Keeling, "Exact states and spectra of vibrationally dressed polaritons," *ACS Photonics* **5**, 249–257 (2018).

[234] J. B. Pérez-Sánchez, A. Koner, N. P. Stern, and J. Yuen-Zhou, "Simulating molecular polaritons in the collective regime using few-molecule models," *Proceedings of the National Academy of Sciences* **120**, e2219223120 (2023).

[235] J. Feist, J. Galego, and F. J. Garcia-Vidal, "Polaritonic chemistry with organic molecules," *ACS Photonics* **5**, 205–216 (2018).

[236] K. S. Daskalakis, S. A. Maier, and S. Kéna-Cohen, "Polariton condensation in organic semiconductors," *Quantum Plasmonics* pp. 151–163 (2017).

[237] J. del Pino, J. Feist, and F. J. Garcia-Vidal, "Quantum theory of collective strong coupling of molecular vibrations with a microcavity mode," *New Journal of Physics* **17**, 053040 (2015).

[238] N. Makri, "The linear response approximation and its lowest order corrections: An influence functional approach," *The Journal of Physical Chemistry B* **103**, 2823–2829 (1999).

[239] U. Fano and J. H. Macek, "Impact excitation and polarization of the emitted light," *Rev. Mod. Phys.* **45**, 553–573 (1973).

[240] S. Mukamel, *Principles of nonlinear optical spectroscopy* Oxford University Press, (1995).

[241] S. Gunasekaran, R. F. Pinard, and A. J. Musser, "Continuum model of strong light-matter coupling for molecular polaritons," *arXiv preprint arXiv:2308.08744* (2023).

[242] M. Reitz, C. Sommer, and C. Genes, "Langevin approach to quantum optics with molecules," *Physical Review Letters* **122**, 203602 (2019).

[243] H. Li, A. Piryatinski, J. Jerke, A. R. S. Kandada, C. Silva, and E. R. Bittner, "Probing dynamical symmetry breaking using quantum-entangled photons," *Quantum Science and Technology* **3**, 015003 (2017).

[244] R. F. Ribeiro, A. D. Dunkelberger, B. Xiang, W. Xiong, B. S. Simpkins, J. C. Owrutsky, and J. Yuen-Zhou, "Theory for nonlinear spectroscopy of vibrational polaritons," *The Journal of Physcial Chemistry Letters* **9**, 3766–3771 (2018).

[245] K. S. Kansanen, J. J. Toppari, and T. T. Heikkilä, "Polariton response in the presence of brownian dissipation from molecular vibrations," *The Journal of Chemical Physics* **154** (2021).

[246] T. Leppälä, A. G. Abdelmagid, H. A. Qureshi, K. S. Daskalakis, and K. Luoma, "Linear optical properties of organic microcavity polaritons with non-markovian quantum state diffusion," (2023).

[247] G. Groenhof, C. Climent, J. Feist, D. Morozov, and J. J. Toppari, "Tracking polariton relaxation with multiscale molecular dynamics simulations," *The Journal of Physical Chemistry Letters* **10**, 5476–5483 (2019).

[248] B. Cui and A. Nizan, "Collective response in light–matter interactions: The interplay between strong coupling and local dynamics," *The Journal of Chemical Physics* **157**, 114108 (2022).

[249] P. Fowler-Wright, B. W. Lovett, and J. Keeling, "Efficient many-body non-markovian dynamics of organic polaritons," *Phys. Rev. Lett.* **129**, 173001 (2022).

[250] F. C. Spano and H. Yamagata, "Vibronic coupling in j-aggregates and beyond: a direct means of determining the exciton coherence length from the photoluminescence spectrum," *The Journal of Physical Chemistry B* **115**, 5133–5143 (2011).

[251] P. Brumer and M. Shapiro, "One photon mode selective control of reactions by rapid or shaped laser pulses: An emperor without clothes?" *Chemical Physics* **139**, 221–228 (1989).

[252] G. Groenhof and J. J. Toppari, "Coherent light harvesting through strong coupling to confined light," *The Journal of Physical Chemistry Letters* **9**, 4848–4851 (2018).

[253] N. F. Scherer, R. J. Carlson, A. Matro, M. Du, A. J. Ruggiero, V. Romero-Rochin, J. A. Cina, G. R. Fleming, and S. A. Rice, "Fluorescence-detected wave packet interferometry: Time resolved molecular spectroscopy with sequences of femtosecond phase-locked pulses," *The Journal of Chemical Physics* **95**, 1487–1511 (1991).

[254] P. Brumer and M. Shapiro, "Control of unimolecular reactions using coherent light," *Chemical Physics Letters* **126**, 541–546 (1986).

[255] D. J. Tannor, R. Kosloff, and S. A. Rice, "Coherent pulse sequence induced control of selectivity of reactions: Exact quantum mechanical calculations," *The Journal of Chemical Physics* **85**, 5805–5820 (1986).

[256] M. Litinskaya, P. Reineker, and V. M. Agranovich, "Fast polariton relaxation in strongly coupled organic microcavities," *Journal of Luminescence* **110**, 364–372 (2004).

[257] P. Michetti and G. C. La Rocca, "Simulation of j-aggregate microcavity photoluminescence," *Physical Review B* **77**, 195301 (2008).

[258] P. Michetti and G. C. La Rocca, "Exciton-phonon scattering and photoexcitation dynamics in j-aggregate microcavities," *Physical Review B* **79**, 035325 (2009).

[259] J. Chovan, I. Perakis, S. Ceccarelli, and D. Lidzey, "Controlling the interactions between polaritons and molecular vibrations in strongly coupled organic semiconductor microcavities," *Physical Review B* **78**, 045320 (2008).

[260] D. M. Coles, P. Michetti, C. Clark, W. C. Tsoi, A. M. Adawi, J.-S. Kim, and D. G. Lidzey, "Vibrationally assisted polariton-relaxation processes in strongly coupled organic-semiconductor microcavities," *Advanced Functional Materials* **21**, 3691–3696 (2011).

[261] N. Somaschi, L. Mouchliadis, D. Coles, I. Perakis, D. Lidzey, P. Lagoudakis, and P. Savvidis, "Ultrafast polariton population build-up mediated by molecular phonons in organic microcavities," *Applied Physics Letters* **99** (2011).

[262] L. A. Martínez-Martínez, E. Eizner, S. Kéna-Cohen, and J. Yuen-Zhou, "Triplet harvesting in the polaritonic regime: A variational polaron approach," *The Journal of Chemical Physics* **151** (2019).

[263] B. Xiang, R. F. Ribeiro, M. Du, L. Chen, Z. Yang, J. Wang, J. Yuen-Zhou, and W. Xiong, "Intermolecular vibrational energy transfer enabled by microcavity strong light–matter coupling," *Science* **368**, 665–667 (2020).

[264] G. Zengin, M. Wersäll, S. Nilsson, T. J. Antosiewicz, M. Käll, and T. Shegai, "Realizing strong light-matter interactions between single-nanoparticle plasmons and molecular excitons at ambient conditions," *Physical Review Letters* **114**, 157401 (2015).

[265] R. Chikkaraddy, B. De Nijs, F. Benz, S. J. Barrow, O. A. Scherman, E. Rosta, A. Demetriadou, P. Fox, O. Hess, and J. J. Baumberg, "Single-molecule strong coupling at room temperature in plasmonic nanocavities," *Nature* **535**, 127–130 (2016).

[266] F. Benz, M. K. Schmidt, A. Dreismann, R. Chikkaraddy, Y. Zhang, A. Demetriadou, C. Carnegie, H. Ohadi, B. De Nijs, R. Esteban *et al.*, "Single-molecule optomechanics in "picocavities"," *Science* **354**, 726–729 (2016).

[267] K. Santhosh, O. Bitton, L. Chuntonov, and G. Haran, "Vacuum rabi splitting in a plasmonic cavity at the single quantum emitter limit," *Nature Communications* **7**, 11823 (2016).

[268] A. Pscherer, M. Meierhofer, D. Wang, H. Kelkar, D. Martín-Cano, T. Utikal, S. Götzinger, and V. Sandoghdar, "Single-molecule vacuum rabi splitting: Four-wave mixing and optical switching at the single-photon level," *Phys. Rev. Lett.* **127**, 133603 (2021).

[269] A. Koner, M. Du, S. Pannir-Sivajothi, R. H. Goldsmith, and J. Yuen-Zhou, "A path towards single molecule vibrational strong coupling in a fabry–pérot microcavity," *Chemical Science* **14**, 7753–7761 (2023).

[270] L. Mazza, S. Kéna-Cohen, P. Michetti, and G. C. La Rocca, "Microscopic theory of polariton lasing via vibronically assisted scattering," *Phys. Rev. B* **88**, 075321 (2013).

[271] T. Andrijauskas, E. Anisimovas, M. Račiūnas, A. Mekys, V. Kudriašov, I. B. Spielman, and G. Juzeliūnas, "Three-level haldane-like model on a dice optical lattice," *Phys. Rev. A* **92**, 033617 (2015).

[272] N. Goldman, E. Anisimovas, F. Gerbier, P. Öhberg, I. B. Spielman, and G. Juzeliūnas, "Measuring topology in a laser-coupled honeycomb lattice: from chern insulators to topological semi-metals," *New J. Phys.* **15**, 013025 (2013).